NASA CONTRACTOR REPORT

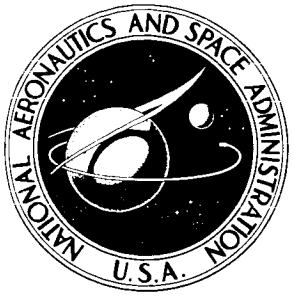

NASA CR-2031

NASA CR-2031

A SYMMETRICAL LASER DOPPLER VELOCITY METER AND ITS APPLICATION TO TURBULENCE CHARACTERIZATION

by M. K. Mazumder

Prepared by
UNIVERSITY OF ARKANSAS
GRADUATE INSTITUTE OF TECHNOLOGY
Little Rock, Ark. 72203
for Ames Research Center

NATIONAL AERONAUTICS AND SPACE ADMINISTRATION • WASHINGTON, D. C. • MAY 1972

1. Report No. NASA CR-2031	2. Government Accession No.	3. Recipient's Catalog No.
4. Title and Subtitle A Symmetrical Laser Doppler Velocity Meter and Its Application To Turbulence Characterization		5. Report Date May 1972 6. Performing Organization Code
7. Author(s) M. K. Mazumder		8. Performing Organization Report No.
9. Performing Organization Name and Address University of Arkansas Graduate Institute of Technology Little Rock, Arkansas		10. Work Unit No. 11. Contract or Grant No. NGL 04-001-007
12. Sponsoring Agency Name and Address National Aeronautics & Space Administration Washington, D.C.		13. Type of Report and Period Covered NASA Contractor Report 14. Sponsoring Agency Code
15. Supplementary Notes		

16. Abstract A symmetrical method of optical heterodyning of the Doppler shifted scattered laser radiation has been developed for velocity measurements with a minimal instrumental spectral broadening and a high signal-to-noise ratio. The method employs two laser beams incident on the moving scatterer and does not use any reference beam for heterodyning. The Doppler signal frequency is independent of the scattering angle and the signal possesses no receiving aperture broadening. Optical alignment is simple. Typical values of the instrumental spectral broadening were approximately 0.8 percent of the center frequency of the Doppler signal, and the signal-to-noise ratio was approximately 25 dB, obtained from an air flow system using submicron dioctylphthalate scattering aerosol. Experimental and theoretical studies were made on the characteristics of the Doppler signal and the effect of system parameters in turbulent flow measurement. The optimization process involved in the beam optics and in the use of a spatial filter is described. For localized flow measurement in any direction of the three-dimensional orthogonal coordinates, the system, using uncorrected optical components, had a sensing volume which can be described by a sensitive length of 600 microns and a diameter of 100 microns. The directional ambiguity in velocity measurement was removed by employing the same heterodyning technique where the two coherent incident beams used were of slightly different frequencies. This frequency shift was accomplished by using a rotating diffraction grating. With this adjustable frequency bias, the Doppler signal from the moving scatterer was no longer an "even" mathematical function of the velocity.

The method was applied to the investigation of the decay of grid-generated turbulence in a wind tunnel. Air at room temperature containing dioctyl-phthalate aerosol was used as the fluid medium. Aerosol dynamics and scattering properties were studied and it was found that aerosol in the size range 0.5 to 1 micron diameter will follow the turbulent eddies. The scattering intensity at a distance of 50 cm from the sensing volume will be approximately 1×10^{-7} W/particle at 30° scattering angle for an incident laser power of 30 mW and wavelength 6328 A. A simple frequency-to-voltage conversion device has been developed using a phase locked loop integrated circuit. The present work on the characterization of turbulence was limited to turbulence of low Reynolds number. Statistical parameters, that are most often used to describe the structure of turbulence, such as mean velocity correlations, energy spectrum, energy decay at the final decay period, etc., were measured using both analog and digital methods. A close agreement was observed between the theoretical expectations and the experimental results.

17. Key Words (Suggested by Author(s))	18. Distribution Statement		
Lasers, Doppler Effect, Velocity	UNCLASSIFIED-UNLIMITED		
19. Security Classif. (of this report) UNCLASSIFIED	20. Security Classif. (of this page) UNCLASSIFIED	21. No. of Pages 193	22. Price* 3.00

*For sale by the National Technical Information Service, Springfield, Virginia 22151

TABLE OF CONTENTS

LIST OF FIGURES

LIST OF TABLES

ACKNOWLEDGEMENTS

The study described in this report was supported by Research Grant NGL 04-001-007 from the National Aeronautics and Space Administration, Ames Research Center, Moffett Field, California.

The Co-Principal Investigator and primary author of the work described herein is:

M. K. Mazumder

The personnel of the Department of Electronics and Instrumentation of the University of Arkansas Graduate Institute of Technology who assisted in this study are:

Dr. J. G. Dodd, Consultant, University of Tennessee

Mr. P. C. McLeod, Assistant Professor

Mr. R. W. Raible, Associate Professor

Dr. T. A. Raju, Associate Professor

Dr. R. A. Sims, Assistant Professor

Mr. D. L. Wankum, Graduate Research Assistant

ABSTRACT

A symmetrical method of optical heterodyning of the Doppler shifted scattered laser radiation has been developed for velocity measurements with a minimal instrumental spectral broadening and a high signal-to-noise ratio. The method employs two laser beams incident on the moving scatterer and does not use any reference beam for heterodyning. The Doppler signal frequency is independent of the scattering angle and the signal possesses no receiving aperture broadening. Optical alignment is simple. Typical values of the instrumental spectral broadening were approximately 0.8 percent of the center frequency of the Doppler signal, and the signal-to-noise ratio was approximately 25 dB, obtained from an air flow system using submicron dioctylphthalate scattering aerosol. Experimental and theoretical studies were made on the characteristics of the Doppler signal and the effect of system parameters in turbulent flow measurement. The optimization process involved in the beam optics and in the use of a spatial filter is described. For localized flow measurement in any direction of the three-dimensional orthogonal coordinates, the system, using uncorrected optical components, had a sensing volume which can be described by a sensitive length of 600 microns and a diameter of 100 microns. The directional ambiguity in velocity measurement was removed by employing the same heterodyning technique where the two coherent incident beams used were of slightly different frequencies. This frequency shift was accomplished by using a rotating diffraction grating. With this adjustable frequency

bias, the Doppler signal from the moving scatterer was no longer an "even" mathematical function of the velocity.

The method was applied to the investigation of the decay of grid-generated turbulence in a wind tunnel. Air at room temperature containing dioctyl-phthalate aerosol was used as the fluid medium. Aerosol dynamics and scattering properties were studied and it was found that aerosol in the size range 0.5 to 1 micron diameter will follow the turbulent eddies. The scattering intensity at a distance of 50 cm from the sensing volume will be approximately 1×10^{-7} W/particle at 30° scattering angle for an incident laser power of 30 mW and wavelength 6328 A. A simple frequency-to-voltage conversion device has been developed using a phase locked loop integrated circuit. The present work on the characterization of turbulence was limited to turbulence of low Reynolds number. Statistical parameters, that are most often used to describe the structure of turbulence, such as mean velocity, intensity of turbulence, probability distribution function, velocity correlations, energy spectrum, energy decay at the final decay period, etc., were measured using both analog and digital methods. A close agreement was observed between the theoretical expectations and the experimental results.

I. INTRODUCTION

Hot wire and hot film anemometers are invaluable tools in the development of fluid dynamics. These anemometers are extensively used in the measurement of localized fluid flow. During the last four decades there has been a continuous improvement of this method for a better understanding of the structure of turbulent fluid flow. However, this method leaves much to be desired. Turbulence measurement with hot wire and hot film anemometers inherently requires the insertion of a finite probe in the flow field, necessarily disturbing the flow field itself. The response of a hot wire is a nonlinear function of many different physical parameters of the fluid medium, such as density, velocity, conductivity and temperature of the fluid. Its calibration often changes due to corrosion and contamination. Anemometers have thermal lag and their sensitivity decreases with the increase of turbulence frequency. They possess finite resolution both in space and time. The use of hot wire anemometers at temperatures above $300^{\circ}C$ and at supersonic flow is severely limited since a hot wire possesses less mechanical strength and increased nonlinearity of response. These and other disadvantages have led to a constant search for a more reliable method for turbulence measurement.

The application of an optical method for the measurement of non-stationary flow has been investigated by many workers in the past.[29] However, a practical and efficient method did not develop until the advent of lasers. Localized fluid flow measurement from the Doppler shift of scattered laser radiations was first observed by Yeh and

Cummins.[49] Since that time, considerable work has been reported in the field of laser Doppler velocity measurement due to its variety of potential applications, such as characterization of turbulent fluid flow, detection of clear air turbulence of the troposphere, propulsion studies, measurement of exhaust flow configuration at rocket bases, thermonuclear plasma research, etc. A laser Doppler velocity meter has the essential features of an ideal instrument to measure the structure of turbulent fluid flow. The method provides an absolute measurement of velocity and does not require any calibration. The flow field is not perturbed in the process of measurement. Its frequency response and spatial resolution are excellent. The method is applicable to both subsonic and supersonic flow regions.

In spite of these advantages over hot wire anemometers, a laser Doppler velocity meter has major limitations in certain aspects. Of these, the finite instrumental spectral broadening (δf) of the Doppler signal and low signal-to-noise ratio (SNR) are probably most important. The application of conventional methods in Doppler signal processing often fails because of these shortcomings. The finite frequency spread arises from the fact that there is a considerable uncertainty in the scattering angles due to the finite size of the transmission and the receiving apertures. In the local oscillator heterodyning process commonly used in velocity measurement, this aperture broadening of the Doppler signal is typically around 10 to 15 percent of the center frequency (f_c). Compared with a FM signal used in communication, the Doppler signal from a non-stationary flow field contains a continuous

spectrum of carrier frequencies in a range $f_c \pm \frac{1}{2}\delta f$ with the modulation component $\Delta f \cos \omega_m t$, where the frequency deviation Δf corresponds to the temporal velocity fluctuations and ω_m is the modulating frequency. Unless δf is small, frequency-to-voltage conversion becomes a difficult problem. The accuracy of measurement of Δf or the velocity fluctuations is limited by the inherent instrumental spread (δf) of the signal. For instance, the intensity of turbulence at the center of the pipe is about 3 percent of the mean velocity of the fluid at the onset of a fully developed turbulence. Instrumental frequency spread of 1 percent or above will give rise to a significant error in the measurements.

The amplitude of the Doppler signal depends on the power of the incident beam, the scattering angle and characteristics and concentration of the scattering centers present in the fluid medium. These quantities are not always controllable and often the intensity of the scattered beam is low. Further, mechanical vibration may cause a low heterodyning efficiency. These conditions may cause a low signal-to-noise ratio (SNR). Since SNR is inversely proportional to δf, reduction of instrumental broadening will have two advantages: (1) it will increase the accuracy of the system in turbulence structure characterization, and (2) it will simplify the frequency-to-voltage conversion method by increasing SNR.

Analog conversion of the Doppler frequency shifts to voltage fluctuations is desirable for discerning the statistical properties of the flow field. It is also desirable that the conversion device be simple and easy to operate so as to make the laser Doppler technique an effective and attractive tool for turbulence studies both in the subsonic and supersonic regions.

The heterodyning process commonly used in laser Doppler velocity measurement has an ambiguity of 180° in the direction of velocity. This ambiguity arises from the fact that the Doppler signal gives only the absolute value of the difference in frequency between the two waves being heterodyned. The resulting signal does not indicate whether the Doppler shift caused the scattered wave to have an upshift or a downshift in frequency with respect to the frequency of the incident beam. Velocity components equal in magnitude but opposite in sign would give the same magnitude of the Doppler frequency shift. This limitation does not adversely affect the use of this method where the direction of the mean velocity is known. However, in many cases of fluctuating velocity measurements, such information may be unknown. A heterodyning system that would eliminate this directional ambiguity is desired.

The objectives of this investigation were to make experimental and theoretical studies on the laser Doppler velocity measurement system and to solve some of the existing problems in its application in turbulence characterization. It was proposed:

(1) to develop a heterodyning system with a minimal instrumental frequency broadening and a high SNR

(2) to eliminate the directional ambiguity of 180 degrees in velocity measurement so that the Doppler shift is no longer an "even" mathematical function of the velocity measured

(3) to determine the optimum system parameters that should be used in the measurement of turbulence structure, with particular emphasis on receiving and transmission optics design and aerosol dynamics

(4) to develop a simple frequency-to-voltage conversion method

(5) to apply the laser Doppler velocity measuring system in the characterization of turbulent fluid flow.

II. LITERATURE SURVEY

Optical methods utilized in flow visualization, especially in supersonic flows, have been involved primarily in qualitative analysis. The most commonly used optical methods are schlieren systems and interferometers. Examples of the latter method are Mach-Zehnder interferometry and shadowgraphy.

Kovasznay[29] in 1949 applied the shadow method to the measurement of turbulent density fluctuations. A large number of shadow pictures are required for a quantitative analysis, and, in general, this method lacks accuracy and convenience. Although the velocity measurement of a moving target by the UHF radar technique has been known for a long time, such a technique could not be used in the localized fluid flow measurement due to the lack of a coherent radiation source in the wavelength region needed for such measurement. The first successful optical heterodyning detection was done by Forrester[14], who used two Zeeman lines of mercury for measuring the frequency difference. With classical monochromatic light sources, detection of Doppler shift below 1 GHz was not practical due to the natural line width of the sources. These difficulties were removed with the development of the laser, which provides a radiation source with a high degree of temporal and spatial coherence.

The feasibility of the laser Doppler method of velocity measurement was first demonstrated by Yeh and Cummins[49] in 1964. They used

polystyrene spheres as scattering centers in their experiment of localized fluid flow measurement in a water flow channel. Later, Foreman et al[12, 13] used this method in gas flow studies. The optical heterodyning system used in these studies consisted of beating the scattered beam with a reference beam which is usually a portion of the incident beam. It was shown that efficient heterodyning is possible between a beam scattered from irregular scattering particles and a reference beam. The method commonly referred to as "local oscillator heterodyning", requires precise optical wavefront alignment. Goldstein and Hagen[19] developed an improved version of this heterodyning technique where the beam alignment became a simple process. They employed two incident beams focused on a point of measurement, with one of these beams used as a reference beam. Goldstein and Kreid[20] were able to measure the velocity profile of a laminar water flow and, later, Goldstein and Hagen[19] reported data on the measurement of turbulent intensity in their water flow experiment using polystyrene hydrosols. Pike et al[40] later but independently developed the same heterodyning method used by Goldstein and Hagen and examined the Doppler ambiguity broadening due to the finite signal life time. They used water with milk suspension as the fluid medium.

Lennert et al[31] used the Goldstein and Hagen heterodyning method in the velocity measurement of subsonic and supersonic air flows. Their experiment was limited to one-dimensional velocity measurement. Design features of a two-dimensional velocity measurement have been discussed by Lewis and Chatterton[32]. Although Goldstein and Hagen's optical arrangement has some advantage over the system used by Yeh and

Cummins, the latter system has been studied in detail for three-dimensional velocity measurements by many workers, notably by Huffaker.[24] Huffaker reported measurement of velocity profile and turbulent intensities in the flow field of a turbulent jet. He also was able to measure atmospheric wind velocity at a range of 50 meters using a 20-watt CO_2 laser. Recent works on laminar flow[1,4,8] using the laser Doppler velocity measurement technique show that spatial resolution, previously not practicable with hot wire anemometers, can be achieved in this process.

The application of the laser Doppler method to a comprehensive study of the properties of turbulent fluid flow has not yet been reported. The primary problem encountered in this field comes from the instantaneous frequency spread of the Doppler signal. This instrumental spectral broadening results in a poor resolution and a low SNR. Further, FM demodulation of the Doppler signal becomes a difficult problem. Foreman et al[13] first analyzed this shortcoming of the laser Doppler method and suggested the use of a frequency tracking method for the signal demodulation. A quantitative study of the frequency broadening and its cause was first made by Goldstein and Hagen[19] and contemporarily by Pike et al.[40] Goldstein and Kreid[20] reported instrumental frequency broadening ranging from 2 to 30 percent of the center frequency for a laminar flow field. Davis[10] carried out a theoretical analysis of frequency spread in the local oscillator heterodyning system and found that a fractional bandwidth ($\delta f/f_c$) of 7.5 percent is expected from the transmission and receiving apertures even when small aperture sizes are used. He observed that in a laminar flow field, where it is only necessary to determine

the center of the signal spectrum, an accuracy of ±3 percent can be achieved even when the total frequency broadening is around 20 percent of the center frequency. In a turbulent flow field, however, this instrumental frequency broadening will lead to a large error. Welch and Tomme[47] were successful in measuring the probability distribution function of turbulent velocity components by using coincidence gating and a subsequent integration method for signal processing. They used liquid flow in a channel in their experimental setup and reported the typical value of signal-to-noise ratio as unity. Goldstein and Hagen's optical arrangement recently has been applied to the measurement of turbulent drag by Chung and Grable[8]. The maximum value of signal-to-noise ratio reported by them is below 3. Some variations of the heterodyning process have been reported by Rudd[43] and by Muller[36]. However, enough experimental studies have not been reported on the relative instrumental broadening in those processes.

A heterodyning system that partially eliminates frequency spread was first reported by Bond[5]. In the system used by Bond, no reference beam was used for heterodyning. Instead, two scattered beams spatially symmetrical about the incident beam were "mixed" to obtain the Doppler shift. This technique eliminates the receiving aperture broadening as long as the aperture size used in the receiving optics is small. Beam alignment procedure is critical as it is with the case of Yeh and Cummins' method of local oscillator heterodyning.

III. LASER DOPPLER VELOCITY METER EMPLOYING SYMMETRICAL HETERODYNING SYSTEM

A. Theoretical Consideration

1. Doppler shift and instrumental broadening:

When a monochromatic beam of light is incident on a moving particle, the Doppler shift of the scattered light wave can be expressed by

$$f_D = \frac{1}{2\pi} (\vec{K}_s - \vec{K}_o) \cdot \vec{V}_p \tag{1}$$

where $\vec{V}_p$ is the instantaneous velocity of the particle with respect to a frame of reference and $\vec{K}_o$ and $\vec{K}_s$ are wave vectors representing the incident and scattered waves. If $\vec{i}_o$ and $\vec{i}_s$ are the two unit vectors in the direction of propagation of the two waves and λ_o and λ_s are the wavelengths of the incident and scattered radiations respectively, and since $V_p << c$, where c is the velocity of light,

$$\lambda_o \simeq \lambda_s$$

$$|\vec{K}_s| = |\vec{K}_o| = K_o = \frac{2\pi n}{\lambda_o}$$

$$f_D = \frac{n}{\lambda_o} (\vec{i}_s - \vec{i}_o) \cdot \vec{V}_p \tag{2}$$

where n is the index of refraction of the medium. Consider that a cone of light, as shown in Figure 1, is focused on a moving particle at O having velocity component U, V, and W and a receiver with an aperture area a_R is used to obtain the scattered signal. The reference frame of cartesian coordinates OX, OY, OZ is chosen such that OX is perpendicular to the central incident wave vector TO; and OX, OS and

TO are coplaner. Considering only a single monochromatic incident wave vector along TO, the frequency of the scattered radiation along OS can be written from equation (2) as

$$\nu_s = \nu_o + \frac{1}{\lambda_o} (\vec{i}_s - \vec{i}_o) \cdot \vec{V}_p \ . \tag{3}$$

If this scattered light beam, with the angular frequency ω_s represented by $E_s \cos \omega_s t$, is superimposed with a reference beam, $E_o \cos \omega_o t$, on a square law photodetector, the output current can be represented by[42]

$$\begin{aligned} i_o &= a \left[E_o \cos \omega_o t + E_s \cos \omega_s t \right]^2 \\ &\approx a \left[\tfrac{1}{2}(E_o^2 + E_s^2) + E_o E_s \cos (\omega_o - \omega_s) t \right] \end{aligned} \tag{4}$$

where a is a constant and ω_o and ω_s are the optical angular frequencies which are well above the frequency range of the detector. The high frequency terms only contribute to a dc component in equation (4) and the ac signal arises from the difference frequency, when the absolute difference between ω_s and ω_o is within the frequency range of the detector. Perfect coherence of the two heterodyning beams has been assumed. Any deviation from this would reduce the ac component and increase the dc term. The Doppler shift f_D is a function of $\vec{V}_p$, $\vec{K}_o$, and $\vec{K}_s$. Referring to this as the center frequency f_c and expressing it in terms of U, V, W, gives, from Figure 1,

$$\begin{aligned} f_c &= \frac{1}{2\pi} |\omega_o - \omega_s| \\ &= \frac{1}{\lambda_o} (\vec{i}_s - \vec{i}_o) \cdot (\vec{U} + \vec{V} + \vec{W}) \\ &= \frac{1}{\lambda_o} (U \sin \psi - V \cos \psi - V) \ . \end{aligned} \tag{5}$$

Equation (5) shows that the measurement of f_c and ψ does not provide sufficient data to determine the direction and magnitude of velocity V_p of the particle. However, if the direction is known, the magnitude of $\vec{V}_p$ can be determined. To measure the three-dimensional components of velocity, three detectors at three different scattering angles are needed and the components are then computed by solving three simultaneous equations.

The frequency spectrum of the Doppler shift for the conical incident beam of solid angle $\Delta\emptyset$ and for the finite aperture area at S, which subtends a solid angle $\Delta\Omega$ at 0, will have a finite spread around f_c. This spread, arising from finite $\Delta\emptyset$ and $\Delta\Omega$, is the aperture broadening of the Doppler signal, and can be represented by δf_a. For a known velocity of the scattering particle, this frequency spread can be calculated. Besides this aperture broadening, there are other causes of signal broadening, such as broadening due to the finite volume of the laser beam "probe" at the effective scattering zone, broadening due to the finite lifetime of the signal, etc. These factors cause an effective instrumental frequency broadening of the Doppler signal. A significant parameter in the signal processing is the ratio of this frequency spread (δf) to the center frequency (f_c).

To examine how $\delta f_a/f_c$ varies with the system parameters, consider that W = 0 and the particle velocity $\vec{V}_p$ is constant in magnitude but varies in direction so that the angle $\emptyset$ varies from 0° to 360°. Similarly, also consider that θ is varied from 0° to 360°. From Figure 1, writing f_c in terms of θ and $\emptyset$,

$$f_c = \frac{1}{\lambda_o}\left[V_p \cos(\theta - \phi) - V_p \cos\phi\right] \quad . \tag{6}$$

From the above equation, the magnitude of the Doppler shift increases as the angle ψ decreases (Figure 1). The maximum frequency spread caused by the finite size of apertures can be approximated by taking the difference between the maximum and the minimum values of the Doppler shifts for known values of $\alpha/2$ and $\Delta\theta/2$. Thus,

$$f_{max} = \frac{1}{\lambda_o}(\vec{i}_{s1} - \vec{i}_{o1}) \cdot \vec{V}_p$$

$$= \frac{V_p}{\lambda_o}\left[\cos(\theta - \phi + \frac{\Delta\theta}{2}) - \cos(\phi + \frac{\alpha}{2})\right] \quad .$$

$$f_{min} = \frac{1}{\lambda_o}(\vec{i}_{s2} - \vec{i}_{o2}) \cdot \vec{V}_p$$

$$= \frac{V_p}{\lambda_o}\left[\cos(\theta - \phi - \frac{\Delta\theta}{2}) - \cos(\phi - \frac{\alpha}{2})\right] \quad .$$

The aperture broadening

$$\delta f_a = f_{max} - f_{min}$$

$$= \frac{2V_p}{\lambda_o}\left[\sin\phi \sin\alpha/2 - \sin(\theta - \phi) \sin\Delta\theta/2\right]$$

or

$$\frac{\delta f_a}{f_c} = \frac{2 \sin\phi \sin\alpha/2 - 2 \sin\beta \sin\Delta\theta/2}{\cos\beta - \cos\phi} \tag{7}$$

where

$$\beta = \theta - \phi \quad .$$

Equation (7) shows that $\delta f_a/f_c$ is a discontinuous function of β and ϕ. To observe the nature of variation of $\delta f_a/f_c$ with θ and ϕ, some

reasonable values of the aperture sizes can be assumed. Let $\alpha/2 = 0.165^{\circ}$ ($\sin \alpha/2 = 0.00285$) which corresponds to a transmission aperture of 4 mm diameter placed before lens L_1 having a focal length of 700 mm and let $\Delta\theta/2 = 1.15^{\circ}$ ($\sin \Delta\theta/2 = 0.02$) which would be the case if a 2 cm diameter receiving aperture is placed at a distance of 50 cm from the scattering point.

Figure 2 shows the theoretically expected values of $\delta f_a/f_c$ plotted versus θ for different values of ϕ. Figure 3 shows the effect of variation of ϕ on $\delta f_a/f_c$ for given values of θ. It is evident that $\delta f_a/f_c$ can be reduced by a proper choice of the values of θ and ϕ, although the primary determining factors for these parameters are the scattering intensity and the convenience of operation. The scattering intensity falls off rapidly as θ is increased. In forward scattering measurements θ is maintained somewhere between 5° and 45° and ϕ between 45° and 135°. Figure 4 shows the variation of $\delta f_a/f_c$ with θ and ϕ in this region of practical interest.

Once θ and ϕ are determined, the fractional bandwidth $\delta f_a/f_c$ becomes a function of α and $\Delta\theta$. Equation (7) shows that, if $\Delta\Omega$, i.e. the size of the receiving aperture at S, is increased, the aperture broadening will also increase. This sets up an upper limit in increasing the aperture size for a higher signal power.

In a local oscillator heterodyning process, a scattered beam from a moving object is mixed with a portion of the incident beam to generate the Doppler signal. A typical experimental setup is shown in Figure 5. Referring to equation (4), observe that, if $E_o >> E_s$,

the maximum signal-to-noise ratio that can be achieved in this process is

$$SNR = \frac{C(\nu_o, \varepsilon, \eta)}{\delta f_\ell} \cdot P_s \quad . \tag{8}$$

The quantity C is a constant depending on the laser radiation frequency ν_o, quantum efficiency ε of the detector and heterodyning efficiency η, and P_s is the power of the scattered beam falling on the photodetector. The bandwidth δf_ℓ is the total instrumental frequency spread of the Doppler signal. Equation (8) indicates that an increase in the receiving aperture for a higher value of P_s may not result in a higher value of signal-to-noise ratio since δf_ℓ increases with the increase of receiving aperture size.

There are three disadvantages of the local oscillator heterodyning system: (1) critical alignment procedures are required in the beam superposition so that the total path difference across the width of the beam is less than $\lambda/4$; (2) a large aperture broadening is present in the Doppler signal; and (3) measurement of direction and magnitude of the velocity requires more than one detector assembly. The modified beam optics developed by Goldstein and Hagen[19] do not require critical alignment procedures. In addition, the velocity component in a chosen direction can be measured with a single detector. However, aperture broadening remains the same.

The heterodyning system developed by Bond[5] is effective in partial elimination of the aperture broadening. The experimental setup used by Bond is shown in Figure 6. In this process, two scattered beams are

mixed to generate the Doppler signal as shown in Figure 6. The locations of the two apertures used to receive the scattered light are symmetrical about the direction of propagation of the incident beam so that the Doppler shifts in these two scattered beams are equal in magnitude but opposite in sign. The sine curve of Figure 6 shows the Doppler shift plotted versus the scattering angle for a constant velocity component U. The superposition of the two scattered beams on the photodetector results in a Doppler signal whose center frequency f_c is sensitive only to the velocity component U, in the direction OX, which is coplaner to the two scattered beams and perpendicular to the bisector of the angle θ subtended by the two scattered beams at the point O. If the spread of the Doppler frequency shift across the two apertures is within the linear portion of the curve, spatial superposition of the two beams will give the same difference frequency across the photocathode surface and result in cancellation of the receiver aperture broadening. Elimination of this broadening will not be effective if the aperture sizes are large since the constraint that the Doppler shift across the aperture should be linear will not be satisfied. Similar to the local oscillator heterodyning process, this method also requires tedious beam alignment for a high heterodyning efficiency. This imposes a rather stringent requirement on the mechanical rigidity of the system.

2. Symmetrical heterodyning system:

Figure 7 shows the experimental arrangement of a two-incident-beam symmetrical heterodyning system developed under the present study.

Two incident beams are focused at the point O making an angle θ. The scattered beam from the moving particles directly generates the desired Doppler signal. The process actually involves heterodyning of the wave vectors scattered from the two incident beams. No further beam superposition is necessary. To calculate the Doppler shift, consider the arrangement shown in Figure 7. The frequency of the scattered beam in an arbitrarily chosen direction OS, Doppler shifted with respect to the incident wave vector $\vec{K}_{01}$, can be written as

$$\nu_{c1} = \nu_o + \frac{1}{\lambda_o}(\vec{i}_s - \vec{i}_o) \cdot (\vec{U} + \vec{V} + \vec{W})$$

$$= \nu_o + \frac{1}{\lambda_o}(V \cos \beta - U \sin \beta - U \sin \frac{\theta}{2} - V \cos \frac{\theta}{2}) \quad (9)$$

where ν_o and λ_o are the frequency and wavelength of the incident radiation. Similarly, the Doppler shift with respect to the incident wave vector $\vec{K}_{02}$ can be written as

$$\nu_{c2} = \nu_o + \frac{1}{\lambda_o}(\vec{i}_s - \vec{i}_o)(\vec{U} + \vec{V} + \vec{W})$$

$$= \nu_o + \frac{1}{\lambda_o}(U \cos \beta - U \sin \beta + U \sin \frac{\theta}{2} - V \cos \frac{\theta}{2}). \quad (10)$$

Thus, the scattered wave along OS has two components whose frequencies are ν_{c1} and ν_{c2}. When this scattered wave is incident on a photodetector, the generated signal will have the frequency given by the absolute difference of ν_{c1} and ν_{c2}. From equations (9) and (10),

$$f_c = |\nu_{c1} - \nu_{c2}|$$

$$= \frac{2U}{\lambda_o} \sin \frac{\theta}{2} \quad . \quad (11)$$

It is evident from equation (11) that the signal frequency f_c is independent of the angle ψ or the spatial position of the receiving aperture. Thus, the receiving aperture broadening

$$\delta f_{\Delta\Omega} = 0 \tag{12}$$

where $\Delta\Omega$ is the solid angle subtended by the receiving aperture at the point of velocity measurement.

The receiving aperture area can be increased to increase the signal strength (P_s) to any desired level without increasing the instrumental broadening of the signal. The only aperture broadening will be due to the finite size of the transmission aperture. It can be shown readily that

$$\delta f_a = \delta f_{\Delta\phi} = \frac{4\sqrt{U^2 + V^2}}{\lambda_o} \sin\frac{\alpha}{2} \cos\frac{\theta}{2} \quad . \tag{13}$$

The angle α (or the solid angle $\Delta\phi$) as shown in Figure 7 depends on the spot diameter of the laser beam and the focal length of the lens used in the transmission optics. Thus, δf_a can be made quite small. Equation (11) also shows that the measured Doppler shift is a function of velocity component U only, the direction of which is perpendicular to the bisector of angle θ and coplaner to $\vec{K}_{01}$ and $\vec{K}_{02}$. By changing the spatial orientation of the two beams incident at 0, any one of the three orthogonal velocity components can be measured. Alignment is simple. Thus, the loss in heterodyning efficiency due to beam misalignment is negligible since the system is less sensitive to small mechanical vibrations. The transmission of the scattered beam through the turbulent fluid medium does not affect the heterodyning efficiency.

Due to the small instrumental broadening of the signal, the accuracy of measurement is higher compared to the local oscillator system. In the following analysis, the two-incident-beam heterodyning system will be referred to as the "symmetrical heterodyning system".

3. Signal-to-noise ratio:

Signal-to-noise ratio in ideal photomixing has been investigated by several workers[22,35,37] and their studies reveal two important aspects: (1) it is possible to operate a photomultiplier as an ideal receiver, i.e., SNR at the output will be limited by that of the incident light falling on the photocathode; and (2) if the signal bandwidth is very small it should be possible to detect a signal below the noise equivalent power (NEP) of the detector.

In the heterodyning system described above, the signal-to-noise ratio can be expressed as

$$\text{SNR} \simeq \frac{i_s^2 R_L}{4KT\delta f + 2q\langle i_d\rangle \delta f R_L + 2q\langle i_b\rangle \delta f R_L + 2q i_{dc} \delta f R_L + a(e_n^2/R_L)} \qquad (14)$$

where i_s is the signal current through the load resistor R_L. The first four terms in the denominator represent thermal noise, dark current noise, stray light noise and shot noise respectively. The last term represents the inherent noise in the signal, which determines the maximum possible signal-to-noise ratio attainable and needs to be considered only when the signal power P_s is quite large.

In the local oscillator heterodyning method, thermal noise, stray light noise and dark current noise can be made insignificant compared to the shot noise in the photomultiplier by increasing the reference

beam intensity. Under these conditions,

$$SNR \approx \frac{C(\nu_o, \varepsilon, \eta)}{\delta f_\ell} \cdot \frac{P_s}{1 + (P_s/P_L)} \tag{15}$$

where the constant C depends on the laser frequency ν_o, quantum efficiency ε, and heterodyning efficiency η. The effective bandwidth, δf_ℓ, is determined by the instrumental signal broadening. The quantities P_L and P_s are the reference beam and signal beam powers respectively. When $P_L >> P_s$,

$$SNR \approx \frac{C(\nu_o, \varepsilon, \eta)}{\delta f_\ell} \cdot P_s \tag{16}$$

as was noted previously in equation (8). In the symmetrical system, no reference beam is used but noise supression is effected by increasing the signal power itself. In this system of heterodyning the signal power P_s can be increased by increasing the receiving aperture area which does not affect the instrumental frequency broadening. From equation (15), with $P_L = P_s$,

$$SNR \approx \frac{C(\nu_o, \varepsilon, \eta)}{2\delta f_S} \cdot P_s \tag{17}$$

where δf_S is the instrumental signal line width of the symmetrical heterodyning system. In most laboratory scale applications, $2\delta f_S$ will be smaller than δf_ℓ, resulting in a SNR value higher or equal to the level obtained in the local oscillator system, depending on the relative values of instrumental broadening and the signal power. In equation (17), it is observed that SNR increases with the signal power P_s. The above is true until the noise in the signal becomes a limiting

factor. When the signal power is high, it is this noise which determines the value of SNR in most practical cases. This quantity was represented in the last term of the denominator of equation (14) and was not considered in deriving equations (16) and (17). Noise in the signal comes from different sources. Probably the major contributions are from: (1) inefficient heterodyning arising from the misalignment of the two incident beams and unequal intensity distribution between the two beams; (2) coherence loss and random phase scattering; (3) imperfections in optics and the transmission path of the incident and the scattered beams through the dispersing and absorbing media; (4) plasma noise and mode interference noise in the laser output; and (5) intensity fluctuations of the laser beam.

To prevent unwanted scattered light from falling on the photocathode surface, a spatial filter can be used in the receiving optics. In the fluid flow studies, the entire path of the two incident beams within the fluid medium is illuminated by the scattering aerosols present in the fluid medium. Since the effective Doppler signal originates only from the beam intersection, scattered light from any other portions of the beam would generate noise. A spatial filter can minimize this background scattering radiation. The efficiency of such a filter is better if $\theta/2$ is large, a criterion that reduces signal beam intensity. However, a large aperture area can be used to obtain the desired value of P_s.

B. Laser Doppler Velocity Measurement Without Directional Ambiguity by Using Frequency Shifted Incident Beams

The heterodyning processes described before for Doppler velocity measurements have an ambiguity of 180° in the direction of velocity. From equations (6) and (11) it is found that the Doppler signal frequency is the absolute value of the difference in frequency between the two heterodyned wave vectors. A heterodyning system developed by the present study eliminates this directional ambiguity by incorporating a frequency bias so that the Doppler shift is no longer an "even" mathematical function of the velocity measured.

If the two incident beams of the symmetrical heterodyning system are of two slightly different frequencies, it is possible to measure velocity without directional ambiguity. This frequency shift can be accomplished by employing a rotating diffraction grating or a Bragg cell. Consider a reflection grating replica mounted along the circumference of a disk, which is rotated at a constant angular velocity. An experimental arrangement is shown in Figure 8. If a laser beam is incident on the diffraction grating at 90°, the frequency of the Doppler shifted +1 order diffracted beam can be written as

$$\nu_{+1} = \nu_o + \frac{1}{2\pi} (\vec{K}_s - \vec{K}_o) \cdot \vec{V} \tag{18}$$

$$= \nu_o + \frac{V}{\lambda_o} \sin \beta \tag{19}$$

where ν_o is the frequency of the incident laser beam, $\vec{K}_s$ and $\vec{K}_o$ represent the wave vectors of the scattered and the incident radiations respectively, and V is the magnitude of the liner velocity of the

rotating diffraction grating. Here β is the angle subtended by the first order beam with the normal incident beam. The frequency of the -1 order beam is

$$\nu_{-1} = \nu_o - \frac{V}{\lambda_o} \sin \beta \quad . \tag{20}$$

When these two beams are focused on the moving scatterer at "0" (Figure 8), the Doppler shift measured by the detector for a velocity component U of the moving scatterer is given by

$$f_{c+} = \nu_{+1} - \nu_{-1} + \left(\frac{U}{\lambda_{+1}} - \frac{U}{\lambda_{-1}} \right) \cos \psi + \left(\frac{U}{\lambda_{+1}} + \frac{U}{\lambda_{-1}} \right) \sin \frac{\theta}{2}$$

$$\simeq f_o + \frac{2U}{\lambda_o} \sin \frac{\theta}{2} \tag{21}$$

where

$$f_o = \nu_{+1} - \nu_{-1}$$

and by noting that $U/\lambda_{+1} \simeq U/\lambda_{-1} \simeq U/\lambda_o$. The quantity U is the velocity in the +x direction which is in the plane of the two incident beams at O and perpendicular to the bisector of the angle θ. For a velocity U in the -x direction, the corresponding shift can be written as

$$f_{c-} = f_o + \left(\frac{U}{\lambda_{-1}} - \frac{U}{\lambda_{+1}} \right) \cos \psi - \left(\frac{U}{\lambda_{+1}} + \frac{U}{\lambda_{-1}} \right) \sin \frac{\theta}{2}$$

$$\simeq f_o - \frac{2U}{\lambda_o} \sin \frac{\theta}{2} \quad . \tag{22}$$

Equations (21) and (22) show that the directional ambiguity of 180° no longer exists. The Doppler shift is independent of the scattering angle (ψ) or the spatial position of the detector. Thus, the frequency biasing does not affect the advantages gained using the symmetrical system. This technique also will be equally effective in a local

oscillator heterodyning process in eliminating the directional ambiguity. However, a symmetrical system will have a high SNR and a minimal instrumental spectral broadening. By changing the orientation of the spatial position of the two incident beams, velocity components along the y and z direction can be measured in a similar manner. The frequency bias f_o can be adjusted by changing the angular speed of the rotating diffraction grating.

One of the annular tracks of an optical encoder disk can also be used as a rotating grating. In the case of a reflection grating mounted along the circumference of a disk and the laser beam incident normal to the edge, there is an appreciable distortion of the diffracted orders due to the finite curvature of the grating surface. The use of an encoder disk eliminates this distortion since the laser beam is incident normal to the face of the disk.

The loss in intensity of light in other diffracted orders, which is considerable since only two orders are used, can be partially eliminated by using a special blazed grating. The mechanical vibration of the rotating grating may also cause a loss in the heterodyning efficiency owing to the fluctuations in degree of alignment of the two incident beams at the scattering point "0". These disadvantages will be removed if a Bragg cell[28, 48] is used for frequency shifting, as shown in Figure 9. In this case an ultrasonic transducer is used to generate a traveling acoustical wave in a water cell. When Bragg reflection conditions[48] are satisfied, 90 percent of the incident energy can be transferred to the -1 order beam.[28] For the first order mode the incident beam and the diffracted order are at the Bragg

angle with the normal to the cell, and the frequency shift is ν_s, the frequency of the acoustic wave.

C. Characteristics of the Doppler Signal from Fluctuating Flow Field

1. General considerations:

The frequency shift of the Doppler signal can vary from zero to several hundred megahertz depending on the mean velocity of the fluid and the system parameters used. The Doppler shift will have random fluctuations about the mean value, which increase with the relative intensity of turbulence. Fluctuations ranging from zero to 10 percent of the mean value are common. The rate of change of frequency may vary from a low value to 20 kHz or higher. Thus, the frequency modulation index β may vary from a small fraction to several hundred, and in a random fashion. Besides having the large static and dynamic ranges of frequency variations and a wide variation of β, a laser Doppler signal has an appreciable frequency spread arising from instrumental broadening. Different causes for the instantaneous broadening of the signal have been mentioned previously. The major sources of instrumental frequency broadening in a symmetrical heterodyning process are: (1) transmission aperture broadening (δf_a); (2) spread due to the finite lifetime of the signal (δf_T); and (3) frequency spread arising from the velocity gradient present within the effective scattering volume (δf_s). Of all the sources of instrumental spectral broadening of the signal, the one which causes the largest spread determines the total effective frequency spread (δf) of the signal. In other words, the components of the total frequency spread δf_a, δf_s, δf_T, etc. are not expected to be additive to comprise the effective spread δf.

A typical Doppler signal is shown in Figure 10. Figure 10a shows the finite spectrum of the signal in the frequency domain and Figure 10b shows the finite width of the waveform in the time domain. The velocity of the scatterer was maintained constant in the above representations. In a non-stationary flow field, this spectrum of continuum band of "carrier" is frequency modulated by the velocity fluctuations of the scatterers. This multiplicity of the "carrier" frequency obviates the use of conventional frequency discriminators in processing the Doppler shift output without further signal conditioning.

Reduction of the instrumental broadening of the Doppler signal will have two advantages: (1) it will increase the accuracy of the system in turbulence structure measurement; and (2) it will increase SNR and, hence, frequency-to-voltage conversion will be possible by a comparatively simple method.

2. Minimization of the instrumental spread:

The aperture broadening in a symmetrical system comes from the transmission aperture. From equations (11) and (13),

$$\frac{\delta f_a}{f_c} \simeq 2 \sin \frac{\alpha}{2} \cot \frac{\theta}{2} \tag{23}$$

assuming $V = W = 0$. Figure 11 shows the effect of increasing θ for different values of α. If Figure 11 is compared with the aperture broadening in a local oscillator heterodyning system, plotted in Figure 4, it is found that the signal broadening is appreciably less in the symmetrical heterodyning system. For example, consider $\theta = 30^\circ$ and $\phi = 90^\circ$ in the local oscillator heterodyning system. From Figure 4, it is found that an aperture broadening of 8 percent of the center

frequency f_c is expected. In the symmetrical heterodyning system, this scattering angle would correspond to $\theta = 60^\circ$ for the velocity component U. The expected frequency spread is approximately one percent in this case. The values of $\alpha/2$ and $\Delta\theta/2$ considered in this example were 0.165° and 1.15° respectively.

Increasing θ reduces the aperture broadening and also decreases the effective length (ℓ) of the laser beam "probe" (sensing volume or the effective scattering volume). This means that increasing θ would also result in a decrease of δf_s, the frequency spread arising because of the presence of the velocity gradient in the sensing volume. The frequency spread arising from the finite size of the sensing volume can be calculated by determining the effective sensitive length (ℓ) of the laser beam "probe" and from the expected average spatial velocity gradient (δu cm/sec/cm) at the point of measurement. Since

$$\frac{\delta f_s}{f_c} = \frac{\delta u \ell}{\overline{U}} \tag{24}$$

where $\overline{U}$ represents the average velocity along the longitudinal axis (x) of the wind tunnel. The maximum value of the spread δf_s will come from the spatial velocity gradient of the fluctuating velocity component u' ($=\sqrt{\overline{u^2}}$) along the lateral axis (y) of the wind tunnel. An expected value of this gradient can be computed by determining the Reynolds number (Re) and the microscale of turbulence λ. For example, considering the experimental data reported by Laufer[30] for the values of Re ranging from 15,000 to 30,000, the spatial velocity gradient can be estimated.

$$\frac{u'}{\overline{U}} = 0.04, \quad \overline{U} = 100 \text{ ft/sec}, \quad \lambda_y = 0.25 \text{ cm}$$

$$\left(\frac{\overline{\partial u}}{\partial y}\right) = 500 \text{ sec}^{-1} \tag{25}$$

giving an approximate velocity gradient in the lateral direction in a moderate intensity of turbulence. The sensitive length, ℓ, can be estimated assuming diffraction limited optics:

$$\ell = \frac{2.44\ \lambda_o}{2 \sin\frac{\alpha}{2} \sin\frac{\theta}{2}} \tag{26}$$

where λ_o is the wavelength of the incident laser beam.

From equation (24)

$$\frac{\delta f_s}{f_c} = \frac{\ell \cdot \left(\frac{\overline{\partial u}}{\partial y}\right)}{\overline{U}} \ . \tag{27}$$

Figure 12 shows the expected variation of δf_s plotted against θ, assuming a velocity gradient of 500 sec^{-1} in the flow field. An increase in θ would give rise to higher values of f_c (equation 11) and Δf (frequency deviation arising from velocity fluctuations) for a given mean velocity and turbulence intensity, thus necessitating a larger static and dynamic frequency range of the demodulator. Further the reflection loss from the optical window of the wind tunnel will also increase. The nature of the variation of this reflection loss from the optical window is shown in Figure 13 for glass and lucite windows.

Figure 14 shows the variation of δf_a and δf_s as a function of $\alpha/2$. While the transmission aperture broadening decreases with $\alpha/2$, the spread due to the finite scattering volume increases. This is due to

the increase in the focal volume, since the blur diameter at the focal point increases as the aperture size in front of the lens decreases. For a known value of θ and the average velocity gradient in the flow field, the convergence angle α or the incident aperture diameter can be optimized. In Figure 14, $\alpha_1/2$ indicates such an optimum value of the convergence angle for $\theta = 60^{\circ}$. The theoretically expected value of the effective instrumental broadening of the signal due to δf_a and δf_s is approximately 1 percent of the center frequency.

3. Scattering volume:

In turbulence characterization, the size of the laser beam "probe" or the effective scattering zone within the flow field should be small compared to the microscale of turbulence but large enough to contain scattering particles at all times during the period of measurements. The latter condition would provide adequate signal strength and signal continuity in time while a reasonable concentration or aerosol is used in the fluid medium. As mentioned earlier, a large sensing volume introduces an appreciable spectral broadening (δf_s) due to the spatial velocity gradients.

The size of the sensing volume depends both on the transmission and receiving optics. This is illustrated in Figure 15. The sensing volume, where the two incident beams are crossing, can be reduced to a minimum if diffraction limited optics are used. This is not easily achieved in the transmission optics since a large f-number is normally used. The blur diameter D_B and the focal tolerance Δz can be determined from diffraction theory.

$$D_B = 2.44 \frac{f_1}{D_T} \lambda_o \tag{28}$$

$$\Delta z = \left(\frac{f_1}{D_T}\right)^2 \cdot \lambda_o \tag{29}$$

where D_T is the transmission aperture diameter, f_1 is the focal length of the lens L_1 and λ_o is the wavelength of incident radiation. If the incident beams are **crossing** at 0 at an angle θ, as shown in Figure 15, the volume of these two focused beams is

$$V = 8 \int_0^{\frac{D_B}{2}} \int_0^{\sqrt{\frac{D_B^2}{4} - z^2}} \int_0^{\frac{\sqrt{\frac{D_B^2}{4} - z^2}}{\sin\theta} + \frac{x}{\tan\theta}} dydxdz$$

$$= \frac{2}{3} D_B^3 \left(\frac{1}{\sin\theta} + \frac{1}{2\tan\theta}\right) . \tag{30}$$

The effective scattering zone is the portion of this volume intersected by the depth of field of the imaging optics. If the receiving optics are in the same plane and in the forward scattering direction, a probable shape of the "probe" will be as indicated in the bottom of Figure 15. To make the sensing volume small, the lenses L_2 and L_3 should have minimum spherical aberrations. If uncorrected lenses are used, the lateral spherical aberration would determine the effective diameter (d) of the "probe". For example, if one chooses a plano-convex lens for L_2 to have a minimum spherical aberration, the effective diameter d can be calculated according to the third order spherical

aberration theory.[26] The position factor p = -1, where p is defined by

$$p = \frac{y' - y}{y' + y}$$

where y' is the image distance and y is the object distance considering the reversibility of rays. The shape factor q = +1, where

$$q = \frac{r_2 + r_1}{r_2 - r_1} \quad .$$

Here, r_1 and r_2 are the radii of curvature of the first and second surfaces of the lens with the usual sign conventions. With the above two values, the effective diameter d will be determined by the lateral spherical aberration.

$$d = S_p h L_s \tag{31}$$

where S_p is the image distance for the paraxial rays, h is the maximum height of the rays above the optical axis, and

$$L_s = \frac{h^2}{8 f_2^3} \cdot \frac{1}{n(n-1)} \left[\frac{n+2}{n-1} q^2 + 4(n+1)pq + (3n+2)(n-1)p^2 + \frac{n^3}{n-1} \right]$$

where f_2 is the focal length of the lens L_2, and n is the refractive index of the glass used. From Figure 15, the following approximation can be made.

$$R \simeq S_p$$

$$h = R \tan \Delta\theta/2$$

and substituting these values and putting n = 1.6, equation (31) can be written as

$$d \simeq \frac{1.7 R^4 \tan^3 \frac{\Delta\theta}{2}}{f_2^3} \tag{32}$$

where R is the distance from the center of the scattering zone to the lens L_2, $\Delta\theta/2$ is the half angle subtended by the receiving aperture at "0" and f_2 is the focal length of lens L_2. Figure 16 shows the effect of variation of $\Delta\theta$ on d. The lower limit is set by the diffraction limit and the upper limit is set by the dimension D determined by the transmission optics. The common diameter of the beam intersection is D, which can be calculated from equation (28).

$$D = \frac{D_B}{\cos(\theta/2)} = \frac{2.44\ \lambda_o}{2\ \sin(\alpha/2)\ \cos(\theta/2)} \quad . \tag{33a}$$

Similarly, the length ℓ can be calculated as

$$\ell = \frac{2.44\ \lambda_o}{2\ \sin(\alpha/2)\ \sin(\theta/2)} \quad . \tag{33b}$$

A simple method of partial elimination of the spherical aberration is to use a doublet consisting of one positive and one negative lens.[26] A combination of hand corrected lenses can be used for complete elimination of the spherical aberration. The latter is shown as diffraction limit in Figure 16. The length (ℓ) of the laser beam "probe" would depend normally on the transmission optics since on-axis rays will not be blocked by the spatial filter as shown in Figure 15. However, if the optical axis of the spatial filter is tilted in a plane perpendicular to the plane containing the transmission optical axis, the effective length (ℓ) can be further reduced. The length (ℓ) decreases also with the increase of the angle θ. The nature of the variation of the length ℓ is plotted versus θ in Figure 17. For example, if $\theta = 60^\circ$, $f_1 = 700$ mm, $D_T = 4$ mm, $D_R = 40$ mm and $\Delta\theta = 10^\circ$, the sensing volume can be characterized by

ℓ = 550 microns

d = 4.5 microns

considering diffraction limited optics. The effective sensing volume is thus approximately 1 x 10^{-8} cm^3. This volume compares favorably with the dimension of a typical hot wire probe (wire diameter 10 microns, length 1.5 mm, probe diameter 3 mm). Consider a uniform aerosol concentration of 10^8 particles/cm^3 in the fluid medium; the effective volume as calculated above would roughly contain 1 to 2 particles. This concentration insures a satisfactory signal continuity in time which means that the frequency spread (δf_T) arising due to the finite lifetime of the signal should be small. As described later, the scattering intensity with 1 to 2 particles within the sensing volume will be adequate for a high SNR. For example, using a 50 mW laser and with the scattering angle ($\theta/2$) = 30°, the scattering intensity at a distance of 50 cm from the sensing volume will be approximately 10^{-7} watt/particle for an average particle diameter of 1 micron.

Considering a typical value of the microscale of turbulence as 1 mm,[23] the size of the effective sensing volume appears to be satisfactory for the desired spatial resolution. However, unlike a hot wire probe, where the effective velocity measured is the average value of fluid velocity over the sensitive length of the wire, a laser Doppler velocity meter generates a signal having frequency components corresponding to the total velocity distributions present in the sensing volume.

The foregoing discussions are based on the assumption that the intensity distribution of the incident beams across the transmission

apertures is constant. In practice, intensity distribution will be Gaussian. However, it is found that this does not change the above results significantly enough to warrant an exact analysis.

4. Signal lifetime:

If the aerosol concentration is low, the Doppler signal may become discontinuous in time. This time discontinuous signal would give an effective frequency spread of the signal, even when $\delta f_a = \delta f_s = 0$. The latter condition is realized when two plane parallel beams ($\alpha = 0$) are crossing at angle θ and there is no spatial velocity gradient within the sensitive scattering zone. Such a condition can probably be achieved in a laminar fluid flow. If the aerosol concentration is such that, in general, each scattering particle is crossing the sensing volume in a discrete manner, then the signal would arrive at the photocathode as short duration bursts. Now, if the velocity of the particles is a function of time, such as in an oscillatory laminar flow or turbulent fluid flow, then the accuracy of measurement of the corresponding frequency shifts would depend on the number of cycles present in the time T and repetition time T_c. If the velocity of the particles is constant, the case is analogous to the case of pulse code modulation, where the modulated carrier can be expressed as

$$M(t) = KE \left[\cos \omega_c t + \sum_{n=1}^{\infty} \frac{\sin (nk\pi)}{(nk\pi)} \left\{\cos (\omega_c - n\omega_r)t + \cos (\omega_c + n\omega_r)t\right\}\right]. \quad (34)$$

The carrier signal is represented by $E_{cm} \cos \omega_c t$ and ω_r represents the repetition frequency, which in the present case will depend on the number concentration of aerosol per cc. In the above equation $k = T/t_c$

and, for $T << T_c$, the effective signal bandwidth is $2/T$. The nature of this signal burst and the corresponding bandwidth in the frequency domain are shown in Figure 18 for a qualitative study. In a turbulent flow field, T_c will decrease with the increase of aerosol concentration since the number of bursts of a given frequency (e.g. f_{c1}, f_{c2}, etc.) increases. In the frequency domain, this would mean that the relative amount of energy contained in the higher frequency range of the Doppler signal spectrum would increase. When the scattering volume contains more than one particle, T_c approaches T, and the individual signal bursts superimpose at a random phase, giving rise to an amplitude modulation of the FM signal. The signal, in this case, will probably be continuous in time. An AGC amplifier can be used to improve the signal condition before the signal is applied to the frequency-to-voltage converter.

In practice, however, the signal waveform will be more complex than the above simplified presentation. In general, the effective frequency spread (δf_T) can be written in terms of T,

$$\delta f_T = \frac{k}{T} \quad ,$$

where k is a constant depending on the aerosol concentration and the scattering process. In the symmetrical heterodyning system, with the two incident beams crossing at an angle θ and with a finite angle of convergence α, the path length d of the scattering aerosol within the sensing volume is given by equation (33). Since,

$$T = \frac{d}{\bar{U}} \tag{35}$$

$$\delta f_T = \frac{K}{T} = \frac{2 \bar{U} k \sin(\alpha/2) \cos(\theta/2)}{2.44 \lambda_o} \tag{36}$$

or

$$\frac{\delta f_T}{f_c} \simeq K' \sin(\alpha/2) \cot(\theta/2) \quad . \tag{37}$$

Comparing this expression with equation (23), it is observed that the effect of adjusting the system parameters α and θ would equally affect both δf_a and δf_T. A further discussion on these two instrumental broadenings based on the formation of an interference fringe pattern is given in Appendix I.

The minimum aerosol concentration of the fluid medium that can be used in turbulence characterization would depend on the maximum value of the turbulence frequency spectrum, f_m, provided the frequency-to-voltage converter can measure the frequency of a single burst. Writing this in terms of T_c, the sampling interval,

$$\frac{1}{T_c} \geq 2 f_m \tag{38}$$

for recording the velocity fluctuations associated with the smallest eddies of the flow field. The number of cycles present in a single burst of duration, T, can be calculated from the effective diameter d and the spatial frequency of the interference fringes formed in the effective scattering zone (Appendix I).

$$\text{Number of cycles} = \frac{2 \sin \theta/2}{\lambda_o} \cdot d$$

$$\simeq 7 \text{ cycles}$$

for $\theta = 60^{o}$ and $\lambda_o = 6328$ A and d = 4.5 microns. Obviously, the number of cycles present in a single burst is independent of the frequency (f_c) of the Doppler shift. The time period T of the signal changes with the particle velocity U (equation (35)) containing the same number of cycles.

5. Amplitude modulation of the Doppler signal:

As discussed previously, the amplitude of the Doppler signal fluctuates since each particle scattering is a discrete process. In the foregoing discussion it was assumed that there was uniform distribution of homogeneous aerosol in the fluid medium. In practice, aerosol will be heterogeneous in size, shape and concentration. This would produce further amplitude modulation of the signal. The macro- and micro-fluctuations of the refractive index of the turbulent fluid medium would also cause a corresponding change in the intensity of the scattered electromagnetic wave. Temporal fluctuations of the laser beam intensity also introduce amplitude fluctuations in the signal strength. Amplitude fluctuations greater than a certain level cause errors in the demodulation stage. In general, it is desired to keep the fluctuation below the level which is rejected by the frequency discriminator.

It is interesting to note that the intensity fluctuation arising due to the density fluctuation of the turbulent fluid medium contains information about the spatial distribution of velocity and density fluctuations. Some correlation studies based on intensity fluctuation spectroscopy have been reported by Bourke et al[6]. Experimental work on the measurement of density fluctuation of a turbulent fluid medium using this method has not been reported.

D. Aerosol Dynamics and Optical Properties

Localized fluid flow measurement using a laser Doppler method implies that there must be some scattering center present in the fluid medium. The scattering cross section of molecules is smaller than that of the submicron aerosol by many orders of magnitude. As a result, it is desired that some contaminants be present in the fluid to serve as the scattering centers. These impurities can be present naturally or deliberately introduced into the flow system.

1. Aerosol size:

The size of the scattering aerosol suspended in the fluid medium should be small enough to follow the turbulent fluctuations of the fluid motion. If the particle inertia is large, such that it travels an appreciable distance independently, the particle will not follow the small eddies in the fluid. A measure of the particle inertia is its stop distance,

$$s = \tau_p V_p \tag{39}$$

where s is the stop distance of the particle for it to come to rest when projected into still air with velocity V_p. The quantity τ_p is the relaxation time[9,15,17] of the particle, which can be defined as the time required for a particle to acquire 63.2 percent of its final velocity from its position of rest when suddenly subjected to a laminar air flow of constant velocity. Neglecting Cunningham's correction factor[21], the relaxation time can be calculated from Stokes law,

$$\tau_p = \frac{m_p}{6\pi r_p \eta} \tag{40}$$

where m_p is the mass of the particle, r_p is its radius and η is the viscosity of air, all in cgs units. How closely a suspended aerosol particle will follow the turbulent eddies would depend upon the ratio of the particle stop distance to the scale of turbulence. This ratio should be small for the particle to follow the fluid motion. In calculating the stop distance of a particle placed in a turbulent flow field, the root mean square of the turbulent velocity components should be considered. Therefore,

$$s = T_p \sqrt{\overline{u^2}} \tag{41}$$

Considering homogeneous and isotropic velocity perturbations in a turbulent flow field, the associated rms value of the velocity fluctuation can be estimated for a given Reynolds number following Kolmogorov's theory.[23] The velocity fluctuation associated with the smallest scale of turbulence can be represented by

$$u_s' = \frac{\bar{U}}{(Re)^{\frac{1}{4}}}$$

$$s = T_p \, u_s' \quad . \tag{42}$$

Figure 19 shows the stop distance plotted against the particle diameter for two values of Reynolds number. From the experimental work of Laufer[30] on the scale of turbulence in subsonic flow regions, it appears that a stop distance of $s \leq 100$ microns is acceptable in turbulence characterization. A further insight to this problem can be gained if it is considered that the relaxation time T_p should be

compatible with the highest frequency of significance in the turbulence energy spectrum. If one assumes a high frequency limit of 20 kHz in turbulence fluctuation[23], the corresponding particle relaxation time

$$T_p = 5 \times 10^{-5} \text{ sec} . \tag{43}$$

Obviously, the desired size of aerosol is one that will follow the motion of an element of fluid but will not participate in the random motion of the gas molecules. Submicron particles have an appreciable Brownian movement. The mean square Brownian displacement of a particle can be written as[21]

$$\overline{\Delta x^2} = \frac{2 R T}{6\pi N \eta r_p} \cdot t \tag{44}$$

and the instantaneous velocity of the particle in temperature equilibrium with the gas molecules

$$v_B = \left(\frac{2 kT}{m_p}\right)^{\frac{1}{2}}$$

where R is the gas constant, T is the absolute temperature, t is the time in seconds, η is the viscosity of the medium, N is Avogadro's number, r_p is the radius of the particle and k is the Boltzman constant. The rms amplitude of displacement for unit density spherical particle diameter of scattering aerosol should be such that $\overline{\Delta x^2}$ and s are minimum.

2. Scattering characteristics:

Evaluation of the scattering characteristics of aerosols in the fluid medium can be made from the Mie theory if the aerosol size distribution and the optical properties are known. For an optically

isotropic spherical particle, the intensity of the scattered beam at angle θ measured from the direction of the incident beam of intensity I_o can be expressed as [21,27]

$$\frac{I(\theta)}{I_o} = \frac{\lambda_o^2}{8\pi^2 R^2} \left[i_1(a_n, b_n, \alpha_p, m, \theta) + i_2(a_n, b_n, \alpha_p, m, \theta) \right] \quad (45)$$

where R is the distance of observation. The intensity functions i_1 and i_2 have solutions in the form of infinite series of Bessel and Hankel functions and Legendre polynomials of the size parameter α_p $(= \frac{2\pi r_p}{\lambda_o})$, refractive index m, and the Mie coefficients of the electric and magnetic waves a_n and b_n respectively. Mie coefficients can be determined from the optical properties of the incident beam and the aerosol.[11, 51] If the particles are separated by a distance large compared to their average radius, scattered intensities from more than one particle will be additive since there will be no permanent phase relationship between the radiation scattered by two different particles. For monodisperse aerosol, computational methods[11,50,51] are available for calculating angular Mie scattering functions $(i_1 + i_2)$, when the incident beam is unpolarized and incoherent. However, no significant difference has been observed in scattering intensities when an incoherent beam is replaced by a He-Ne laser beam.[41] Scattering characteristics of atmospheric aerosol with an incident laser beam has been reported by Call et al.[7] for different values of scattering angle θ.

For polydisperse aerosol, an approximation can be made

$$i_1 = i_2$$

and equation (45) can be rewritten as

$$I(\theta) = \frac{\lambda_o^2 I_o N_p \Delta\Omega}{4\pi^2} i_1 (\alpha_p, m, \theta) \qquad (46)$$

where $\Delta\Omega$ is the solid angle subtended by the receiving aperture, I_o is the power density of the incident beam at the scattering zone, and N_p is the number of particles within the sensing volume. The intensity functions i_1 and i_2 can be found for a wide range of α_p, m, and θ, given in the NBS table of scattering functions for spherical particles.[51]

To gain a physical insight of the effect of the aerosol parameters, Mie theory can be further simplified[21, 39] for approximate calculation. The normalized angular scattering intensity coefficient $I(\theta)$, defined by the ratio of flux scattered per unit solid angle at an angle θ from the forward direction to the flux geometrically incident on the particle, can be expressed as

$$I(\theta) = K n r_p^z$$

where K is a constant, r_p is the average particle radius, n is the aerosol number concentration per cc, and z depends on the angle θ, aerosol size parameter α_p and the refractive index of the particle. The value of z is empirically determined. For polydisperse aerosol in a size range that can be used for turbulence measurement, it is expected that z would vary widely with the radius r_p, probably within the range of values of 2 to 4. Since the size distribution of aerosol generally follows a skewed Gaussian curve, it is of interest to examine whether the aerosol radius corresponding to the maximum number concentration has the highest value of z. For polydisperse aerosol, it appears that

only the higher size fractions will contribute significantly to the total scattering intensity if z is approximately the same aerosol size spectrum present in the fluid medium. This would effectively reduce the adverse effect of using heterogeneous aerosol with the associated spectrum of stop-distance values in turbulence characterization. Where such assumptions are not valid, contributions from different size ranges may be equally significant to the total scattering intensity. Aerosol size distribution, in this case, should be narrow.

An estimation of the order of magnitude of the forward scattering intensity at a distance R from the scattering volume, containing N_p particles of radius r_p, can be made from the following equation.

$$I(\theta \approx 0^{\circ}) = \frac{\pi^2 r_p^4 K_s^2 N_p}{4R^2 \lambda_o^2} \cdot I_o \cdot \qquad (47a)$$

I_o is the intensity of the incident beam and K_s is the scattering coefficient, which is a function of the refractive index m and the size parameter α_p of the aerosol. For water mist particles with radii in a size range of 0.5 micron to 1 micron, K_s has an approximate value of 2 for λ_o = 6328 A. For θ in the range of 1 to 2°, r_p = 0.5 micron, K_s = 2, R = 50 cm, λ_o = 6328 Å, and an incident laser beam power of 30 mW focused to an airy disk diameter of 100 microns, the scattered intensity per particle is

$$I(\theta \approx 0^{\circ}) \approx 2.4 \times 10^{-4} \text{ watts/particle} \cdot$$

If $\theta = 30^{\circ}$, $I(\theta)$ is expected to be reduced by about three orders of magnitude. The expected scattering intensity will be

$$I(30^{o}) \simeq 2.4 \times 10^{-7} \text{ watts/particle} . \qquad (47b)$$

Equation (47) shows that scattering intensity varies as the fourth power to the radius r_p, which indicates that only the larger size fractions of aerosol are of primary importance in scattering intensity. The assumption that the scattered intensity is N_p times that scattered by a single particle is valid for a dilute aerosol. In general, a large particulate concentration and a small scattering angle are desirable for a high scattering intensity. The last requirement cannot be met easily since it is contrary to the other criteria discussed previously.

3. Aerosol concentration

Particulate concentration should be sufficiently high for a high SNR and a low δf_T. However, energy removed from the incident and the scattered beam will also increase in direct proportion to the value of n. Further, a large aerosol concentration would effectively produce more heterogeneous aerosol due to a higher coagulation rate. Aerosol coagulation is a spontaneous process and its rate is proportional to the square of the concentration.

$$\frac{dn}{dt} = - \frac{K_o}{2} n^2 \qquad (48)$$

where n is the number of particles per unit volume (instantaneous concentration) and K_o is the rate constant for still air. The rate constant increases appreciably with turbulence. Thus, a fairly monodisperse aerosol will become polydisperse in a short residence time due to coagulation if n is large.

4. Generation of aerosol:

The type of aerosol to be used for scattering purposes would depend on the physical properties of the fluid medium and on the flow system. The generation of a fairly monodisperse aerosol by dispersion of powders is quite difficult for the size range of present interest. One of the commonly used devices for generation of solid aerosol is the Wright dust feed mechanism[21] which uses dry compressed air for dispersion. Well-fractionated solid powders can be used. If the generator is followed by an ilutriator, a suitable size range can be picked up for scattering aerosol. Aerosol generation by an atomizer nozzle of a modified Laskin[33, 38] type can be used for generating liquid droplets in a size range of 0.2 to 3 microns diameter. Fairly uniform submicron aerosol (0.3 to 0.8 micron mass median diameter) of dioctyl-phthalate can be generated using this generator. The aerosol output rate can be varied widely by controlling the number of the atomizer nozzles and the applied pressure. Use of dioctyl-phthalate or water droplets is advantageous because of minimum cleaning and corrosion problems in optical windows and in wind tunnel equipment. Smoke or metal oxide fumes can be used but are not very desirable because of their corrosive properties and difficulties in continuous generation. Submicron solid aerosol can be generated by atomizing an aqueous solution of uranine (disodium salt of flourescein) in a nebulizer and subsequent drying of the aerosol. Similar methods are available for generating sodium chloride and stearic acid aerosols. The generated aerosol preferably should be non-toxic and have a low electrostatic charge.

E. Laser Output Power and Wavelength

The previous discussions on the scattering characteristics indicate that the power of the incident laser beam (P_o) should be high and the wavelength (λ_o) of radiation should be small. Intensity of the scattered beam is directly proportional to that of the incident beam and inversely proportional to the square of the wavelength. Further, the quantum efficiency of the photomultiplier increases considerably with the decrease of wavelength in the region of 7000 to 4000 A. For instance, an RCA 7265 photomultiplier having S-20 response has a quantum efficiency of approximately 5.9 percent at 6328 A which increases to 11 percent if the green wavelength of a cw argon laser is used. The quantum efficiency of a RCA 4526 is typically double that available from the S-20 PM tubes in this wavelength regions.

The use of a cw argon ion laser has the advantage of: (1) high power handling capacity; (2) higher scattering coefficient; and (3) higher quantum efficiency of the detector. However, compared to a cw He-Ne laser, an argon laser has appreciably more noise in the low frequency spectrum of the Doppler frequency shift. The signal-to-noise ratio is limited by this noise which arises primarily from the plasma and mode instabilities of the argon laser. However, single frequency operation under optimum conditions would increase the SNR considerably.[25]

F. Coherence Loss and Random Phase Scattering

The optical path of the incident beams and the scattered beam in a turbulent medium would give rise to a loss of coherence due to the inhomogeneities of the refractive index. Further, there is a loss of

coherence in the scattering process. The density fluctuations of the fluid medium affect the geometry of the focal spot. The aerosol particles cross the sensing volume in a random fashion. The emanated signal consists of a wave train of random phase. These factors cause appreciable decrease of signal-to-noise ratio.

G. Effect of Path Difference

For a maximum possible heterodyning efficiency, the path length difference ΔL between the two incident beams should be zero. Deviation from this will cause loss in the heterodyning efficiency depending on the coherence length of the laser. It has been experimentally observed[2] that the heterodyning efficiency varies with the path length difference as shown in Figure 20. The path length difference ΔL can be made equal to $2nL$ without appreciable loss of heterodyning efficiency. Thus, in general

$$2nL - C_1 < \Delta L < 2nL + C_1$$

where C_1 is the coherence length of the laser, L is its cavity length, and n is an integer; $n = 0, 1, 2, 3, \cdots$.

H. Frequency-to-Voltage Conversion of the Doppler Signal in Turbulence Characterization

1. Frequency demodulation:

The application of a laser Doppler velocity meter in the characterization of a turbulent flow field requires recording of the temporal fluctuation of frequency of the Doppler signal. The range of the frequency deviations from the mean value and the rate of change of

frequency depend directly on the velocity fluctuations of an element of fluid at the point of observation. Analog conversion of the Doppler frequency shift to voltage is desirable for discerning the statistical properties of the flow field. The resulting voltage variations proportional to the instantaneous velocity can be conveniently analyzed by analog or digital methods. Although the approach is straightforward, its use is greatly limited because of the lack of a simple and convenient analog conversion method that can process the Doppler signal.

In general, three analog conversion methods appear feasible: (1) the use of ratio detectors or pulse counting type frequency discriminators with a large bandwidth; (2) phase-locked loop demodulators; and (3) envelope detection and frequency tracking by FM feedback demodulation. It is desirable that the conversion device be simple, easy to operate and economic so as to make the laser Doppler technique an efficient and attractive tool for turbulent studies both in the subsonic and supersonic regions.

Conventional ratio detectors used in FM demodulations do not have a frequency range sufficiently wide to encompass Doppler signal excursions in the frequency domain. A Q-spoiled ratio detector with a wide deviation range can be used if the signal-to-noise ratio is high and the turbulent intensity is low. Under these conditions and if the instrumental frequency spread is low, a pulse counting type of frequency discriminator can be used. A cross-correlation technique of noise elimination and frequency conversion, as used in the correlation-Doppler radar system, although feasible, is not readily applicable to the

present problem because of the higher modulation frequency involved. Unless suitable signal conditioning is performed, the above methods are not satisfactory in turbulence characterization. The primary disadvantage comes from the fact that the Doppler signal has a finite instantaneous frequency spread and a large modulation index. This requires a high level of SNR as discussed below.

2. SNR and bandwidth consideration:

As mentioned earlier, the FM signal from a turbulent flow field will have a varying modulation index. Since the average value of β would be large ($\beta >> 1$) the bandwidth approaches $2\Delta f$, where Δf is the frequency deviation corresponding to the velocity fluctuation. In general, this frequency deviation will be large, since

$$\frac{\Delta f}{f_c} = \frac{\Delta U}{U} \quad . \tag{49}$$

Such a wide bandwidth is advantageous to a FM system provided the SNR of the carrier (S_c/N_c) is high. The SNR value is quite critical since the noise output to the receiver increases in direct proportion to its detection bandwidth. In the present case the effective bandwidth is large, but S_c/N_c is limited by the instrumental frequency spread of the Doppler signal. Unless the carrier signal-to-noise ratio is above a threshold value[44,45], demodulation becomes extremely noisy. For example, if $\beta = 4$, the critical value of the signal-to-noise ratio is 15 dB. In an FM receiver the output signal-to-noise ratio falls off rapidly if the strength of the input signal is below a threshold level. When these threshold conditions are met, there is a considerable improvement of the signal-to-noise ratio of the demodulated output

with respect to the input SNR. The Doppler signal from a turbulent flow field should have a SNR above the threshold value. The threshold value in the present case is a function of the modulation index and the instrumental frequency broadening (δf). A probable range of this threshold value is 13 to 20 dB.

It is imperative that all the system parameters be optimized to obtain a maximum possible value of SNR. However, because of the signal generation process involved in a particular application of the laser Doppler method, the maximum value of SNR obtainable may be lower than the threshold limit. To lower the threshold level it is necessary to lower the bandwidth and the noise figure of the demodulator. Since the latter is generally fixed, reduction of the bandwidth offers a solution. It is evident that distortion will result if the receiver bandwidth is smaller than the effective bandwidth of the signal. However, if the demodulator has a narrow instantaneous bandwidth but is capable of tracking the signal frequency over a wide range, threshold reduction is possible.

Two techniques are available for bandwidth reduction or threshold extension: (1) phase-locked loop detection; and (2) envelope detection and frequency tracking by FM feedback demodulation. The second system, which is rather a logical improvement of the first method, is efficient but more complex. In the present studies, a phase-locked loop detector has been used.

The FM demodulation process accentuates the high frequency noise components. It is therefore preferable to pass the Doppler signal through a high pass filter for preemphasis of the higher frequency

signal components. A high pass filter will also eliminate the Doppler spectrum around "zero" frequency (Appendix I). A low pass filter, with a cutoff frequency higher than the maximum frequency of signal excursion, will minimize high frequency noise. Thus, a bandpass filter is desirable for signal processing before the signal is applied to the demodulator stage.

3. Phase-locked loop:

A block diagram of the phase-locked loop is shown in Figure 21. The loop consists of a phase comparator, a low pass filter, a dc amplifier and a voltage controlled oscillator. The basic operation of the loop has been well described in the literature.[18,34] The FM signal is applied to the phase comparator. The phase comparator output is proportional to the cosine of the error phase angle. Basically, the phase comparator performs the integration (1/S) for converting frequency difference to phase difference. If the input is represented as $E_i \sin(\omega_c t + \phi_i(t))$ and the voltage controlled oscillator (VCO) output as $E_o \cos(\omega_c t + \phi_o(t))$ then the output of the phase comparator is

$$v_c = K_1 \cos\left[\phi_i(t) - \phi_o(t)\right]$$

where K_1 is the sensitivity of the phase comparator. This output is passed through a low pass filter (F(S)) which rejects the high frequency error components and enhances the interference rejection. The output voltage of the low pass filter can be represented by an error voltage e(t), where

$$e(t) = h(t) * K_1 \cos\left[\phi_i(t) - \phi_o(t)\right] \quad .$$

Equation (50) represents a convolution of the impulse response h(t) of the filter and the output of the phase comparator. Assuming the VCO output frequency ω_o is a linear function of the error voltage input,

$$\omega_o = \omega_c + \mu K_2 \, e(t) \tag{50}$$

where K_2 is the sensitivity of the VCO in radians/sec/volt and μ is the gain of the amplifier. It is assumed that the center frequency ω_c of the incoming signal is within the locking range of the loop.

The integration process (1/S) in the phase comparator results in a zero steady state error between the frequencies of the input signal and the VCO output. When the VCO output frequency is equal to the input signal frequency, the system is said to be locked. The maximum frequency deviation of the input for which the system still remains locked is known as the lock range. The capture range is defined as the range of input frequency to which the VCO can be synchronized automatically, when initially in the unlocked state. The capture range cannot be larger than the lock range, but can be smaller. The two ranges coincide when the low pass filter allows all of the low frequency components to pass unattenuated but rejects the high frequency components of the phase comparator output.

In the case of the Doppler signal from the turbulent flow field, since occasional signal dropouts are expected, both the locking range and the capture range should be high. Therefore, a higher cutoff frequency of the low pass filter is desired. This, however, increases the instantaneous bandwidth of the receiver and, thus, is less effective in decreasing the threshold level. A compromise is therefore necessary.

The concept of phase-locked loop for FM demodulation has been known since the early 1930's. However, the construction of a phase-locked loop with a wide frequency range was difficult because of the complexity involved in making this device from discrete circuit components. However, many of these practical difficulties have been removed by the recent availability of the phase-locked loop device as a single integrated circuit capable of wide range frequency demodulation.

When the signal-to-noise ratio of the Doppler signal is low, a larger amount of threshold extension may be required. In such a case, FM feedback technique for threshold extension will be required. Practical extension limits are a function of frequency deviation, modulation frequency, filter bandwidth and the feedback process.

IV. EXPERIMENTS, RESULTS AND DISCUSSION

A. Symmetrical Heterodyning System

Three types of scattering processes were studied in the present investigation: (1) surface scattering; (2) solid volume scattering; and (3) fluid medium (air) with scattering aerosol. In this section, experiments primarily on the development of the heterodyning process, frequency-to-voltage conversion method, and system optimization are described. The application of the laser Doppler velocity meter to the characterization of turbulence is described later. A list of major components and equipment used in these studies is given in Appendix II.

Two experimental setups, shown in Figures 5 and 7, were used to study the relative merits of the symmetrical heterodyning system compared to the local oscillator process. In both of these experiments, a one-dimensional velocity measuring system using back scattered light from a rotating disk was used. A Spectra Physics, Model 125 He-Ne laser with rated output of 50 mW and wavelength of 6328 A was used. The detector used was a RCA 4526 photomultiplier, which had a dark current of 2 nA at room temperature. A 50 ohm load resistor was used and the output of the PM tube was fed to a Singer Metrics spectrum analyzer through a wide band amplifier. The amplifier used was a C-COR amplifier having a 200 MHz bandwidth. The disk was painted with fairly uniform 20 micron diameter white pigment particles and was driven by a synchronous motor. The velocity of the scattering point could be adjusted from 10 to 30 meters per second.

The frequency spread in both heterodyning systems was measured for constant velocity of the scatterer. Measurements were made at the half power points using the spectrum analyzer display. SNR measurements were also made using the spectrum analyzer. Experimental data on instrumental spectral broadening are plotted in Figure 22 for the two systems. The frequency spread of the Doppler signal in the symmetrical heterodyning system did not increase with the size of the receiving aperture. In the case of local oscillator heterodyning, the frequency spread increased with the aperture diameter. These results were in accordance with the theoretical expectations.

The major contribution to the signal spread in a symmetrical system comes from the transmission aperture. Figure 23 shows the variation of δf_a with the transmission aperture diameter. The local oscillator heterodyning system will show a similar variation except that the minimum value of the spread will be higher due to the large value of $\delta f_{\Delta\Omega}$. The aperture diameter used in the transmission beam was maintained at 4 mm in both systems during all other experiments.

The signal-to-noise ratios are plotted in Figure 24 for the two systems as a function of signal strength, P_s. All other parameters, such as α and $\Delta\Omega$, were kept constant. In the local oscillator heterodyning system, the reference beam intensity was adjusted each time to maximize the signal-to-noise ratio. In this experiment, the receiving aperture diameter was maintained small. As expected, the maximum value of SNR in both systems is approximately the same. The symmetrical system always gave higher SNR values due to a low δf_a and a better

heterodyning efficiency. The maximum value of signal-to-noise ratio that could be obtained using the surface scatterer was approximately 45 dB in the symmetrical system. Some typical values of SNR and instrumental frequency spread are given in Table I. For a comparative study, the heterodyning system developed by Bond[5] was also employed for SNR measurements. Figure 6 shows an experimental arrangement where two scattered beams are used. In all heterodyning systems, SNR and δf depend on the system parameters used. If the intensity of the scattered beam at the receiving aperture is large, a small aperture can be used and all three systems give comparable values of SNR and δf.

The symmetrical system would be preferred if the scattered intensity is low, but the signal may be increased by employing large values of $\Delta\Omega$, since δf_a will be appreciably smaller as compared to the other two cases. The symmetrical system also possesses less critical optical alignment procedures. In the case where the distance between the scattering centers and the receiver is large and the intensity of the scattered beam is low, a reasonably large receiver aperture area will not make a large $\Delta\Omega$ and, consequently, δf_a will not be significant. Here, the local oscillator process would be a preferred choice for heterodyning.

Since it is desired that in a laser Doppler system SNR should be high and δf should be low, it is possible to define a dimensionless quantity Q_s relating these two parameters. Designating this as the "figure of merit" of the heterodyning system, the following expression may be written:

$$Q_s = \text{SNR(power ratio)}/(\delta f/f_c)$$

TABLE I

Typical Values of SNR and $\delta f/f_c$ for the Three Different Heterodyning Systems

System Used	$\delta f/f_c$ *		SNR	
	$\sin \alpha/2 = 0.0075$ $\sin \theta/2 = 0.075$	$\sin \alpha/2 = 0.0028$ $\sin \theta/2 = 0.15$	$P_s = 10^{-8}$ Watts	$P_s = 10^{-7}$ Watts
Local Oscillator Heterodyning	20.0%	20.0%	17 dB	29 dB
Two Scattered Beam Symmetrical System	3.1%	0.8%	12 dB	33 dB
Two Incident Beam Symmetrical System	3.8%	0.8%	31 dB	33 dB

* $\Delta\Omega = \pi/8600$ sterradians; $D_A = 8.5$ mm

Note: For large values of $\Delta\Omega$, the two scattered beam system will have larger values of $\delta f_a/f_c$ compared to the two incident beam system.

which is evaluated at a scattered beam intensity of s watts per cm^2 per second at a unit distance from the scattering center and in the direction of the receiving aperture. For a comparative study between the heterodyning systems, measurements of Q_s were made on the equal intensity scattered lobe, i.e., constant s, since SNR depends on the total signal power falling on the photocathode. Figure 25 shows a plot of Q_s versus P_s for the two heterodyning systems. This plot clearly shows that, as long as P_s can be increased by increasing the receiving aperture so that P_s is greater than 1×10^{-10} watt, the symmetrical system will be more advantageous. Below this level, the local oscillator heterodyning system may give better SNR values. The value of Q_s decreases in the local oscillator heterodyning system as the scattering intensity decreases, whereas in the symmetrical heterodyning system, Q_s does not change with the scattering intensity (for constant P_s) since in the latter case SNR and δf_a are not affected by the size of the receiving aperture.

B. Measurement of the Instrumental Spread Due to the Finite Sampling Volume

To examine the relative magnitude of the instrumental spread, δf_s, arising from the finite sensing volume compared to the aperture broadening δf_a, experiments with known values of spatial velocity gradients were carried out. Two scattering systems were chosen. In one system, a rotating surface scattering disk was used, where there is a velocity gradient along the radial direction from the center of the disk. When the two incident beams are focused on the scattering disk such that the

bisector of the angle θ is normal to the disk surface, the velocity gradient is along the blur diameter D_B of the focal spot of the beam (Figure 26). The experimental arrangement was the same as shown in Figure 7. If the point of velocity measurement is at a distance r from the center of the surface scattering disk, the center frequency f_c corresponds to the velocity ωr, where ω is the angular velocity of the disk. If the characteristic diameter of the sensing volume is d ($d = D_B$), the expected frequency spread δf_{sd} will be, from equation (33a),

$$\frac{\delta f_{sd}}{f_c} = \frac{d}{r} = \frac{2.44\ \lambda_o}{2r \sin \frac{\alpha}{2}}$$

which is independent of the angular speed of the motor shaft.

The second experiment was carried out to measure the frequency spread arising from the effective length ℓ of the laser beam "probe". A volume scatterer was used in the experimental arrangement shown in Figure 27. The disk was made of clear transparent silicone compound (GE RTV-615 Silicone Potting Compound with one percent curing agent) to which white pigment particles were added to act as scattering centers within the solid volume scatterer. The disk was rotated about a vertical axis and the two incident beams were focused inside the volume scatterer. The velocity gradient existed only along the length ℓ of the sensing volume. The expected frequency spread can be written from equation (33b),

$$\frac{\delta f_{s\ell}}{f_c} = \frac{\ell}{r} = \frac{2.44\ \lambda_o}{2r \sin \frac{\alpha}{2} \sin \frac{\theta}{2}}$$

where r is the radial distance measured from the axis of rotation to the point of measurement.

Table II presents the total frequency spread measured in each case. In this set of experiments δf_a remained the same. The primary objective was to determine whether or not the total instrumental spectral broadening is effectively determined by one of its components which has the largest magnitude. The effective frequency spread is not expected to be the algebraic sum of the components of each different spread, such as δf_a, δf_s and δf_T. However, it was neither possible to devise an experiment where the instrumental frequency spread would come from a single source, while the other sources contribute no frequency spread, nor was it possible to measure the individual components of the effective frequency spread while contribution came from more than one source.

The experimental results show that the effective spread was determined by the aperture broadening which had the largest magnitude in the present case. A slight increase of frequency spread in the case of the volume scatterer was probably caused by the fluctuation of the angular speed of the motor shaft. The volume scatterer was driven by a low speed air-driven motor and a high speed synchronous motor was used with the surface scattering disk.

Figure 28 shows the intensity versus distance plot as the rotating silicone rubber disk was moved along the optical axis in the region of the focal point. Maximum intensity was reached when the beam was focused at the edge of the disk (air-silicone rubber interface). This interface corresponds to the $\Delta x = 0$ point. When the disk was moved

TABLE II

Effect of Different Sources of Doppler Signal Broadening (Instrumental) on the Effective Frequency Spread δf

Scattering System	f_c	δf_a*	δf_{sd}*	$\delta f_{s\ell}$*	δf Measured
Surface Scatterer	5.6 MHz	303 kHz	9.6 kHz	≈ 0	230 kHz
Volume Scatterer	5.6 MHz	303 kHz	≈ 0.0	128 kHz	270 kHz

*Calculated values. All frequency spread are referred to half-power points

$\theta/2 = 4.3^{\circ}$; $\alpha/2 = 0.28^{\circ}$; $d \approx 154\ \mu$; $\ell \approx 2.03$ mm

away from this point, the intensity declined as shown in the right half of the plot (Δx positive). The rate of fall of intensity was not very sharp because of the fact that the outer surface of the disk was not perfectly spherical and concentric. In this case the scattering particles were moving out of the sensing volume. When the disk was moved toward the transmission optics (Δx negative) the sensing volume moved inside the silicone rubber disk. The intensity declined again because of the absorption of light in the scattering medium.

C. Velocity Measurement Without Directional Ambiguity

The experimental arrangement used to measure velocity without the directional ambiguity of 180° is shown in Figure 8. The output beam from a 50 mW He-Ne laser is incident upon a reflection grating mounted along the edge of a large diameter lucite disk. The disk was rotated at a constant angular speed which was adjustable. The two first orders of the diffracted beams were used as the two incident beams of the symmetrical heterodyning system. The two beams were focused at the point "0" on the front surface of the surface scattering disk. The motor and the disk assembly was movable in a vertical plane so that the point "0" moved in a vertical line on the surface scatterer. The velocity of the scattering particles at the point "0" can be changed in magnitude and in sign, with reference to a given x-direction, by shifting the point of measurement above or below the horizontal line passing through the center of the disk.

When the surface scattering disk is stationary ($U = 0$) and the two incident beams have different frequencies, a Doppler signal of

frequency f_o is generated. As the angular speed of the rotating diffraction grating was increased, f_o was found to increase as expected from the theory. The speed was adjusted so that the frequency bias f_o = 6.0 MHz. The angle β between the first order and the zero order was measured and it was found to be 19.31^o.

The surface scattering disk was then rotated at a constant angular speed. As the point of measurement "0" was moved along a vertical line on the surface of the scattering disk, the Doppler signal frequency was shifting above or below f_o depending on the direction of the linear velocity U. In Figure 29, the observed frequency shifts were plotted along with the theoretically expected curve. An excellent agreement between these shows that the method is readily applicable to any system where the velocity may change its direction.

Similar frequency biasing was also obtained by using an encoder disk with its outermost track having a spatial frequency of 100 lines per mm. The disk was mounted on a movable shaft which was driven by an air motor. A photograph of this device is shown in Figure 30. The diameter of the outer track of the encoder disk was 9 inches. The rotating encoder disk system was found to be an efficient method for a continuous variation of the frequency bias f_o in a low frequency range without any appreciable vibration problem.

In general, this technique is applicable to any system where the direction of velocity is unknown. The present work is primarily aimed at measuring two-point cross correlation of velocity in turbulent flow fields. The velocity component along the channel axis has a non-zero average component while the velocity components along the other two

orthogonal coordinates have fluctuations in velocity about the zero dc component. If the positive and negative directions are not resolved, the velocity versus time plot will be folded about the zero velocity axis. This method also can be used with advantage where a frequency translation is desirable in the Doppler frequency shift measurement.

D. System Optimization

Experiments on the minimization of the instrumental spectral broadening and the improvement of the signal-to-noise ratio were performed. Both surface scattering experiments and the fluid flow studies were employed in this investigation. The effect of the system parameters, such as α and θ as well as the size and concentration of aerosol to be used, were studied. A spatial filter was designed and incorporated in the system for minimization of background radiation.

1. Measurement of small instrumental broadening:

The experimental setup used to obtain a minimum possible value of δf and a maximum SNR is shown in Figure 31. The angle θ was varied by changing the spatial orientation of the incident beams. The value of α was varied by using lenses of different focal length for L_1. When the instrumental frequency spread was below 50 kHz, the spectrum analyzer could not be used for an accurate measurement of the frequency spread δf, because of the spectrum analyzer low resolution limit ($\simeq$ 50 kHz). A communication receiver, Hallicrafter Model S76, was used for frequency bandwidth measurement with a high resolution. The instrument has a high sensitivity and an operating range from 538 kHz to 34 MHz. Selectivity of 500 Hz or better was obtainable. For the

calibration of its bandspread dial at any frequency range of measurement, a precision, crystal controlled beat frequency signal generator (Philco Corporation, Signal Corps Frequency Meter BC-221-E) was used. The carrier level meter of the communication receiver was calibrated with an RF signal generator from which RF signals of known amplitude were applied to the receiver and the receiver output meter reading was noted.

The accuracy of bandwidth measurement was greatly improved by the use of this communication receiver compared to the spectrum analyzer measurements. For example, the two spectrum analyzer displays in Figure 32 show the Doppler signal spectrum and an RF signal from an oscillator. The center frequency in both cases was maintained nearly equal. The analyzer sweep width was the same in both displays. Although the bandwidth of the Doppler signal is appreciably larger than the oscillator output, measurements of the width of the Doppler signal are quite difficult due to the resolution limit of the spectrum analyzer. When the same two inputs were analyzed by the communication receiver, the expected large difference in their frequency spectra was observed. Frequency spectra for the two signals are shown in Figure 33. A communication receiver also can be used with advantage for measuring the frequency bandwidth of the Doppler signal arising from the velocity fluctuations in the fluid flow.

Measured values of δf agreed well with the theoretically expected values of δf_a (transmission aperture broadening) as long as δf_a was greater than the magnitude of the other instrumental frequency spreads,

δf_s (instrumental frequency spread arising from spatial velocity gradient) and δf_T (instrumental frequency spread arising from finite signal lifetime). Since both δf_s and δf_T were present in the system, the measured lower limit of the instrumental broadening was set by the above two sources when δf_a was minimized. Some typical values of the measured frequency spread, δf, are given in Table III along with the theoretically expected values of the aperture broadening. In general, the measured values of the frequency spread were lower than the computed values. This discrepancy can be explained by the fact that theoretical calculations were based on the assumption that the laser beam intensity distribution across the transmission aperture is constant.

To examine the effect of time-discontinuous signal on the Doppler spectrum measurement by the communication receiver, a slotted surface scattering disk was used to generate a Doppler signal. The experimental arrangement is shown in Figure 34 and the measured frequency spectrum is shown in Figure 35.

2. Spatial filtering:

To prevent background scattered light from falling on the photocathode, a spatial filter was used, as shown in Figure 15. For determining its spatial resolution, a translucent scattering sheet, 175 microns thick, was positioned and moved in the effective scattering zone along and perpendicular to the receiving optical axis. The relative intensity of light falling on the photomultiplier was plotted against the displacement ($\Delta\ell$) in mm of the translucent surface from the center of the sensing volume. Two simple lenses were used in this spatial filter along with a

TABLE III

Effect of System Parameters on Instrumental Frequency Spread*

sin $\alpha/2$	sin $\theta/2$	$\delta f/f_c$ x 100% Calculated	$\delta f/f_c$ x 100% Observed	SNR dB
0.0028	0.1500	1.82	0.8	30
0.0040	0.5736	0.57	0.5	30
0.0075	0.0750	4.90	3.8	31
0.0143	0.2436	5.72	1.4	30
0.0143	0.1398	10.13	4.3	28

*Referred to half-power points

pinhole. Figure 36 shows the dependence of the optical spatial filtering efficiency on the incident beam geometry (θ and α).

The relative intensity versus distance plot shows the resolution along the receiving optical axis or the depth of longitudinal focal tolerance (ℓ). Figure 37 shows the improvement of the resolution when the receiving optical axis is tilted by an angle of 30° in the vertical plane. Obviously, this improved resolution was gained with the sacrifice of the scattering intensity. Figure 38 shows the spatial resolution in the direction perpendicular to the optical axis and in the focal plane. This plot gives a measure of d, the characteristic diameter of the sensing volume (Figure 15). As expected, the transverse focal tolerance (d) is smaller than the longitudinal tolerance (ℓ). Better spatial filtering will be obtained if diffraction limited optics are used. It appears that the use of corrected optical components, to obtain better spatial resolution and a high SNR, is desirable in the characterization of the structure of turbulent fluid flow.

E. Aerosol Generation and Measurement of the Scattering Intensity as a Function of Scattering Angle

1. Aerosol generation:

Three types of aerosol were used in the fluid flow studies: (1) talcum powder dispersed by a Wright dust feed mechanism; (2) water mist produced by injecting steam at the upstream end of a duct through which air at room temperature was drawn by a blower connected at the end of the duct; and (3) dioctyl-phthalate (DOP) aerosol generated by an atomizer nozzle assembly. The dioctyl-phthalate aerosol generator was found to be most satisfactory for continuous operation and in producing sub-micron aerosol. The generator was made according to the design of Parrish and Schneider.[38] A photograph

of the DOP aerosol generator and a schematic diagram of one of its nozzles are shown in Figure 39a and 39b respectively. From the design consideration of this generator, it is expected that the particle size will have a mass median diameter of approximately 0.8 micron.[38]

2. Measurement of scattering intensity:

A wide angle optical spectrum analyzer[46] was used to measure the scattering intensity as a function of the scattering angle. The experimental arrangement is shown in Figure 40. DOP aerosol was used for the scattering measurement. The relative scattering intensity is plotted against the scattering angle θ in Figure 41. It may be noted here that a 30° scattering angle corresponds to an angle of 60° between the two incident beams used in the symmetrical heterodyning system.

F. Frequency-To-Voltage Conversion

In the process of developing a suitable frequency-to-voltage conversion device, three types of FM demodulators were studied: (1) ratio detector, (2) frequency meter discriminator and (3) phase-locked loop detector.

1. Ratio detector:

A ratio detector was made with its effective bandwidth widened by using a Q-spoiling load resistor. Its effective bandwidth was approximately 700 kHz with the center frequency around 13 MHz. The characteristic curve of this ratio detector is shown in Figure 41. A mixer was used to translate the Doppler signal spectrum to the frequency range of operation of the ratio detector. It was observed that, if the signal-to-noise ratio is 20 dB or higher and the instrumental frequency spread is

below 50 kHz, such a ratio detector can be used for turbulent intensity measurement. In general, the performance of the ratio detector in Doppler signal processing was not satisfactory. This was expected since signal-to-noise ratio of the Doppler signal was below the threshold level.

2. Frequency meter discriminator:

A Hewlett-Packard frequency meter discriminator was used for Doppler signal demodulation. The instrument has a linear dynamic range from several hertz to 10 MHz and is capable of wide deviation range FM demodulation. The instrument can be used to read the frequency input (f_c) and its output can be fed through a low pass filter to give the demodulated signal. The experimental arrangement is shown in Figure 43. The instrument operation was found satisfactory when tested with a simulated signal which was a time-discontinuous frequency modulated rf output but without any instrumental spread. In the case of Doppler signal demodulation, the demodulated output was extremely noisy, which was apparently caused by the characteristic instantaneous frequency broadening of the Doppler signal. The Doppler signal was passed through a band pass filter having a pass band wide enough to pass the Doppler signal spectrum. Table IV shows several typical readings of the frequency meter along with the center frequency reading of the Doppler signal measured by the spectrum analyzer. It was observed that when the instrumental frequency spread was high the frequency meter reading lagged the true frequency reading. This lag was expected since the Schmitt trigger circuit at the input of the frequency meter was disabled by the presence of a large instrumental frequency broadening. The above experiment was performed using laminar fluid flow and rotating surface scattering disk.

TABLE IV

Effect of the Instrumental Frequency Spread of the Doppler Signal on Frequency Meter Operation

Spectrum analyzer reading fc	SNR dB	$\frac{\delta f}{fc}$ x 100%	Frequency meter reading	System used*
3.5 MHz	30	1.0	3.5 MHz	(1)
2.5 MHz	30	1.0	2.5 MHz	(1)
750 KHz	15	1.0	750 KHz	(2)
250 KHz	15	1.0	250 KHz	(2)
5.0 MHz	20	8.3	4.1 MHz	(1)
4.0 MHz	20	8.3	3.5 MHz	(1)
2.5 MHz	20	8.3	2.3 MHz	(1)

*(1) Surface scattering disk
(2) Laminar air flow

To observe the performance of this frequency meter in an oscillating flow field of known frequency, a flow modulator, schematically shown in Figure 44, was constructed. The bleed port of the flow modulator faces a slowly rotating aluminum disk which has different sized openings. The flow output from the nozzle can be modulated at a known low frequency. The flow can be maintained within the laminar flow regions if the Reynolds number is small. The flow field was observed by studying the schlieren image. A schlieren photograph of the laminar oscillatory jet is shown in Figure 45. Figure 46 shows a record of the demodulated output of the frequency meter plotted against time for steady and oscillatory flows. However, when a Doppler signal from a turbulent flow field was applied, the modulated signal was noisy and, in general, was not satisfactory. This was expected from the fact that the input SNR was below the threshold value and the instrumental frequency spread was considerably higher than the value that could be used in such a system for frequency demodulation.

An AGC amplifier was built for reducing the adverse effect on FM detection due to the amplitude fluctuation of the signal. The schematic circuit diagram is shown in Figure 47. Automatic gain control was effective when the frequency of amplitude fluctuation was low and the frequency spread (δf_T) due to signal dropouts was negligible.

3. Phase-locked loop detector:

Two phase locked loop detectors were made using Signetics NE 561B PLL integrated circuits. A schematic diagram of one of the detectors is shown in Figure 48. The demodulated output is fed to an active low pass filter to reject the high frequency noise arising from occasional

signal dropouts. The output of the filter can be directly recorded by a magnetic tape recorder for later processing of the signal or connected directly to an analog correlator. A Sony Model TC-355 audio tape recorder was used. The frequency response of the tape recorder is flat from 20 Hz to 22 kHz at 7.5 inches per second tape speed. The high frequency response was adequate compared to the maximum turbulence frequency expected in subsonic air flow fields. At low Reynolds numbers, when the frequency of turbulence has components below 20 Hz, the signal could not be recorded on a magnetic tape without attenuation. To obviate this difficulty, an AM modulator was incorporated in the FM detection unit. A 15 kHz signal from an audio oscillator was modulated by the low frequency turbulence signal which could be recorded on magnetic tape using the audio tape recorder. An AM demodulator was used to retrieve the signal for further processing.

Figures 49 and 50 show an interior view and the external controls of the phase-locked loop detector, respectively. The demodulator was calibrated using a FM generator which could be operated at different carrier frequencies and with a modulation frequency which was adjustable within the audio frequency range. Since the present work is primarily on low frequency turbulence, R_1C_1 values used in the filter of the phase-locked loop demodulator were selected for low modulation frequency. It was found that the demodulator output was linearly related to the amplitude of the modulating signal in the frequency range 0 to 6 kHz. Figure 51 is a calibration curve showing the relationship between the amplitude of the input sinusoidal modulation with the

output voltage variation. The circuit also was tested with a Doppler signal from low frequency turbulence. Since a fully developed turbulent flow at a high Reynolds number could not be generated in the present wind tunnel, the demodulator circuit could not be tested at a high turbulence frequency.

V. CHARACTERIZATION OF THE STRUCTURE OF TURBULENT FLUID FLOW

A. Theoretical Consideration

The purpose of the present work on the investigation of grid-generated turbulence in a wind tunnel was to establish the applicability of the symmetrical laser Doppler velocity meter to the characterization of turbulence with its advantages over hot wire instruments. A synoptic review of the statistical theory of isotropic turbulence, necessary for relating the measured parameters to the structure of turbulence, is presented here.

At any point within the turbulent flow field the velocity vector randomly fluctuates both in magnitude and in direction. This three-dimensional character of turbulence can be conceived as a rotational motion where the mechanical energy is dissipated to internal energy through a cascade of eddies of diminishing size. The largest scale of these eddies, for a given Reynolds number, depends on the size of the channel (lateral dimensions) in which the fluid flow is contained. The smallest size of the eddies depends on the viscosity of the fluid. The equation of turbulent motion cannot be solved analytically and, as a result, both experimental and theoretical research have become a joint tool for the understanding of this physical phenomenon.

Fortunately, isotropic and homogeneous turbulence can be completely characterized[16,23] by its statistical parameters. Turbulence is called isotropic when the eddying motion is uniformly distributed such that the components in different directions have the same average magnitude

and when there is no correlation of motion between the orthogonal components. There is a strong tendency for turbulence to become isotropic in nature when not affected by the boundary walls. For example, the flow field at the center of a large diameter pipe approaches isotropic conditions when a well-developed turbulent flow is generated by placing grids at a sufficient distance upstream. Considering a condition in which turbulence in a fluid is uniformly distributed so that the average condition is the same anywhere in the flow field, the velocity components in a given set of orthogonal axes can be written

$$U = \overline{U} + u \tag{51}$$

$$V = \overline{V} + v \tag{52}$$

$$W = \overline{W} + w \tag{53}$$

where the mean value is defined by

$$\overline{U} = \frac{1}{T} \int_0^T U dt \tag{54}$$

and T is the time period large enough to include all small time scale fluctuations. If the pipe flow is in the direction of U, the mean flow $\overline{V} = \overline{W} = 0$. The root mean square values of the fluctuating components are

$$u' = \sqrt{\overline{u^2}} \; ; \quad v' = \sqrt{\overline{v^2}} \; ; \quad w' = \sqrt{\overline{w^2}} \tag{55}$$

and in isotropic conditions, by definition,

$$u' = v' = w' \tag{56}$$

and

$$\overline{uv} = \overline{vw} = \overline{wu} = 0 \; . \tag{57}$$

The above quantities are independent of time. The intensity of turbulence is defined by

$$I_T = \frac{u'}{\bar{U}} \tag{58}$$

and its magnitude depends on the Reynolds number and on the distance between the point of observation and the turbulence generating grids. The turbulence generated by the grids decays as this distance increases. The rate of loss of kinetic energy per unit volume is

$$-\tfrac{1}{2}\,\rho\bar{U}\,\frac{d}{dx}\,(\overline{u^2} + \overline{v^2} + \overline{w^2})$$

which, in an isotropic field, can be written as

$$-\frac{3}{2}\,\rho\bar{U}\,\frac{d}{dx}\,(\overline{u^2})$$

where ρ is the density of the fluid. Taylor[16] has shown that a simple law of decay holds provided the measurements are taken beyond the "shadow" region.

$$\frac{\bar{U}}{u'} = \frac{5x}{A^2M} + \text{Const.} \tag{59}$$

where x is the distance between the grids and the point of measurements, M is the mesh size of the grid, and A is a constant which depends on the grid shape and is to be measured experimentally. Equation (59) shows that U/u' has a linear relationship with x/M. If the diameter of the rod of the grid is approximately M/4 or less, the shadow region (where the mean velocity becomes variable) does not extend more than several mesh lengths.

Measurement of velocity at two points close together (compared to the diameter of a given size of eddy) will show definite correlations.

If the points are situated many diameters apart, the velocity correlations are likely to be small. The cross correlation of two point velocities is defined by

$$R(x, x + \xi) = \lim_{T \to \infty} \frac{1}{T} \int_0^T u_x \, u_{x+\xi} \, dt \tag{60}$$

where x and $x + \xi$ are two points separated by ξ in the x direction. In a stationary process, ξ can be replaced by $U\tau$, and one can measure the above quantity by measuring

$$R(\tau) = \lim_{T \to \infty} \frac{1}{T} \int_0^T u(t) \, u(t + \tau) \, dt \tag{61}$$

where τ is the time required by an element of fluid to travel the distance ξ and $R(\tau)$ is the autocorrelation function. When $\tau = 0$,

$$R(0) = \overline{u^2} \, . \tag{62}$$

The correlation function can be normalized such that,

$$R\eta(\tau) = \frac{R(\tau)}{R(0)} = \frac{\overline{u(t) \, u(t + \tau)}}{\overline{u^2}} \, . \tag{63}$$

Measurements of velocity in two orthogonal directions at the same time can be made to determine the Reynolds shear stress components $-\rho\overline{uv}$, $-\rho\overline{vw}$, $-\rho\overline{wu}$, each representing the rate of transfer of momentum across the corresponding surface. These components will be zero in true isotropic turbulence.

If one measures the correlation R_y between the values of u, the velocity in the x direction, at two points in the y-axis separated by y, the curve resulting from a plot of R_y versus y can be used to

calculate the average diameter of the eddies ℓ_y, defined as

$$\ell_y = \int_0^{\infty} R_y dy = \int_0^{y} R_y dy \tag{64}$$

where $R_y = 0$ at $y \geq Y$. Correspondingly, a length ℓ_x can be defined by the relation

$$\ell_x = \int_0^{\infty} R_x dx = \int_0^{x} R_x dx \tag{65}$$

where R_x is the correlation between u at two points at a distance x along the x-axis. Note that $R_x = 0$ for $x \geq X$.

The microscales, λ_x and λ_y, of turbulence are related to ℓ_x and ℓ_y by

$$\frac{\lambda_x^2}{\ell_x^2} = \frac{10}{(A\, R_{\ell x})} \tag{66}$$

$$\frac{\lambda_y^2}{\ell_y^2} = \frac{10}{(A\, R_{\ell y})} \tag{67}$$

where λ_x and λ_y indicate the diameter of the smallest eddies in the corresponding directions, and A is a constant determined by the shape of the turbulence generating grids. The Reynolds number of turbulence in the y direction is defined by

$$R_{\ell y} = \frac{u' \ell_y}{\nu} \tag{68}$$

where ν is the kinematic viscosity. In general, the above relations hold good for large values of $R_{\ell y}$. However, some experimental results[16] show validity of these equations for $R_{\ell y}$ as low as 10. In a similar manner, the diffusion lengths introduced in the Lagrangian concept of turbulent motion can be determined.

The probability distribution function of the fluctuating components of velocity in a turbulent flow field also depends on the distance x between the point of measurement and the grid. The effect of "shading frequency" can be observed near the turbulence generating grid. Thus, velocity fluctuations immèdiately after the grids will have an approximately flat distribution pattern. If the point of measurement is at a large distance compared to the mesh size, the velocity distribution will approach a nearly Gaussian pattern.

A more detailed picture of turbulence can be obtained if a plot is made of the kinetic energy distribution among the eddies of different size. Since each eddy size (ℓ) corresponds to a frequency ($\ell/\overline{U}$) of velocity fluctuations, it is convenient to plot the energy spectrum in the frequency domain. Obviously, the mean square value $\overline{u^2}$ can be regarded as the total contribution from all frequency components. Thus,

$$\int_0^\infty G_u(f)\, df = \overline{u^2} \tag{69}$$

where $G_u(f)$ is the power spectral density function of turbulence energy. If the energy spectrum is normalized,

$$\nu(f) = \frac{G_u(f)}{\overline{u^2}} \tag{70}$$

so that

$$\int_0^\infty \nu(f)\, df = 1 \,. \tag{71}$$

The Fourier transform of the correlation function gives the

spectral density, so that a measurement of one quantity is sufficient for computation of the other.

$$G_u(f) = 4 \int_0^\infty R_x(\tau) \cos(2\pi f\tau)\, d\tau \tag{72}$$

and

$$R_x(\tau) = \int_0^\infty G_u(f) \cos(2\pi f\tau)\, df \ . \tag{73}$$

The above quantities can be normalized by writing

$$\nu(f) = 4 \int_0^\infty R_\eta(\tau) \cos(2\pi f\tau)\, d\tau \tag{74}$$

$$R_\eta(\tau) = \int_0^\infty \nu(f) \cos(2\pi f\tau)\, df \tag{75}$$

where the subscript η refers to the normalized correlation coefficient.

The microscale as well as the macroscale of turbulence can be obtained from the energy spectrum.

$$\lambda = \frac{\overline{U}}{2\pi} \left[\int_0^\infty f^2\, \nu(f)\, df \right]^{-\frac{1}{2}} \tag{76}$$

and

$$\ell = \frac{\overline{U}}{4} \lim_{f \to 0} \nu(f) \tag{77}$$

where λ is the microscale of turbulence and ℓ is the macroscale or integral scale of turbulence. The above relationship between the turbulence scales and the energy spectrum has been based on the assumption that the turbulence is nearly isotropic. Examination of the self preservation of the correlation functions is also an important parameter in the characterization of turbulence.

Karman[16] has shown that for low Reynolds numbers

$$\frac{d\overline{u^2}}{dt} = -10\nu \frac{\overline{u^2}}{\lambda^2} \tag{78}$$

where t is the decay time measured with reference to the turbulence generating grid so that

$$t = \frac{x}{\overline{U}} \quad . \tag{79}$$

At the final decay period, the macroscale (ℓ) of turbulence approaches nearly constant values and the energy decay approaches an inverse square law relationship.

$$\overline{u^2} \sim t^{-2} \quad . \tag{80}$$

From the above relations, Karman derived that

$$\lambda^2 = \text{Const. x } t \quad . \tag{81}$$

B. Experimental Apparatus and Procedure

A channel with cross sectional area of 1.5 inches by 1.5 inches and 12 feet long was used in the present study. Air at room temperature was used as a fluid medium. Polydisperse dioctyl-phthalate aerosol with an average diameter of 0.8 micron and concentration of 10^7 particles/cc was used. The end connections to the air duct were made with flexible piping. The experimental arrangement is shown in Figure 52. The flow rate could be adjusted by changing the blower speed. The channel was mounted on a movable frame so the channel could be translated in the vertical and the horizontal directions by known displacements. At the center of the duct, lucite windows (17 cm x 3 cm x 3 mm) were provided on four sides.

1. Measurement of the effective bandwidth of the Doppler signal arising from a turbulent flow field:

In this experiment, it was intended to examine the effective spread of the Doppler signal arising from the velocity fluctuations using the spectrum analyzer display. The effective frequency spread (Δf), arising from the velocity fluctuations, increased with the turbulent intensity as the Reynolds number was increased. Since the instrumental frequency spread (δf) also increased with the mean velocity $\overline{U}$, it was necessary to determine δf experimentally for a constant velocity of the scatterer equal to the mean velocity of the air flow. This was accomplished by using a rotating surface scattering disk where the linear velocity of the scattering particles at the point of measurement was adjusted to give the same value of the center frequency of the Doppler signal as it was obtained with the fluid flow system for each value of the Reynolds number. In this set of experiments, the values of θ and α were not adjusted to give a minimal instrumental spread. Table V shows some experimental results giving the variation of the Doppler frequency bandwidth (Δf) with increasing value of the Reynolds number. The contribution from the instrumental frequency spread is also recorded.

2. Measurement of velocity profile of laminar flow:

The experimental setup is shown in Figure 31. Beginning with this experiment, the system parameters in the transmission and receiving optics were adjusted so that the instrumental frequency broadening (δf) of the Doppler signal was minimal using the simple optical components available. The beam geometry was such that the associated angles had

TABLE V

Total Frequency Spread at Different Reynolds Numbers

Fluid flow ($\sin \theta/2 = 0.1398$, $\sin \alpha/2 = 0.0143$)

mean velocity (cm/sec)	R_e	f_c	total frequency spread (Δf)	instrumental frequency spread (δf)
37.4	762	170 KHz	19 KHz	17 KHz
332.0	5300	1.5 MHz	390 KHz	100 KHz
595.0	10600	2.7 MHz	705 KHz	120 KHz
818.0	16600	3.7 MHz	1200 KHz	154 KHz

the following values: $\theta = 70^{\circ}$; $\alpha = 0.18^{\circ}$ and $\Delta\theta = 5^{\circ}$. The velocity at the center of the pipe was maintained at 32.2 cm/sec. The air duct was mounted at two ends on clamps which were supported on two elevating screws. These two stainless steel screws (0.5 inch diameter, 12 inches long) were coupled by a chain so that the rotation of one of the screws moved the duct in the vertical direction, keeping the duct horizontal. In this manner, the point of measurement of the fluid velocity could be moved along the lateral direction of the channel axis. Figure 53 is a plot of the experimental data showing the velocity distribution across the duct. The velocity distribution plot was normalized with respect to the mazimum velocity, V_{max}, to compare the experimental figures with the theoretically expected parabolic law. Departures from the theoretical curve were expected since the length of the upstream section of the duct was not long enough for laminar flow stabilization.

As the mean velocity was increased further, the velocity distribution near the center of the duct approached a flat profile. The flow became unstable when the velocity at the center of the pipe was greater than 40 cm/sec.

3. Decay of weak turbulence:

The experimental arrangement is shown in Figure 52. The velocity at the center of the pipe was maintained at 38.65 cm/sec. A grid, made of cylindrical rods (diameter 0.63 cm and M = 1.27 cm), was placed upstream of the optical window. The distance x between the point of observation and the turbulence generating grid was varied by moving the grid to the desired position. The demodulated Doppler signal was fed to a DISA model

55D70 correlator for plotting the auto-correlation of the velocity at the point of measurement as a function of time delay. The time delay (τ) was generated by using a sweep drive unit. The correlation unit was 2 Hz to 200 kHz. Since the turbulence frequency spectrum was in the low frequency range, a large time constant was used for integration (100 seconds) in the correlation process and a low sweep speed of 0.03 msec per one second real time was used. The maximum time delay (τ) that could be given in the correlator was 100 msec. The correlation curves for different x/M ratios are plotted in Figure 54.

During each measurement for auto-correlation for a fixed x/M ratio, the signal was also recorded on a Sanborn recorder at its highest recording speed, giving a flat frequency response up to 30 Hz. A typical signal record is shown in Figure 55. The signal was recorded for approximately 10 seconds for each value of x/M. The recorded signal was then digitized using a Mosely Model 2A line follower and a Digitec punch controller and the paper punching setup. The signal processing and the digitization system are shown in block diagram, Figure 56. The punched tape contained the output data in a format that could be fed directly to the GE 635 time-sharing computer terminal. The sampled data were then analyzed for determining the statistical parameters in characterizing turbulence. Fortran IV computer language was used in the computer program. Appendix III gives an analysis of the digital computation using an equal time interval sampling process. A copy of the computer program used is included in Appendix III.

The "output" of a typical computer run is given in Table VI. Table VII presents some of the computed values of the characteristic parameters of turbulence decay as obtained from the digital analysis. Figure 57 shows the velocity correlation curves obtained for different values of x/M and Figure 58 shows the energy spectrum. A plot of $\overline{U}/u'$ versus x/M is given in Figure 59 for values of x/M greater than 10. Energy decay of weak turbulence is plotted versus the decay time in Figure 60. The square of the microscale of turbulence is plotted versus the decay time in the same figure.

C. Discussion of Results

The value of $\overline{U}/u'$ plotted versus x/M in Figure 59 shows an approximate linear relationship, which is in accordance with the expected result. Since

$$\frac{\overline{U}}{u'} = \text{Const.} + \frac{5}{A^2} \cdot \frac{x}{M}$$

where the slope measured from Figure 59,

$$\text{slope} = 0.6 = \frac{5}{A^2}$$

$$A = 2.8 .$$

This value is in the range of previously obtained[16] experimental results on isotropic turbulence using rounded bars as turbulence generating grids ($A \approx 2.12$).

Further, since it is possible to write

$$\lambda/M = A\sqrt{\frac{\nu}{u'M}}$$

TABLE VI

COMPUTER "OUTPUT" OF THE TURBULENCE PROGRAM FOR X/M=18.00

XBAR= 3.9043
UMIN=-10.86452 UMAX= 9.0548 C= 0.830 K= 24 N= 600

PROBABILITY DENSITY FUNCTION

N	F(U)	U(CM/SEC)	LOG(N)
1	0.17	-10.035	*
2	0.33	-9.205	**
6	1.00	-8.375	******
5	0.83	-7.545	*****
15	2.50	-6.715	**********
22	3.67	-5.885	**********
30	5.00	-5.055	**********
26	4.33	-4.225	**********
31	5.17	-3.395	**********
34	5.67	-2.565	**********
27	4.50	-1.735	**********
27	4.50	-0.905	**********
44	7.33	-0.075	**********
44	6.67	0.755	**********
45	7.50	1.585	**********
36	6.00	2.415	**********
59	9.83	3.245	**********
44	7.33	4.075	**********
39	6.50	4.905	**********
45	7.50	5.735	**********
9	1.50	6.565	*********
5	0.83	7.395	*****
3	0.50	8.225	***
5	0.83	9.055	*****

U(MEDIAN)= 0.7548 F(0)= 16.0441 G(0)= 2.0134

UBAR= 38.6500CM/SEC, URMS= 4.0055CM/SEC,

TURBULENT INTENSITY= 0.1036(X100 PERCENT)

TABLE VI CONTINUED

T(SEC)	F(T)	FC(T)	F(HZ)	((F)
0.000	16.04	1.00	0.000	2.01
0.009	15.19	0.95	1.384	2.44
0.018	13.40	0.84	2.769	2.50
0.027	11.19	0.70	4.153	1.97
0.036	8.80	0.55	5.537	1.46
0.045	6.56	0.41	6.921	0.80
0.054	4.62	0.29	8.306	0.44
0.063	2.92	0.18	9.690	0.31
0.072	1.48	0.09	11.074	0.17
0.081	0.34	0.02	12.458	0.11
0.090	-0.54	-0.03	13.843	0.09
0.099	-1.10	-0.07	15.227	0.07
0.108	-1.43	-0.09	16.611	0.05
0.117	-1.59	-0.10	17.996	0.04
0.126	-1.67	-0.10	19.380	0.03
0.135	-1.69	-0.11	20.764	0.01
0.144	-1.63	-0.10	22.148	0.01
0.154	-1.48	-0.09	23.533	0.01
0.163	-1.28	-0.08	24.917	0.01
0.172	-1.14	-0.07	26.301	0.01
0.181	-0.98	-0.06	27.685	0.01
0.190	-0.85	-0.05	29.070	0.01
0.199	-0.77	-0.05	30.454	0.01
0.208	-0.82	-0.05	31.838	0.01
0.217	-1.04	-0.06	33.223	0.01
0.226	-1.37	-0.09	34.607	0.01
0.235	-1.78	-0.11	35.991	0.01
0.244	-2.20	-0.14	37.375	0.01
0.253	-2.57	-0.16	38.760	0.01
0.262	-2.86	-0.18	40.144	0.00
0.271	-3.06	-0.19	41.528	0.00
0.280	-3.08	-0.19	42.913	0.00
0.289	-2.97	-0.19	44.297	0.00
0.298	-2.75	-0.17	45.681	0.00
0.307	-2.48	-0.15	47.065	0.00
0.316	-2.28	-0.14	48.450	0.00
0.325	-2.20	-0.14	49.834	0.00
0.334	-2.18	-0.14	51.218	0.00
0.343	-2.22	-0.14	52.602	0.00
0.352	-2.15	-0.13	53.987	0.00
0.361	-1.99	-0.12	55.371	0.00

DELTA= 0.009SEC
F(0) COMPUTED FROM SPECTRUM = 16.0441
MICROSCALE= 0.70CM

TABLE VII

Some Statistical Parameters of Turbulence at Low Reynolds Number

x/M	Decay Time t sec	u' cm/sec	Turbulence Intensity %	ℓ_x cm	R_{ℓ_x}	λ_x Calculated cm	λ_x Observed cm	ℓ_x/λ_x
12	0.396	5.7	14.86	1.08	41.5	0.51	0.54	2.0
18	0.595	4.0	11.68	1.20	36.4	0.58	0.70	1.7
24	0.792	2.5	6.50	2.16	36.7	0.75	1.00	2.1
30	0.990	1.7	4.46	2.72	31.4	0.94	1.38	2.0

one can calculate λ from the above relationship. Thus,

$$\lambda = 0.51 \text{ cm}$$

for $x/M = 18$, $u' = 4.0$ cm/sec and $\nu = 0.148$ cm^2/sec for air at room temperature. From Table VII it is found that the value obtained from the digitized data is 0.7 cm. The discrepancy is probably due to non-isotropic conditions of the flow system investigated.

The correlation curves obtained from the sampled data taken for a short interval of time ($\simeq$ 10 seconds) agreed well with the analog correlation curves where a single run was taken for about 55 minutes. This agreement between the two analyses indicates that the total sampling time and the sampling intervals used were adequate. The analog correlator output was noisy. This noise was expected since the signal was a stationary random function of low frequency; the mean square circuit with a finite time constant would show fluctuations at the output. It was expected that a better resolution could be achieved at a low frequency by the digital methods rather than the analog technique.

The slope of the energy decay curve as a function of decay time is -2.2, which is in good agreement with Taylor's inverse square decay law of turbulence energy at the final decay period. The square of the micro-scale of turbulence in this period increases linearly with t as is expected from the analysis made by Karman.[16] Table VII shows general agreement between the measured turbulence scales with calculated values.

The application of the laser Doppler velocity meter presented here was limited to the characterization of turbulence of low Reynolds number. Turbulence of high Reynolds number could not be investigated because of

the lack of an adequate wind tunnel. The present work, however, indicates that a symmetrical laser Doppler velocity meter can be employed in the characterization of turbulence both in subsonic and supersonic flow regions. Table VIII shows some of the relative merits and demerits of the symmetrical laser Doppler system compared to a hot wire or hot film anemometers - in their application to the studies of the structure of fluid velocity fields.

TABLE VIII

A Comparative Study on the Performance of a Hot Wire Anemometer and Symmetrical Laser Doppler Velocity Meter in Turbulence Characterization

	Hot Wire Anemometer	Symmetrical Laser Doppler Velocity Meter
System equation	$V = \sqrt{A+BU^m}$ (nonlinear) V = volts (output); U = velocity; A, B and m are constant in a small velocity interval. In general, A, B and m are functions of Reynolds No., gas density, conductivity, temp., etc.	$f = KU$ (linear) f = frequency (Doppler shift) K = constant; U = velocity Velocity measurements are not generally affected by the properties of the flow medium.
Calibration	Must be calibrated	Provides a method for absolute measurement of velocity
Sensing Volume	Wire dia. ≈ 10μ, ℓ = 1.5mm; probe dia. = 3 mm (typical)	d ≈ 5μ; ℓ = 600μ (using corrected optics)
Interaction with the flow medium	Disturbs flow field	No significant interaction
Limits of measurement	Measurement of velocity generally limited to 20 cm/sec to 150 m/sec for air	Can be used both in subsonic and supersonic flow region
Temperature limit	Normally designed for max fluid temp of 250°C	Can be used at fluid temp up to 1000°C or higher depending on the Brownian motion of the aerosol particles
Contamination	Corrosion and contamination affects calibration	Scattering aerosol (range 0.5μ to 2μ dia) must be present within the fluid medium
Frequency response	Upper frequency limit of a hot wire is about 500 Hz; the response is extended to 40 kHz or higher by using appropriate electronic compensation circuitry	Frequency response of a laser Doppler system is much higher compared to the highest turbulence frequency in fluid flows. However, scattering particle inertia may become significant in the regions of high local accelerations in supersonic flows

TABLE VIII. Continued

	Hot Wire Anemometer	Symmetrical Laser Doppler Velocity Meter
Directional ambiguity of 180° in velocity measurement	Present	Can be eliminated by using a frequency biasing technique
Noise level	Generally equivalent to 0.5% turbulence intensity level at moderate velocity	Approximately equivalent to 0.5% turbulence intensity, primarily caused by instrumental frequency broadening
Remote measurement	Not possible	Remote sensing possible

VII. CONCLUSIONS

The symmetrical heterodyning system in the laser Doppler method of velocity measurement does not possess receiving aperture broadening of the signal. The Doppler signal frequency is independent of the scattering angle and the laser light beam alignment is simple. These characteristics result in a relatively high signal-to-noise ratio compared to other heterodyning systems.

The symmetrical heterodyning method is advantageous as long as signal power can be appreciably increased by increasing the receiving aperture area. If the power of the scattered beam falling on the photocathode is 10^{-10} watts or higher, the symmetrical system of heterodyning is advantageous compared to the other methods of optical heterodyning. Local oscillator heterodyning is advantageous when aperture broadening of the signal is insignificant for scattering sites located at large distances.

The method of frequency biasing by employing a rotating diffraction grating is an efficient technique for removing directional ambiguity from velocity measurements.

A careful optimization of the system parameters is essential for the minimization of the instrumental frequency spread and to obtain high SNR. This optimization also results in higher accuracy and better spatial resolution in localized fluid flow measurement.

A simple and efficient analog frequency-to-voltage conversion device was constructed using a phase-locked loop system available as an integrated circuit.

Scattering aerosols must be present in the fluid medium for turbulence studies employing a symmetrical laser Doppler velocity meter. Aerosol in the size range of 0.5 to 1 micron diameter (unit density) follows turbulence eddies and the effect of fluid temperature will not cause any appreciable error for temperatures below 500^{o}C.

An excellent agreement observed between the theoretical and experimental results indicates that the symmetrical heterodyning process can be gainfully employed on the studies of the structure of turbulent fluid flow. The system has many advantages over hot wire anemometers.

REFERENCES

1. Angus, J. C., et al., Industrial and Engineering Chemistry, 61; No. 2, p. 8 (1969).

2. Ballard, G. S., Personal Communication

3. Bendat, Julius S. and Piersol, Allan G., "Measurement and Analysis of Random Data", John Wiley and Sons, New York, New York, 1966.

4. Berman, N. S., et al., AIChE J., 15; 323 (May 1969).

5. Bond, Robert L., "Contribution of the System Parameters in the Doppler Method of Fluid Velocity Determination", Ph.D. Dissertation, University of Arkansas, 1968, NASA-CR-95221.

6. Bourke, P. J., et al., Phys. Letters, 28A; 692 (Feb. 1969).

7. Call, Roger W., Palmer, E. Paul and Richard W. Grow, "Measurement of the Atmospheric Aerosols by Polarized-Laser Light Scattering", Utah University, UTEC-MD-67-034; NSF-11, 1967.

8. Chung, Jim S. (Ph.D. Thesis), "Laser Anemometer Measurements of Turbulence in Non-Newtonian Pipe Flow", Michigan University Report 06505-4-T; AD699533, 1969.

9. Davis, C. N., "Aerosol Science", Academic Press, New York, New York, 1966.

10. Davis, Donald T., ISA Trans., 7; 43 (1968).

11. Deirmendjian, Diran, "Electromagnetic Scattering on Spherical Polydispersions", American Elsevier Publication Co., New York New York, 1969.

12. Foreman, J. W., Jr., George, E. W. and Lewis, R. D., Appl. Phys. Letters, 7; 77 (1965).

13. Foreman, J. W., Jr., et al., IEEE J. Quantum Electron., QE-2; No. 8, p. 260 (Aug. 1966).

14. Forrester, A. T., Gudmundsen, R. A. and Johnson, P. O., Phys. Rev., 99; p. 1691 (Sept. 15, 1955).

15. Friedlander, S. K. and Johnstone, H. F., Ind. Engr. Chem., 49; 1151 (July 1957).

16. Friedlander, Sheldon K. and Topper, L., editors, "Turbulence: Classic Papers on Statistical Theory", Interscience Publication Inc., New York, New York, 1961.

17. Fuchs, N. A., "Mechanics of Aerosols", Pergamon Press, Elmsford, New York, 1964.

18. Gardner, Floyd M., "Phase-Lock Technique", John Wiley and Sons, New York, New York, 1966.

19. Goldstein, R. J. and Hagen, W. F., Phys. Fluids, 10; 1349 (June 1967).

20. Goldstein, R. J. and Kreid, D. K., Trans. ASME., Ser. E., J. Appl. Mech., 34; 813 (Dec. 1967).

21. Green, H. L. and Lane, W. R., "Particulate Clouds, Dusts, Smokes and Mists", E. & F. N. Spon Ltd., London, U. K., 1964.

22. Haus, H. A. and Townes, C. H., Proc. I.R.E. (Corr.), 50; 1544 (June 1962).

23. Hinze, J. O., "Turbulence", McGraw-Hill Book Co., New York, New York, 1959, p. 71.

24. Huffaker, R. M., Appl. Opt., 9; 1026 (May 1970).

25. Jackson, D. A. and Paul, D. M., J. Sci. Instr., Ser. 2, 2; 1077 (Dec. 1969).

26. Jenkins, Francis A. and White, Harvey E., "Fundamentals of Optics", McGraw-Hill Book Co., 3rd edition, New York, New York, 1957, p. 137.

27. Kerker, Milton, editor, "Electromagnetic Scattering; Proceedings" Pergamon Press, New York, 1963, p. 87.

28. Kleinhans, W. and Fried, D. L., Appl. Phys. Letters, 7; 19 (July 1965).

29. Kovasznay, L. S. G., Turbulence Measurements, in "Physical Measurements in Gas Dynamics and Combustion", Rudolf W. Ladenburg, et al., editors, Princeton University Press, New Jersey, 1954, p. 277.

30. Laufer, John J., Aeronautical Sci., 17; 277, (May 1950).

31. Lennert, A. E., et al., "Laser Application for Flow Field Diagnostics", Paper presented at the second National Laser Industry Association Meeting, Los Angeles, California, October 20-22, 1967.

32. Lewis, R. D. and Chatterton, N. E., and Watson, H. J., "Investigation of Two-Dimensional Flow Measurements Using the Laser Doppler Technique ", Brown Engr. Co., TN-AST-285, AD-685 249, 1968.

33. Lindeken, C. I., et al., Ind. Hygiene J., p. 473, Nov.-Dec. 1962.

34. McAleer, H. Proc., I.R.E., 47; 1137 (1959).

35. Monroe, Marvin E., "Noise in an Optical Homodyne System", Ohio State University Rept. -1935-7; AD 474 465, Oct. 1965.

36. Muller, A., Appl. Opt., 9; 2393 (1970).

37. Oliver, B. M., Proc. I.R.E. (Corr), 49; 1960 (1961).

38. Parrish, E. C. and Schneider, R. W., "Tests of High Efficiency Filters and Filter Installations at ORNL", Oak Ridge National Lab. ORNL-3422, June 1963.

39. Pendorf, R., J. Opt. Soc. Am., 52; 402 (1962).

40. Pike, E. R., et al., J. Sci. Instr., Ser. 2, 727 (1968).

41. Reisman, E., et al., Appl. Opt., 6; 1969 (1967).

42. Ross, Monte, "Laser Receivers", John Wiley and Sons, New York, New York, 1966.

43. Rudd, M. J., J. Sci. Instr., Ser. 2, 2; 55 (1969).

44. Schwartz, Mischa, "Information Transmission, Modulation and Noise", McGraw-Hill Book Co., New York, New York, 1959, p. 304.

45. Thomas, John B., "An Introduction to Statistical Communication Theory", John Wiley and Sons, New York, New York, 1969, p. 459.

46. Wankum, D. L., "Measurement of Film Grain Size and Its Contribution to Noise in Wavefront Reconstruction", in "Investigation of Laser Properties Relevant to the Measurement of Different Physical Parameters", Testerman, M. K., Univ. of Arkansas, NASA CR-97761, 1969, P. 16-26.

47. Welch, N. E. and Tomme, W. J., "The Analysis of Turbulence from Data Obtained with a Laser Velocimeter", AIAA Paper No. 67-179, AIAA 5th Aerospace Sciences Meeting, New York, New York, Jan. 23-26, 1967.

48. Willard, G. W., J. Acoust. Soc. Am., 21; 101 (1949).

49. Yeh, Y. and Cummins, H. Z., Appl. Phys. Letters, 4; 176 (1964).

50. "Subroutine for Computing the Parameters of the Electromagnetic Radiations Scattered by a Sphere", IBM Program No. PIDIHDR 08-360D174002B, May 1968.

51. "Table of Scattering Functions for Spherical Particles", Department of Commerce, National Bureau of Standards, Appl. Math. Ser. 4, Jan. 1949.

APPENDIX I

DERIVATION OF THE DOPPLER FREQUENCY SHIFT FROM INTERFERENCE THEORY AND AN ANALYSIS OF THE SIGNAL FREQUENCY SPECTRUM

Derivation of the Doppler frequency shift in the two incident beam symmetrical system of heterodyning can be made from the spatial frequency of the interference fringes formed at the beam intersection. Consider two coherent beams of circular cross section crossing at an angle θ. Assuming plane parallel wave fronts, the interference fringes produced at the beam intersection will have fringe separation

$$d_i = \frac{\lambda_o}{2 \sin \theta/2}$$

which corresponds to a spatial frequency f_i

$$f_i = \frac{1}{d_i} = \frac{2 \sin \theta/2}{\lambda_o} .$$

When a scattering particle passes through this fringe pattern, the scattered light will undergo amplitude fluctuation having a frequency f_c given by the product of the spatial frequency of the interference fringes and the component of the particle velocity in a direction perpendicular to the fringe pattern.

Thus,

$$f_c = f_i \times U$$

$$= \frac{2U}{\lambda_o} \sin \theta/2$$

which is identical with equation (11). If the scattering particles are

separated in space by a distance greater than D (Figure 61), the signal will appear on the detector as discrete "signal bursts". If the inter-particulate distance is less than D, the signal will be continuous in time but will have amplitude modulation. Finite lifetime of the signal or amplitude modulation of the signal will give rise to a frequency spread of the Doppler spectrum (δf_τ). There is no transmission aperture broadening in this case since there is no uncertainty in the angle θ, considering plane parallel wave fronts. Thus, $\delta f_a = 0$ but $\delta f_\tau \neq 0$. In practice, two beams meeting at an angle θ are focused at the point "O" to obtain higher power density at the sensing volume. This focusing of the incident beams introduces a finite uncertainty in the angle θ, and the wave fronts are no longer plane parallel. The actual shape of the wave fronts will also depend on the spherical aberration of the lens and the diffraction effect. Considering two concentric spherical wave fronts crossing in the focal region (Figure 62), the shape of the interference fringe pattern will be different from those obtained in the case of plane parallel wave fronts. The spatial frequency of these fringes will not have a unique value and can be represented by a spectrum of spatial frequency around the center frequency f_i. The path of a scattering particle with velocity U will give rise to a scattered wave having a finite bandwidth of signal frequency. This frequency spread is the transmission aperture broadening of the signal (δf_a) referred to previously.

In the above analysis, the velocity component of the particle, U, was assumed constant and no spatial velocity gradient of the particles

in the sensing volume was considered. If a velocity gradient is present, the Doppler signal will have frequency broadening δf_s.

"Zero Frequency" Doppler Spectrum

A typical Doppler spectrum will display Doppler shift around "zero frequency" in addition to the signal at f_c. This spectrum comes from the fact that when a beam of laser light is focused at the point "O", the rays focused with an angle α (Figure 1) will produce interference fringes at the focal spot. The spatial frequency of these fringes is maximum for the two outermost wave vectors and it gradually decreases to zero as the angle α between the wave vectors decreases to zero. The latter condition is satisfied by the wave vectors lying on the optical axis. Thus, if a cone of a laser light is focused at a moving scatterer as shown in Figure 1, a Doppler signal spectrum will be observed around "zero frequency" if the scattered light is allowed to fall on the photomultiplier without any additional beam mixing. The frequency spread of this signal is proportional to the component of particle velocity on the focal plane irrespective of the direction. The measurement of this spread of frequency will give the speed of the scattering particles or the velocity components projected on the focal plane. The method has some potential application in the measurement of Brownian motion of submicron scattering aerosol which can be related to the temperature of the fluid.

The Doppler shift around "zero frequency" may have two adverse effects in signal processing while the signal is processed at the frequency f_c. First, it might set the lower limit of the dynamic

range in the measurement of one of the velocity components, and secondly, there may be some deterioration of SNR of the signal of frequency f_c if the effective bandwidth of the "zero frequency" signal encompasses a large frequency range. This is possible if one velocity component fluctuates while another is being measured. For example, if measurements are taken on U, while V has a fluctuation such that

$$V = \bar{V} + v_o \cos pt$$

where $\bar{V}$ is the mean velocity and p is the angular frequency. The Doppler spectrum around the "zero frequency" due to the component V can be written as

$$f_V = \frac{2\bar{V}}{\lambda_o} \sin \alpha/2 + \frac{2v_o \sin \alpha/2}{\lambda_o} \sin pt$$

and the output voltage of the photomultiplier can be represented by

$$e_V = E \sin (\omega t + M \sin pt)$$

$$= E \left[J_o(M) \sin \omega t + \sum_{n=1}^{\infty} J_n(M) \sin (\omega + np)t \right.$$

$$\left. + \sum_{n=1}^{\infty} (-1)^n J_n(M) \sin(\omega - np)t \right]$$

where

$$\omega = \frac{4\pi\bar{V}}{\lambda_o} \sin \alpha/2$$

and

$$M = \frac{4\pi v_o \sin \alpha/2}{\lambda_o p}$$

and $J_n(M)$ is the Bessel function of the first kind and nth order with argument M and E is a constant. The above equation indicates that

effective bandwidth can become large and may cause appreciable interference in the desired signal frequency range around f_c.

APPENDIX II

LIST OF MAJOR COMPONENTS AND EQUIPMENT USED

A. Laser

Spectra Physics; Mountain View, California; Model 125 He-Ne laser, λ = 6328 A, rated output power = 50 mW.

Power supply: Spectra Physics Model 250 Exciter unit.

B. Granite Table

Herman Stone Company; Dayton, Ohio; granite surface plate mounted on a three-point suspension system.

C. Optical Benches

Baling Corporation; Cambridge, Massachusetts; Model 22-950 lathe bed optical bench.

D. Optical Components

Edmund Scientific Company; Barrington, New Jersey; front surface mirrors, Al-coated with SiO overcoat, 90 to 95 percent reflectivity. Plano convex lenses of different focal lengths. Diffraction grating replica, 13,400 lines/inch.

Spectra Physics Model 511 beam splitters, transmission loss less than 2 percent.

Optical Technology Inc.; Palo Alto, California; neutral density filters.

Baldwin Electronics Co.; Little Rock, Arkansas; encoder disk, 9 inches diameter, outermost track having a spatial frequency of 100 lines per mm.

E. Detectors

RCA, Harrison, New Jersey; RCA 4526 and RCA 7265 photomultipliers, S-20 response.

Spectra Physics Model 401 laser power meter.

F. Scattering System

Surface scattering disk: sand blasted aluminum disk and 20 micron diameter pigment particles (3M Co.) painted on an aluminum disk.

Drive unit: Joy Manufacturing Co.; New Philadelphia, Ohio.; Model AVP-42351794 synchronous motor working on three phase supply; excitation frequency, 400 Hz.

Behlman-Inver Electronics; Santa Monica, California; Invertron Model 503A ac power supply having variable output frequency 290 to 550 Hz.

G. Refractometer

Bausch and Lomb; Rochester, New York; Catalog No. 33-45-58, ABBE-3L refractometer

H. Electronic Data Processing Equipment

C-COR Electronics Inc.; State College, Pennsylvania; Model 4366E wide band solid state pre-amplifier, frequency range 10 kHz to 200 MHz, gain 1000.

Singer Metrics; Bridgeport, Connecticut; Model SPA 3/25a spectrum analyzer, frequency range 1 kHz to 25 MHz.

Tektronix, Inc.; Portland, Oregon; type 535 oscilloscope.

Fluke Co.; Seattle, Washington; Model 415B high voltage power supply, 0 to ±3000 volts, adjustable.

Hewlett Packard; Atlanta, Georgia; Model 5210 A frequency meter discriminator, range 10 Hz to 10 MHz.

Krohn Hite Corporation; Cambridge, Massachusetts; Model 3100 band pass filter, pass band adjustable between 10 Hz to 1 MHz.

Lectronics Research Laboratories; Philadelphia, Pennsylvania; Model TS-4B B/U signal generator, range 230 kHz to 40 MHz.

DISA Electronics; Franklin Lakes, New Jersey; DISA type 55D70 Correlator, frequency range 20 Hz to 200 kHz.

DISA type 55D75 time delay unit, range 0.1 msec to 100 msec.

Ramp function generator for sweep drive unit, range 0 to ±5 volts, sweep speed adjustable from 0.36 mV/sec to 0.36 volts/sec in 20 steps. (The unit was constructed in this laboratory).

Phase-locked loop FM demodulator using Signetics NE 561B PLL integrated circuits; frequency range 1 Hz to 15 MHz; low pass filter, cut-off frequency 500 Hz; AM modulator and demodulator. (Two units were constructed in this laboratory).

AGC amplifier, gain 10, frequency range 100 kHz to 15 MHz. (The unit was constructed in this laboratory).

Hewlett-Packard; Atlanta, Georgia; Model 6215A power supply, 0 to ±30 volts adjustable.

Hallicrafter Co.; Chicago, Illinois; Model S-76 communication receiver range 535 kHz to 34 MHz.

Philco Corporation; Philadelphia, Pennsylvania; Model BC-221-E Signal Corps frequency meter, crystal controlled frequency generator, range 125 kHz to 20 MHz.

Hewlett-Packard, Model 2D-2A X-Y recorder.

Sony Corp.; Tokyo, Japan; Sony Model TC-355 tape deck, frequency response: 20 Hz to 22 kHz at 7.5 inches per second tape speed.

Hewlett-Packard Model 425A dc microvoltmeter, range 10 microvolts to 1 volt.

Sanborn Co.; Cambridge, Massachusetts; Model 60-1300 Twin-Viso strip chart recorder, frequency response: 0 to 30 Hz.

I. Digital Data Processing System

United System Corporation; Dayton, Ohio; System No. F9375 data punching system containing the following units: (1) Model 251A/251-1 digital voltemeter; (2) Model 623 punch controller; and (3) Model 671 paper tape punch.

Hewlett-Packard Model 2D-2A X-Y recorder and line follower.

Moseley Autograf Type F-3B line follower.

Hewlett-Packard Model 6215A dc power supply, range 0 to ±30 volts.

Ramp function generator. (The unit was constructed in this laboratory).

Exact Co.; Hillsboro, Oregon; Model 240 function generator.

Hewlett-Packard Model 521E electronic counter.

J. Computer

General Electric Co.; Bethesda, Maryland; GE 635 Time Sharing Computer Terminal.

APPENDIX III

DIGITIZATION AND COMPUTER PROCESSING

A. Sampling Interval

In the digitization process, the sampling interval was so chosen that the cut-off frequency f_c, given by

$$f_c = 1/2h$$

was appreciably higher than the maximum value of the signal frequency f_m. In the above expression, h is the sampling interval. The value of h was maintained so that the frequency f_c is at least twice that of the maximum frequency of interest.[3]

B. Mean Velocity

$$\overline{U} = \frac{1}{N} \sum_{n=1}^{N} U_n$$

where N is the total number of samples.

C. Transformation of Data to Zero Mean Value

$$u_n = U_n - \overline{U}$$

so that

$$\overline{U}_n = 0.$$

D. RMS Value of the Velocity Components and Turbulence Intensity

$$\overline{u^2} = \frac{1}{N} \sum_{n=1}^{N} (u_n)^2$$

$$u' = \sqrt{\overline{u^2}}$$

and the intensity of turbulence is defined by

$$I_T = \frac{u'}{\overline{U}} \times 100 \text{ percent.}$$

E. Probability Density Histogram

The probability density function p(u) is given by

$$p(u) = \lim_{\Delta u \to 0} \frac{\text{Prob}\left[u < u(t) < u + du\right]}{\Delta U}$$

$$= \frac{dP(u)}{du}$$

where P(u) is the probability distribution function

$$P(u) = \int_{-\infty}^{u} p(\xi)\, d\xi$$

where ξ is a dummy variable. For large N, the number of class interval k can be chosen as

$$k = 1.87\ (N-1)^{2/5}$$

and if the maximum and minimum value of the velocity is b and a respectively, then the width of the interval c is

$$c = (b - a)/k\ .$$

The total number of data points N_i in the class interval d_i, where

$$d_i = a + ic, \quad i = 1, 2, 3, \cdots k,$$

can be plotted against k giving the desired histogram of fluctuating velocity components. The probability density can be expressed as the percentage of data,

$$p_i = N_i/N \times 100 \text{ percent} .$$

The median can be calculated from the velocity histogram.

F. Auto-correlation

The maximum number of correlation lag values m is chosen as

$$m = N/15$$

so that the maximum delay that will be introduced in the auto-correlation measurement is

$$\tau_{max} = mh .$$

Thus, the resolution bandwidth of the power spectra will be

$$B_s = \frac{1}{mh} = \frac{1}{m(1/2f_c)} = \frac{2f_c}{m}$$

for $-f_c < f < f_c$.

The power spectra are calculated at discrete frequencies separated by an interval f_c/m, and only for positive values of the frequency f.

The auto-correlation function can be written as

$$R(rh) = \frac{1}{N - r} \sum_{n=1}^{N-r} U_n U_{n+r}$$

$$r = 0, 1, 2, 3, \cdots, m$$

where r is the lag number and is related with the time delay by

$$rh = \tau(\text{displacement}).$$

The normalized auto-correlation coefficient

$$R_c(rh) = \frac{R(rh)}{R(o)} .$$

G. Power Spectra

The power spectral density function $G_u(f)$ is given by

$$G_u(f) = 4 \int_o^\infty R_u(\tau) \cos 2\pi f\tau d\tau$$

calculated at the discrete frequencies

$$f = K \frac{f_c}{m}, \qquad K = 0, 1, 2, 3, \cdots, m .$$

Thus,

$$G_u\left(\frac{Kf_c}{m}\right) = 4 \int_o^\infty R_u(rh) \cos \frac{2\pi K f_c}{m} \cdot rh \, d(rh)$$

$$= 2h \left[R(o) + 2 \sum_{r=1}^{m-1} R(r) \cos\left(\frac{\pi r K}{m}\right) + (-1)^K R(m) \right] .$$

The above spectrum $G_u(f)$ gives a "raw estimate" of the true power spectral density. A smooth estimate can be obtained by taking

$$\tilde{G}_o = 0.5\, G_o + 0.5\, G_1$$

$$\tilde{G}_K = 0.25\, G_{K-1} + 0.5\, G_K + 0.25\, G_{K+1}$$

$$\tilde{G}_m = 0.5\, G_{m-1} + 0.5\, G_m$$

$$K = 1, 2, 3, \cdots, m-1$$

where $\tilde{G}_K$ represents the smooth estimate and $G_K = G_u\left(\frac{Kf_c}{m}\right)$.

To calculate the modified spectrum, a function D_r is generated such that

$$D_r = D(rh) = \frac{1}{2}\left(1 + \cos\left(\frac{\pi r}{m}\right)\right), \qquad r = 0, 1, 2, \cdots, m,$$

$$= 0 \qquad r \geq m$$

$$\tilde{G}_K = \tilde{G}\left(\frac{Kf_c}{m}\right) = 2h\left[R_o + 2\sum_{r=1}^{m-1} D_r R_r \cos\left(\frac{\pi rK}{m}\right)\right]$$

giving the desired power spectrum. Since the sum of all power components will be equal to the total power given by $\overline{u^2}$,

$$\sum_{K=0}^{m} G_K = \overline{u^2}$$

it is possible to check the accuracy of the computed spectrum by adding the individual components and comparing this with the value R(0), since,

$$\overline{u^2} = R(0) \ .$$

To normalize this one-dimensional power spectrum, it is convenient to express

$$\nu_K = \frac{\tilde{G}_K}{\overline{u^2}} \qquad \text{for } K = 0, 1, 2, \cdots, m$$

so that

$$\sum_{K=0}^{m} \nu_K = 1 \ .$$

H. Microscale of Turbulence

$$\lambda_x = \frac{\overline{U}}{2\pi}\left[\sum_{K=0}^{m} f(K)^2 \, \nu_K\right]^{-\frac{1}{2}}$$

I. Integral Scale of Turbulence

$$\ell_x = \overline{U}\left[\sum_{r} R_c(rh)\right] \ .$$

The above summation is made from rh = 0 to rh = τ_m, such that

$$R_c(rh) \approx 0 \qquad \text{for } \tau_m \geq \tau \ .$$

COMPUTER PROGRAM

```
100C  TURBULENCE STRUCTURE ANALYSIS
110   DIMENSION DEL(50),FC(50)
120   REAL INTENSITY
130    DIMENSION Y(100),MM(100)
140    COMMON X(1000),XMIN, XMAX,C,K,M(50),F(50),FC(50),
150    & F(50),G(50),DN(50)
160    ALPHA PONT, LINE(62)
170    DATA PONT/"*"/
180   PRINT,"N,FACTOR,UBAR,DELTA,DISNORM(X/M)"
190   INPUT, N,FACTOR,UBAR,DELTA,DISNORM
200   READ("DATAFILE",99)(X(I),I=1,N)
210   99 FORMAT(F6.3)
220   MAXDNO=N/15
230   IF(MAXDNO.GT.50)MAXDNO=50
240   FC=1./(2.*DELTA)
250   DO 361 I=1,MAXDNO
260   F(I)=I*FC/MAXDNO
270   361 DEL(I)=I*DELTA
280    XBAR=XMEAN(N)
290    DO 2 I=1,N
300   2 X(I)=(X(I)-XBAR)*FACTOR
310   DO 801 I=1,N; IF(X(I).LT.(-20.))X(I)=0.;801 CONTINUE
320    XMIN=X(1); XMAX=X(1)
330    DO 18 I=2,N
340    IF (X(I).LT.XMIN)XMIN=X(I)
350    IF(X(I).GT.XMAX)XMAX=X(I)
360    18 CONTINUE
370   XRMS=RMS(N); RO=XRMS**2
380    INTENSITY=XRMS/UBAR
390C  WRITING IN THE FILE RESULTS(FILENAME)
400    CALL XMEDIAN(N,XMEDVAL,SIGMA)
410   CALL SPECTRA(N,GZERO,RO,FC,XRMS,MAXDNO,DELTA,TESTRO,
420   & UBAR,SCALE1,SCALE2)
430    ENDFILE "RESULTS"
440   WRITE("RESULTS",621)DISNORM
450   621 FORMAT(" ","                                    X/M=", F6.3//)
460    WRITE("RESULTS",25)XBAR,XMIN,XMAX,C,K,N
470   25FORMAT(4X,6H XBAR=,F8.4,2X,/4X,6H UMIN=,F8.4,2X,5HUMAX=,
480   & F8.4,2X,2HC=,F6.3,2X,2HK=,I6,2X,2HN=,I4,///)
490    DO3 J=1,K; IF(M(J).LE.10)GO TO 21
500    C1=M(J); C2=10.*ALOG(C1)/2.3026; MM(J)=C2; GO TO 130
510    21 MM(J)=M(J)
520   130 CONTINUE; PC(J)=(M(J)*100.)/N; 3 CONTINUE
530   WRITE("RESULTS",76)
```

```
540   76FORMAT(4X,34H PROBABILITY DENSITY FUNCTION     ,//4X,
550   &" ","N      P(U)    U(CM/SEC)  LOG(N)"/)
560    DO 98 J=1,K; P=J;XX=XMIN+C*P
570    L=MM(J)
580    DO 999 I=1,L;999 LINE(I)=PONT
590   98 WRITE("RESULTS",129)M(J),PC(J),XX,(LINE(I),I=1,L)
600   129 FORMAT(I6,2X,F7.2,2X,F8.3,3X,59A1)
610   WRITE("RESULTS",109)XMEDVAL,P0,GZERO,UBAR,XRMS,INTENSITY
620   109 FORMAT(///"    U(MEDIAN)=",F8.4,"  R(0)=",F8.4,"  G(0)=",
630   &F8.4,//4X,6H UBAR=,F8.4,7HCM/SEC,,2X,5HURMS=,F8.4,7HCM/SEC,,
640   & //" ",4X,"TURBULENT INTENSITY=",F8.4,"(X100 PERCENT)",//)
650   WRITE("RESULTS",260)
660   260 FORMAT(" "," T(SEC)     R(T)      RC(T)    F(HZ)     G(F)",//)
670   WRITE("RESULTS",261)R0,GZERO
680   261 FORMAT(" "," 0.000  ",F7.2,"      1.00    0.000",2X,F7.2)
690   & 13H     0.00      ,F10.5,//)
700   WRITE("RESULTS",26)(DEL(I),R(I),RC(I),F(I),G(I),I=1,MAXDNO)
710   26 FORMAT(2X,F6.3,2X,F7.2,2X,F7.2,2X,F6.3,2X,F7.2)
720   WRITE("RESULTS",28)DELTA,TESTRO
730   28 FORMAT(//" ","DELTA=",F6.3,"SEC",/" R(O) COMPUTED FROM SPE"
740   & "CTRUM =",F10.4)
750    & "MAX. DELAY=1SEC",F5.2)
760   WRITE("RESULTS",327)SCALE1,SCALE2
770   327 FORMAT(" ","MICROSCALE=",F7.2,"CM",/"DIFFUSION LENGTH=",
780   & F7.2,"CM"//)
790    STOP; END
800CMEAN VALUE
810    FUNCTION XMEAN(N)
820    COMMON X(1000)
830    XSUM=0
840    DO 10 I=1,N
850    10 XSUM=XSUM+X(I)
860    T=N
870    XMEAN=XSUM/T
880    RETURN;END
890C   PROBABILITY DISTRIBUTION FUNCTION
900    SUBROUTINE PROB(N)
910    COMMON X(1000),XMIN,XMAX,C,K,M(50)
920    K=1.87*N**0.4
930    C=(XMAX-XMIN)/K
940    DO 12 KK=1,N
950    TEMP=(X(KK)-XMIN)/C
960    IF(TEMP.LE.1.0)GO TO 107
970    L=TEMP
980    O=L
990    IF(TEMP-O)21,21,22
1000   21 J=L; GO TO 23
1010   22 J=L+1
1020   23 M(J)=M(J)+1; GO TO 12
1030   107 M(1)=M(1)+1
1040    12 CONTINUE
1050    RETURN ;END
```

```
1060C  MEDIAN
1070   SUBROUTINE XMEDIAN(N,XMEDVAL,SIGMA)
1080   COMMON X(1000),XMIN,XMAX,C,K,M(50)
1090   CALL PROB(N)
1100   SUM=0. ; DO 13 I=1,K
1110   SUM=SUM+M(I)
1120   IF(SUM.GE.N/2) GO TO 19
1130   13 CONTINUE
1140   19 XMEDVAL=XMIN+C*I
1150
1160   RETURN; END
1170   FUNCTION RMS(N)
1180   COMMON X(1000)
1190    SUMSQX=0
1200    DO 7 I=1,N
1210   7 SUMSQX=SUMSQX+X(I)*X(I)
1220
1230   RMS=(SUMSQX/N)**0.5
1240    RETURN;END
1250   SUBROUTINE AUTOCORR(N,R0,XRMS,MAXDN0)
1260   COMMON X(1000),XMIN,XMAX,C,K,M(50),R(50),RC(50)
1270   DO 20 I=1,MAXDN0; PRODX=0.;L=N-I
1280   DO 21 KK=1,L
1290   21 PRODX=PRODX+X(KK)*X(KK+I)
1300   R(I)=PRODX/(N-I)
1310   20 RC(I)=R(I)/R0
1320    RETURN;END
1330   SUBROUTINE SPECTRA(N,GZERO,R0,RC,XRMS,MAXDN0,DELTA,TESTRO,
1340   & UBAR,SCALE1,SCALE2)
1350   COMMON X(1000),XMIN,XMAX,C,K,M(50),R(50),RC(50),
1360   & F(50),G(50),DR(50)
1370   CALL AUTOCORR(N,R0,XRMS,MAXDN0)
1380   R0=0.;A=MAXDN0; LM=MAXDN0-1; LP=MAXDN0+1
1390   DO 46 I=1,MAXDN0; F=I
1400   46 DR(I)=0.5*(1.+COS(3.14159*F/A))
1410   DO 281 J=1,MAXDN0
1420   SUMARG=0.
1430   DO 33 JJ=1,LM
1440   33 SUMARG=SUMARG+DR(JJ)*R(JJ)*COS(3.14159*JJ*J/A)
1450   281 G(J)=2.*DELTA*(R0+2.*SUMARG)
1460   ZSUM=0.; DO 41 I=1,LM;41 ZSUM=ZSUM+DR(I)*R(I)
1470   GZERO=2.*DELTA*(R0+2.*ZSUM)
1480   GK=0.;DO 404 I=1,LM
1490   404 GK= GK+G(I)
1500   TESTRO=(0.5*GZERO+GK+0.5*G(MAXDN0))/(2.*DELTA*A)
1510   SUM=0.; DO 282 I=1,LM
1520   282 SUM=SUM+(F(I)*F(I)*G(I)/R0)
1530   TLAST=F(MAXDN0)*F(MAXDN0)*G(MAXDN0)/R0
1540   FINT=(2.*SUM+TLAST)/(2.*DELTA*A)
1550   SCALE1=(UBAR/(2.*3.14159))*(FINT**(-0.5))
1560   SUMR=0.; DO 283 I=1,LM
```

```
1570   IF(FC(I))430,430,431
1580   430  GO TO 432
1590   431 SUMR=SUMR+FC(I)
1600   283 CONTINUE
1610   432 SCALE2=XRMS*DELTA*0.5*(1.+2.*SUMR)
1620   RETURN;END
```

GLOSSARY OF TERMS AND SYMBOLS

A	angstrom unit
	an empirical constant depending on the shape of the turbulence generating grids
a	a constant
	aperture
a_n	Mie Coefficient
a_R	receiving aperture area
a_T	transmission aperture area
B_s	resolution bandwidth of the power spectrum
b_n	Mie Coefficient
C	a constant
C_l	coherence length of the laser
	capacitance used in the low pass filter of the phase-locked loop
c	velocity of electromagnetic wave in free space
	width of an interval in probability distribution function
D	diameter of the intersection of two incident beams
D_B	blur diameter
D_R	diameter of the receiving aperture
D_T	diameter of the transmission aperture
d	diameter characterizing the sensing volume
d_i	fringe separation
E	a constant
E_i	a constant
E_o	a constant

E_s a constant

e_n noise voltage due to inherent noise in the signal

$e(t)$ output voltage

e_V output voltage for velocity component V

$F(s)$ transfer function of the low pass filter

FM Frequency Modulation

f frequency

f_c center frequency of the Doppler signal

cut-off frequency

f_D Doppler shift

f_i spatial frequency of fringe separation

f_m maximum value of turbulence frequency

maximum value of signal frequency

f_{max} maximum Doppler shift

f_{min} minimum Doppler shift

f_o frequency bias

f_V Doppler frequency spectrum due to fluctuating velocity V

f_1, f_2 focal length of lens L_1, L_2

$G_u(f)$ spectral energy density function of kinetic energy of turbulence

h maximum height of the rays above the optical axis

sampling interval

$h(t)$ impulse response

I_o intensity of the incident beam

I_T intensity of turbulence

$I(\theta)$ intensity of the scattered beam at an angle θ

i_b current in the photomultiplier tube due to stray light noise

i_d dark current in the photomultiplier tube

i_{dc} current in the photomultiplier tube due to shot noise

i_o output current

$\vec{i}_o$ unit vector in the direction of propagation of the incident wave

i_s signal current

$\vec{i}_s$ unit vector in the direction of propagation of the scattered wave

i_1, i_2 Mie scattering function

$J_n(M)$ Bessel function of the first kind and order n and for argument M

K a constant

K_o coagulation rate constant for still air

K_1 sensitivity of the phase comparator

K_2 sensitivity of the voltage controlled oscillator

$\vec{K}_o$ incident wave vector

$\vec{K}_s$ scattered wave vector

k a constant

Boltzman constant

number of class interval in probability distribution function

τ/T_c

k' a constant

L laser cavity length

L_s lateral spherical aberration

L_1, L_2..lenses

ℓ eddy size

length characterizing sensing volume

ℓ_x integral scale of turbulence in x-axis

ℓ_y integral scale of turbulence in y-axis

M mesh size of the grid

modulation index

M(t) modulated carrier in a pulse code modulation

m refractive index (complex)

maximum number of correlation lag values

m_p particle mass

N Avogadro's number

total number of samples

N_c noise power at frequency f_c

N_p number of particles within the sensing volume

NEP noise equivalent power

n a positive integer

index of refraction

sample number

aerosol number concentration per cc

O point of velocity measurement

OS direction of propagation of the scattered wave vector

OX,OY, OZ cartesian coordinates

P_L reference beam power

P_s signal power

P(U) probability distribution function

p position factor in aberration

angular frequency

p(u) probability density function

Q_s Figure of merit of a heterodyning system calculated for a scattered light intensity of s watts per square centimeter per second at a unit distance from the scattering center

q electronic charge

shape factor in aberration

R correlation function

distance between the sensing volume and the receiving aperture

gas constant

Re Reynolds number

R_L load resistor

$R_{\ell x}$ Reynolds number of turbulence in the x-axis

$R_{\ell y}$ Reynolds number of turbulence in the y-axis

R_x velocity correlation between the values of u measured at two points in the x-axis separated by x

R_y velocity correlation between the values of u measured at two points in the y-axis separated by y

$R(\tau)$ auto-correlation function

$R_n(\tau)$ normalized auto-correlation coefficient

R_1 resistance used in the low pass filter of the phase-locked loop

r lag number

radius of curvature of the lens

distance between the point of velocity measurement and the center of the surface scattering disk

r_p particle radius

S location of the receiving aperture

Laplace operator

S_c power of the carrier signal at f_c

S_p image distance for paraxial rays

SNR	signal-to-noise ratio
s	stop distance
T	time period
	absolute temperature
T_c	repitition time
TO	direction of propagation of the incident wave vector
t	time
	decay time
U	velocity component in the x-axis
$\overline{U}$	average velocity in the x-axis
u	fluctuating velocity component
u'	root mean square velocity
u_s'	velocity fluctuation associated with the microscale of turbulence
V	velocity
	volume of intersection of two beams
	velocity component in the y-axis
V_{max}	maximum velocity
V_p	instantaneous particle velocity
	velocity at the point of measurement in the wind tunnel
$\overline{V}$	average velocity in the y-axis
VCO	voltage controlled oscillator
v	fluctuating velocity component
v'	rms velocity
v_B	most probable velocity of the particle due to Brownian motion
v_o	maximum amplitude of the fluctuating velocity component

W	velocity component in the z-axis
$\overline{W}$	mean velocity in the z-axis
w	fluctuating velocity component
w'	root mean square velocity
x	distance along the longitudinal axis (channel axis)
	distance between the point of measurement and the turbulence generating grid
y	distance along the transverse axis, perpendicular to the channel axis
	object distance
y'	image distance
z	a constant
	distance along the z-axis (optical axis)
α	convergence angle of the focused incident beam
α_1	optimum value of the convergence angle for an angle θ
α_p	particle size parameter
β	modulation index
	a simplifying substitution for $(\theta - \phi)$
	angle between the zero and first order of diffraction
$\Delta\theta$	angle subtended by the receiving aperture at the point of measurement
$\Delta\phi$	solid angle subtended by the transmission aperture at the point of measurement
$\Delta\Omega$	solid angle subtended by the receiving aperture at the point of measurement
Δf	frequency deviation
	bandwidth

ΔL path length difference between the two incident beams

$\overline{\Delta x^2}$ mean square Brownian displacement

δf instrumental frequency broadening

δf_a instrumental frequency broadening arising from the finite size of the receiving aperture

δf_s instrumental frequency broadening due to the finite size of the sensing volume

δf_T instrumental frequency broadening due to the finite lifetime of the Doppler signal

ε detector quantum efficiency

η heterodyning efficiency

θ scattering angle

angle between the two incident beams of a symmetrical heterodyning system

λ microscale of turbulence

wavelength of light

λ_o wavelength of the incident wave

λ_s wavelength of the scattered wave

μ gain

ν_o frequency of the incident wave

ν_s frequency of the scattered wave

ξ spatial displacement in the x-axis

a dummy variable

ρ density

σ conductivity

τ time

time delay

T Doppler signal lifetime

ϕ angle between the forward direction of the incident wave vector and the direction of particle velocity

$\phi(t)$ phase angle

ψ angle between the incident and the scattered wave vectors

ω angular frequency

angular velocity

ω_r repitition frequency

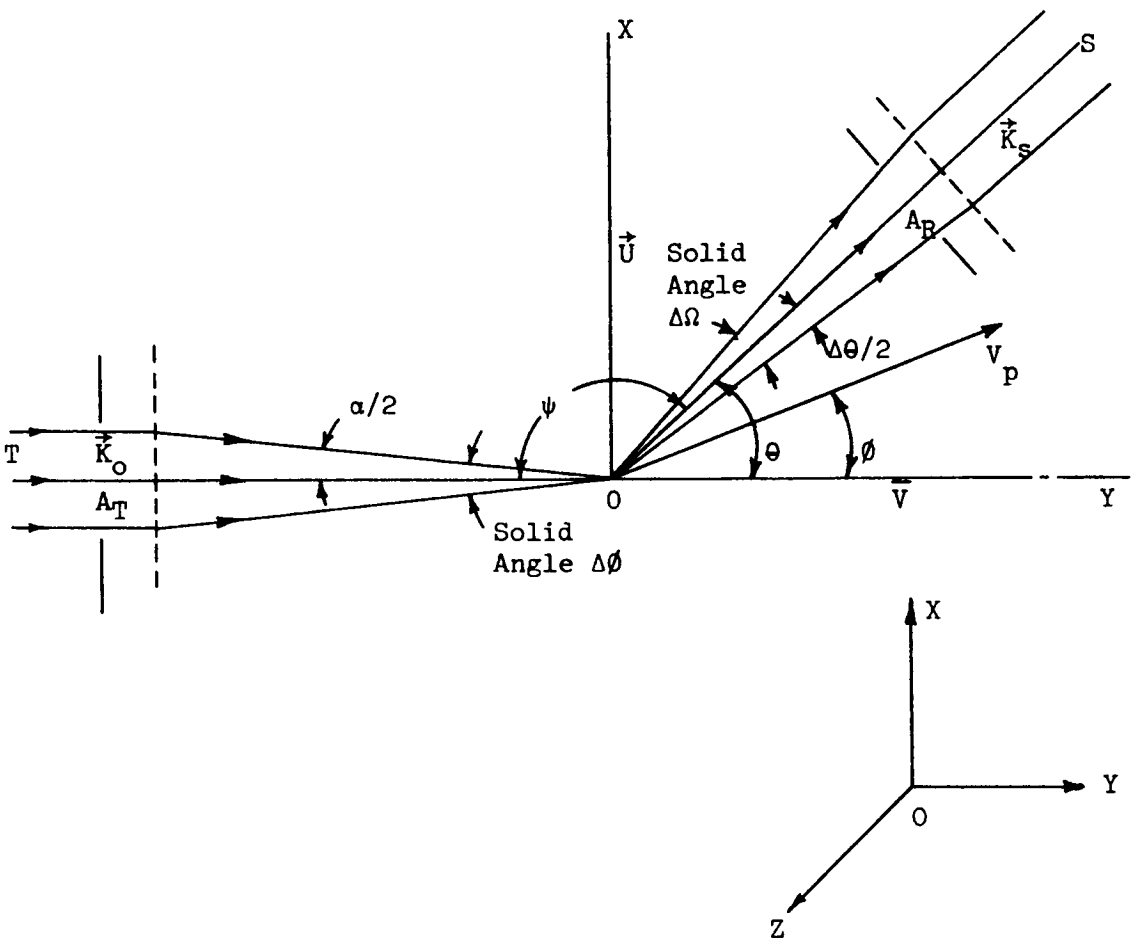

Figure 1

Incident and Scattered Beam Geometry in a Laser Doppler Velocity Meter

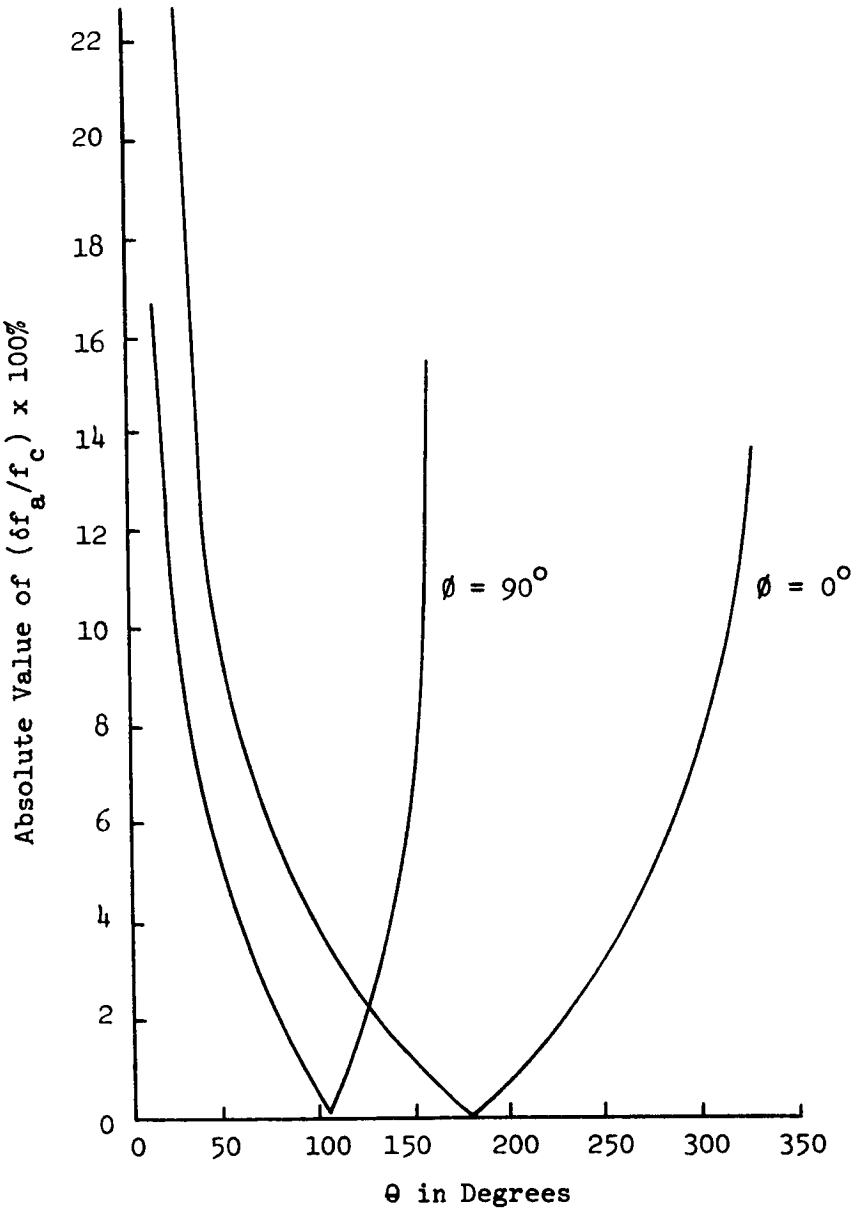

Figure 2

Nature of Variation of $\delta f_a/f_c$ as a Function of θ Plotted for Different Values of Ø in the Local Oscillator Heterodyning System

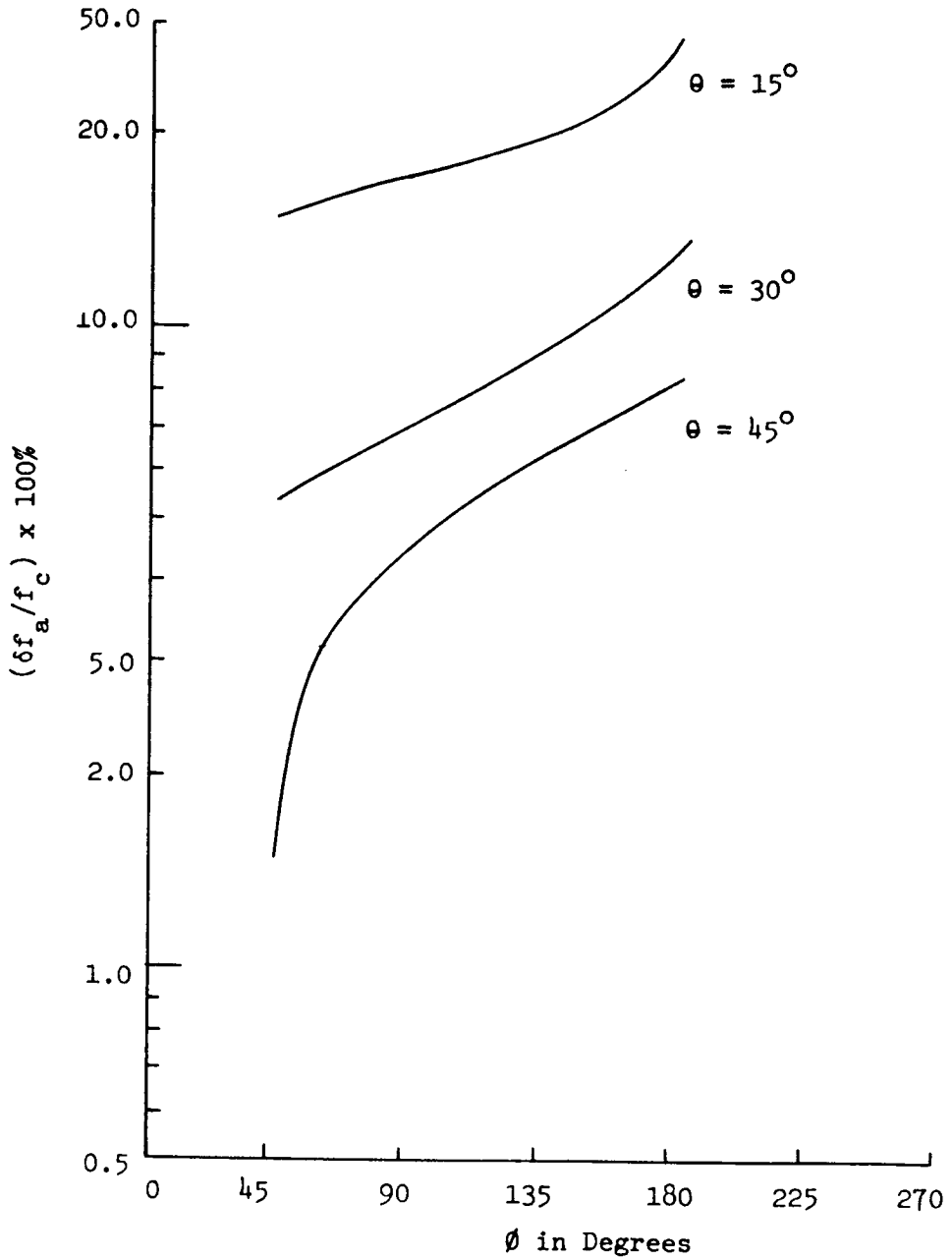

Figure 3

Nature of Variation of $\delta f_a/f_c$ as a Function of Ø Plotted for Different Values of θ in the Local Oscillator Heterodyning System

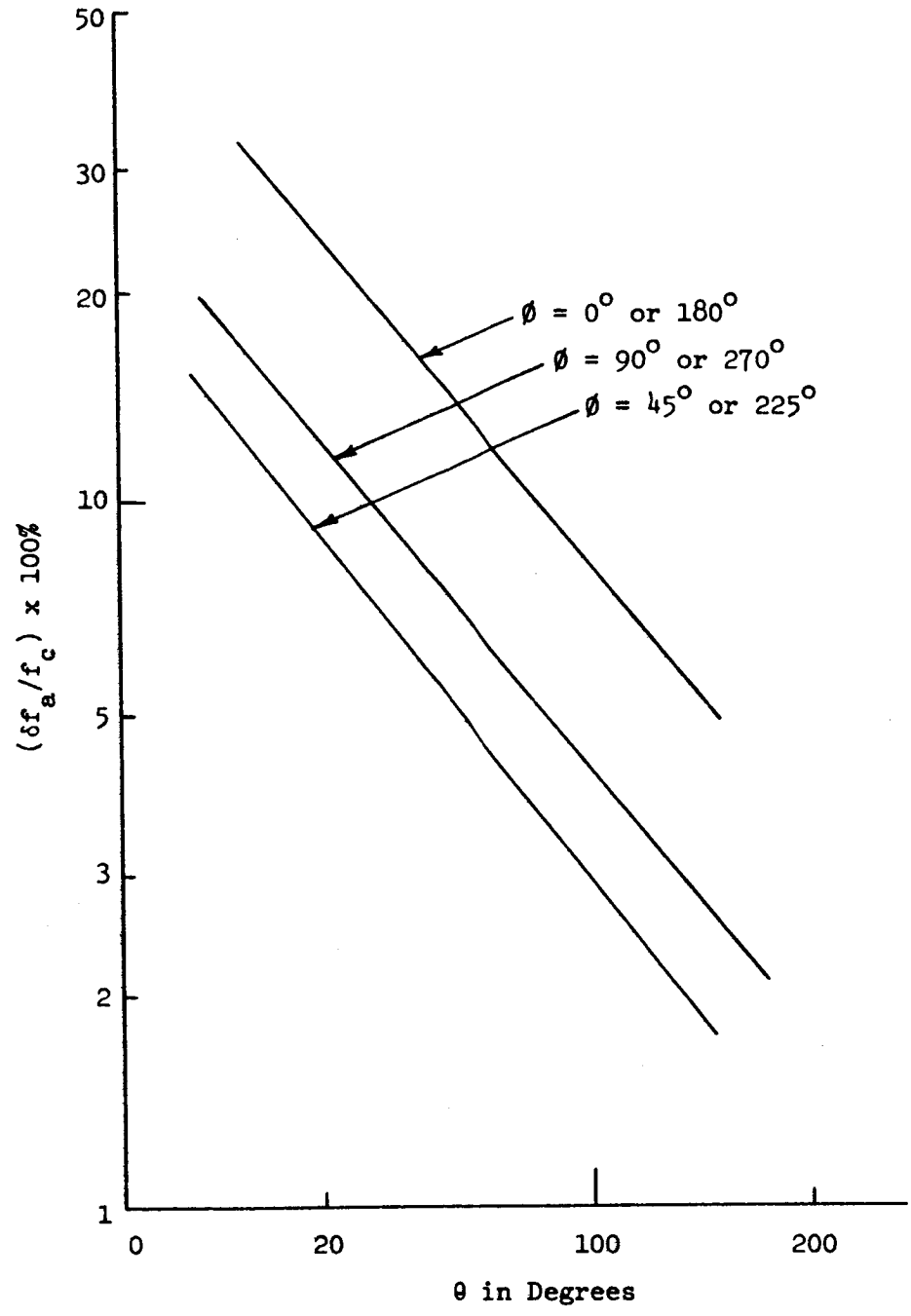

Figure 4

$\delta f_a/f_c$ Versus θ for Different Values of ϕ in the Region of Practical Interest. (Local Oscillator Heterodyning System)

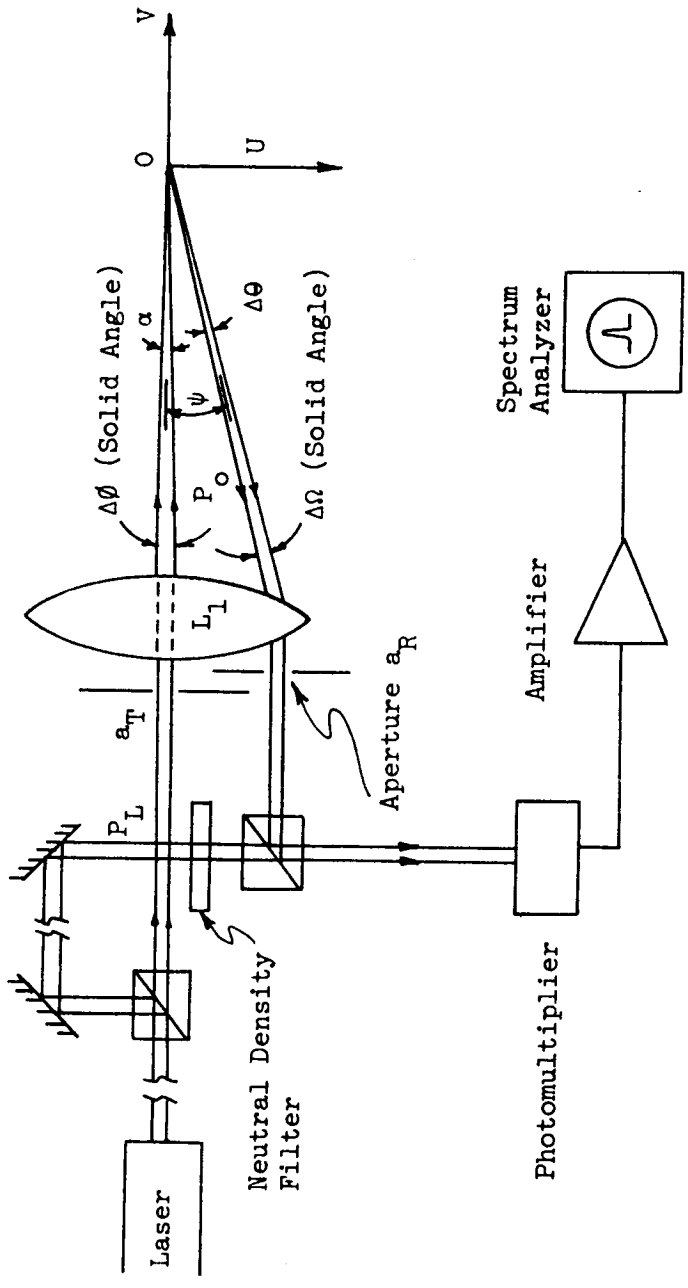

Figure 5

Schematic Diagram of the Local Oscillator Heterodyning System

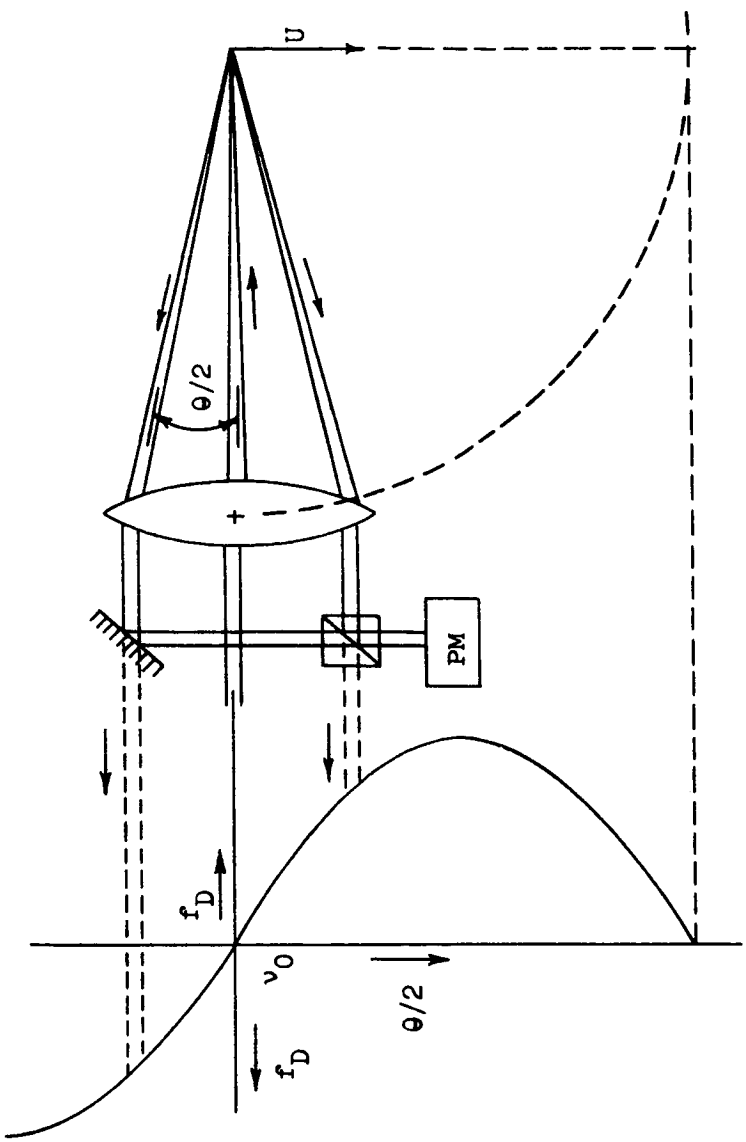

Figure 6

Beam Geometry for the Elimination of Aperture Broadening by Superposition of Two Symmetrically Located Scattered Beams

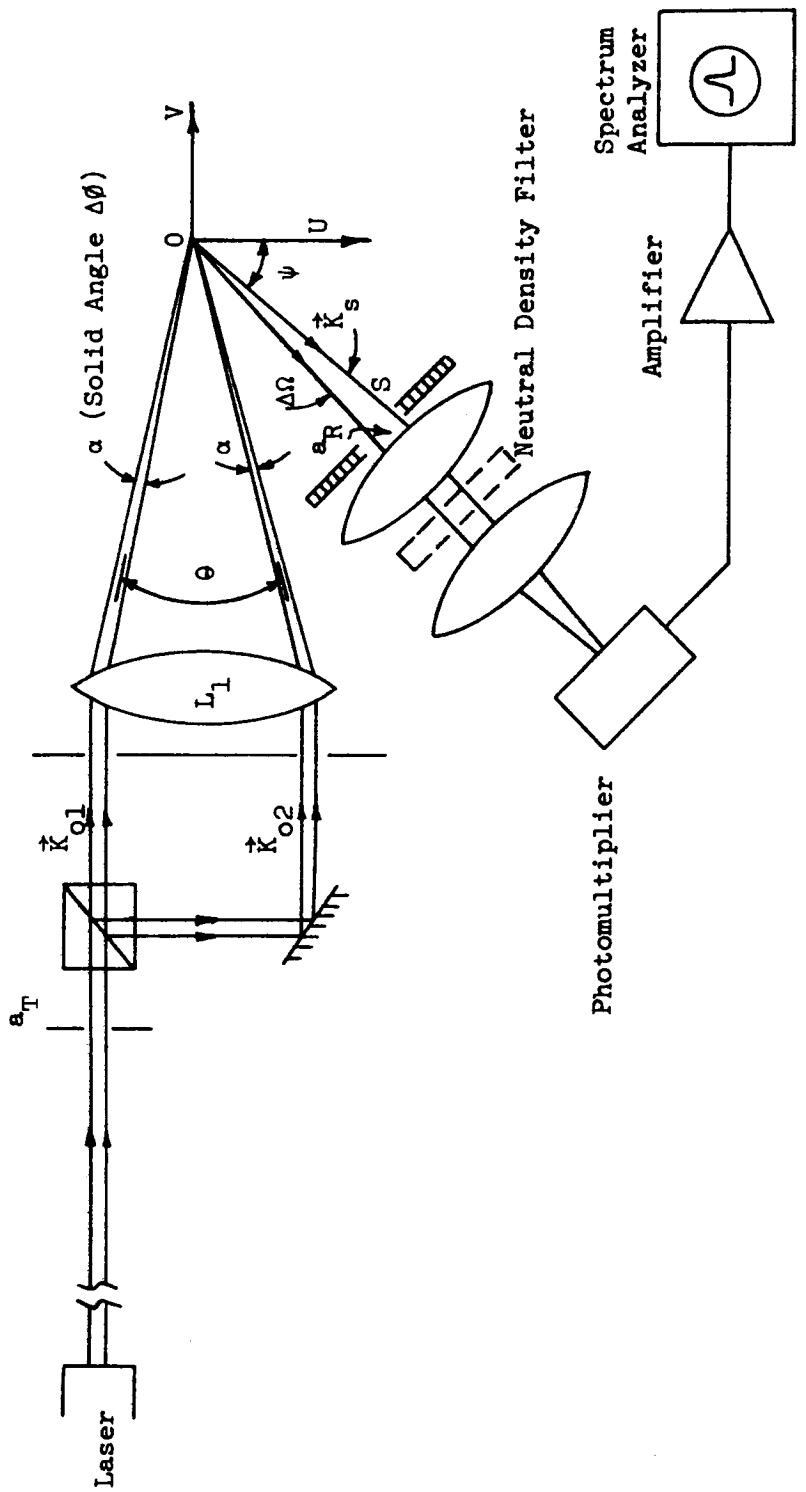

Figure 7

Schematic Diagram of the Symmetrical Heterodyning System

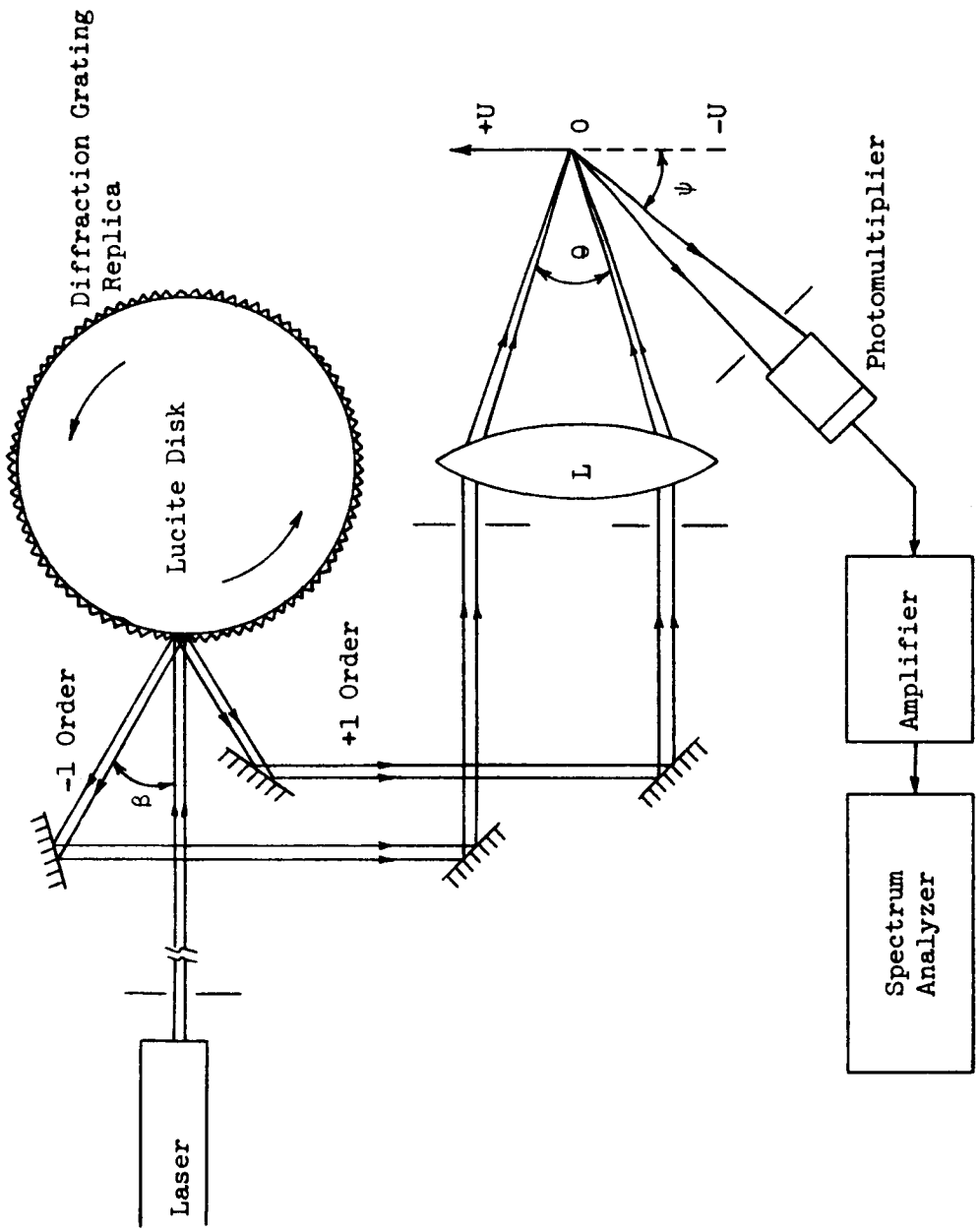

Figure 8

An Experimental Arrangement for Directionally Sensitive Velocity Measurement Employing a Rotating Diffraction Grating

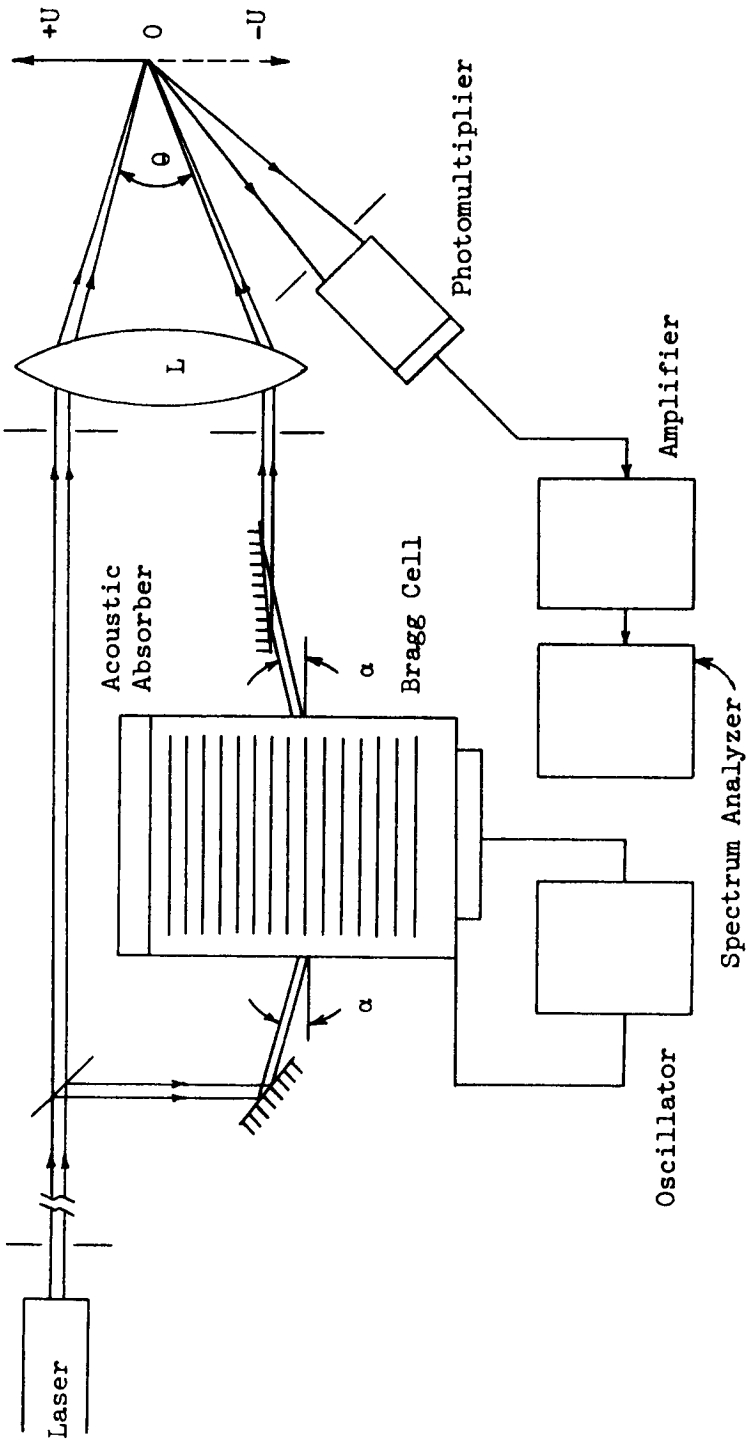

Figure 9

An Experimental Arrangement for Frequency Shifting Using a Bragg Cell

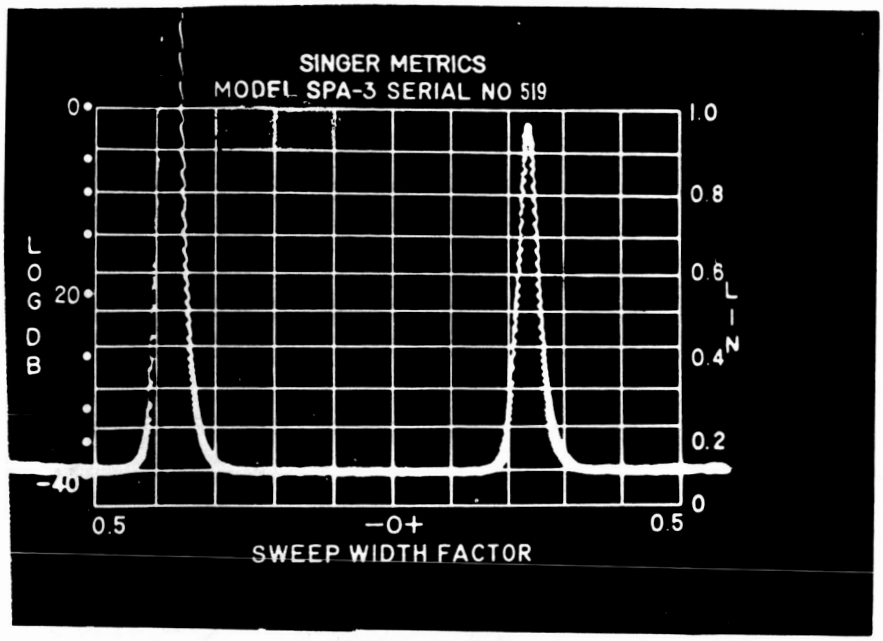

Figure 10a

A Typical Doppler Spectrum from a Constant Velocity (Laminar Flow) Showing the Instrumental Spread (f_c = 600 kHz, sweep width 100 kHz/div. The peak at the left is the zero frequency pip of the spectrum analyzer)

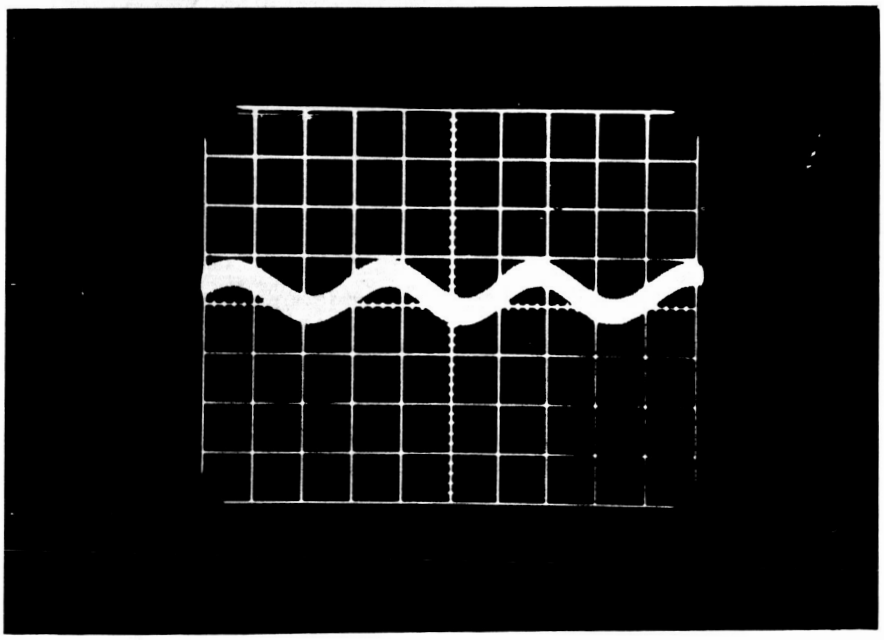

Figure 10b

An Oscillograph of the Same Doppler Signal (f_c = 600 kHz, sweep time: 0.5 microsec/cm. The finite width of the waveform shows the frequency spread)

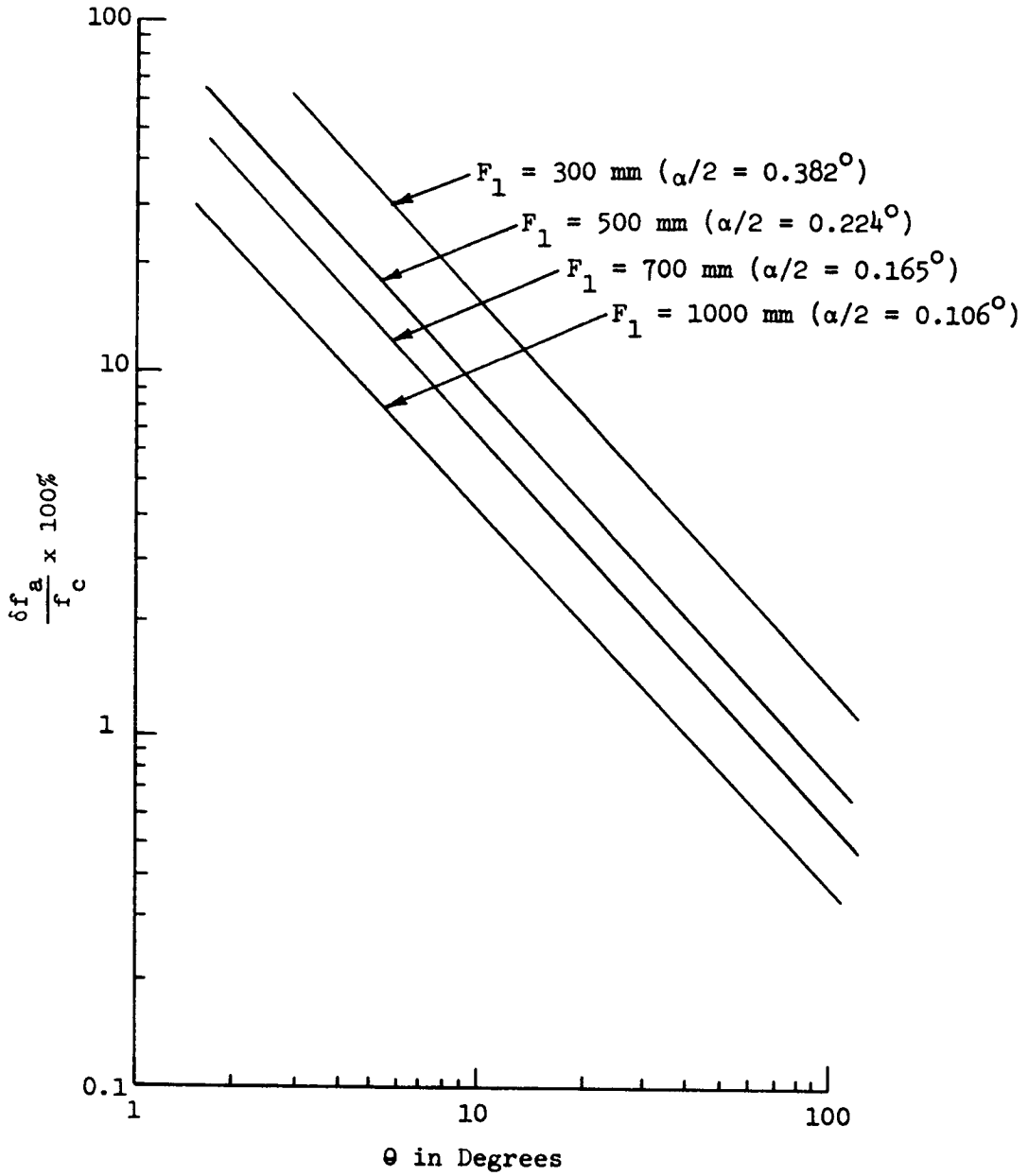

Figure 11

$\delta f_a/f_c$ Versus Θ for Different Values of α
for the Symmetrical Heterodyning System

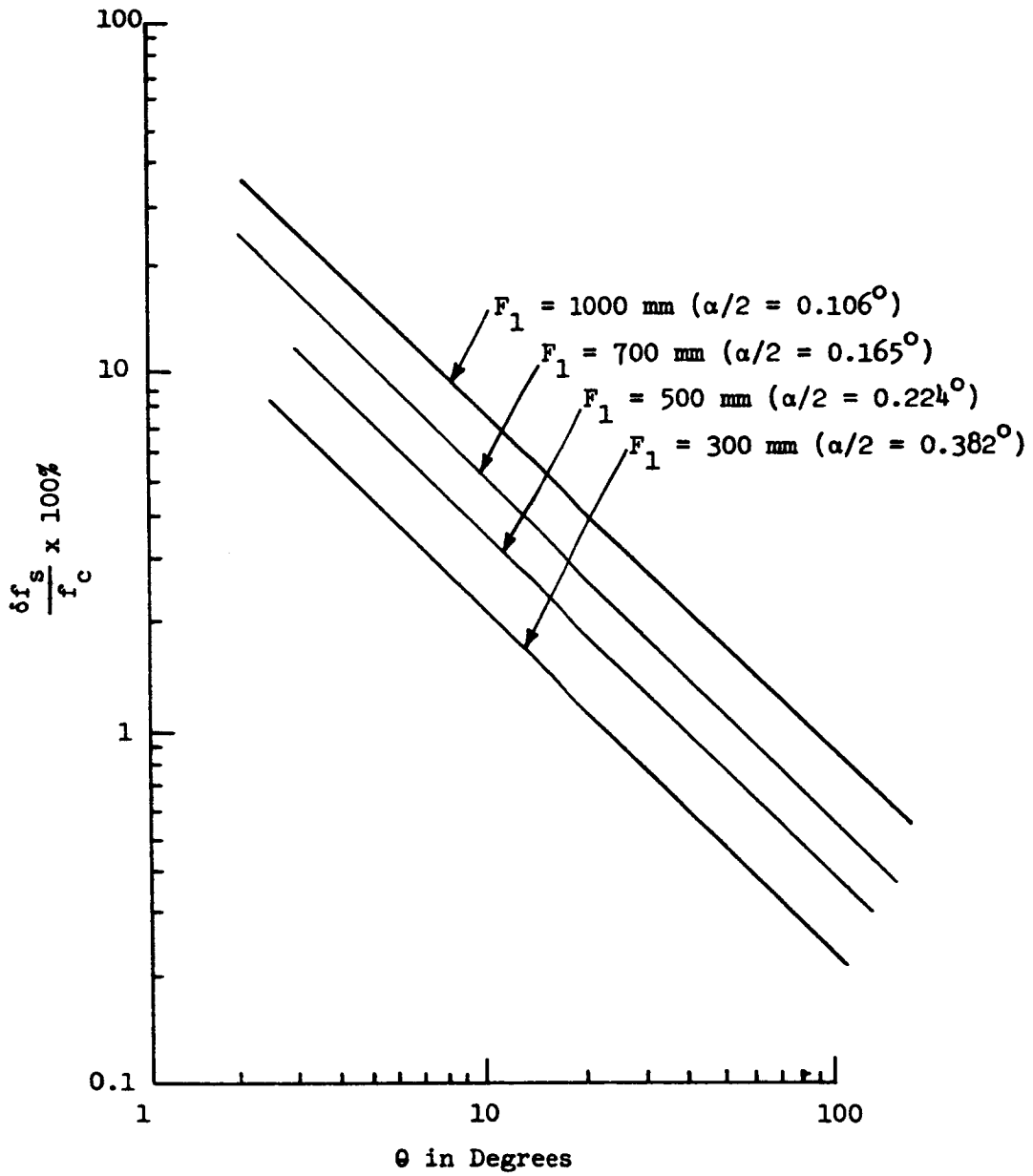

Figure 12

Variation of $\delta f_s/f_c$ as a Function of θ Plotted for Different Values of α and for a Spatial Velocity Gradient of u' = 500 sec^{-1} in the Lateral Axis (Symmetrical Heterodyning System)

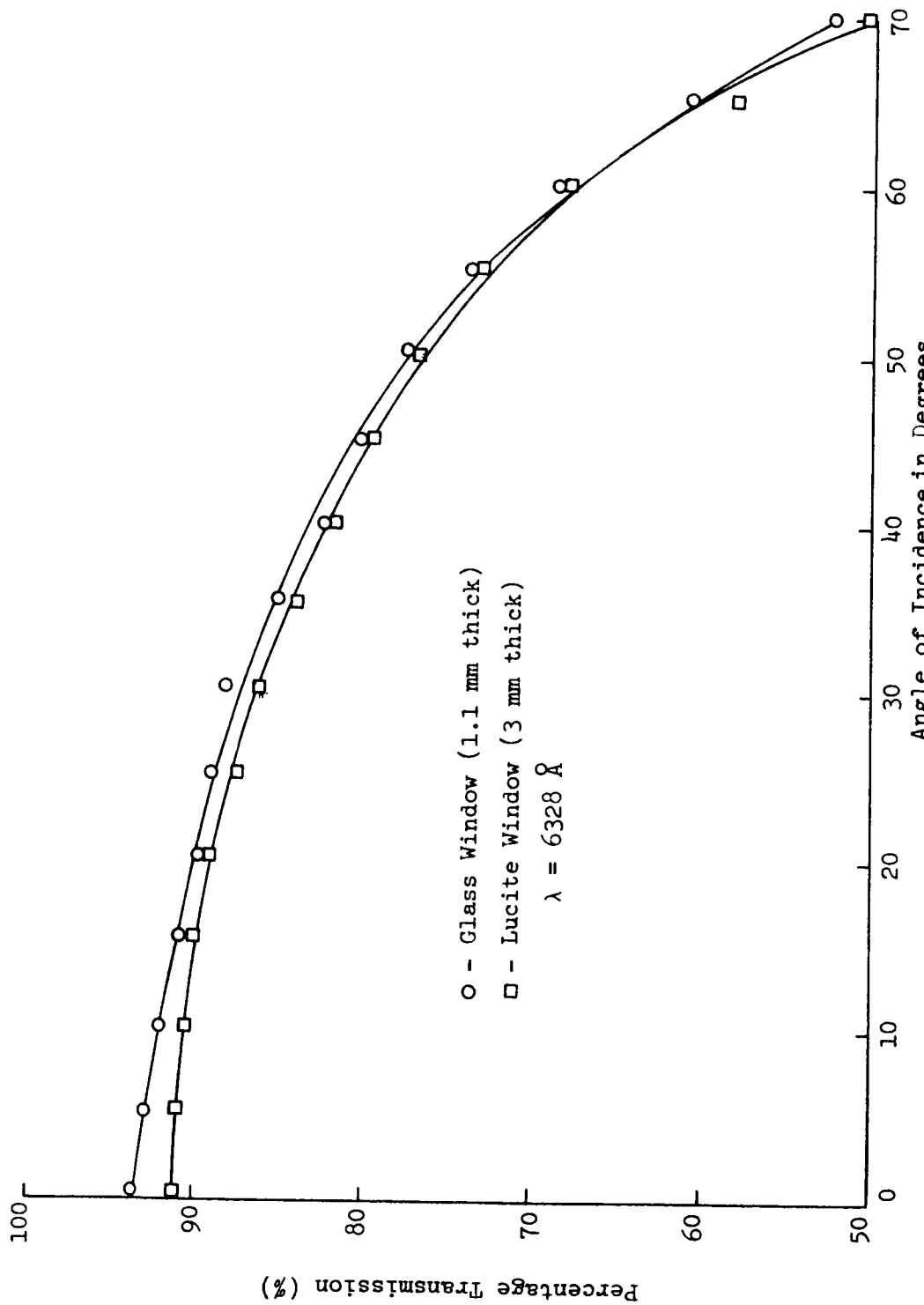

Figure 13

Percentage Transmission Versus the Angle of Incidence for Glass and Lucite Optical Windows

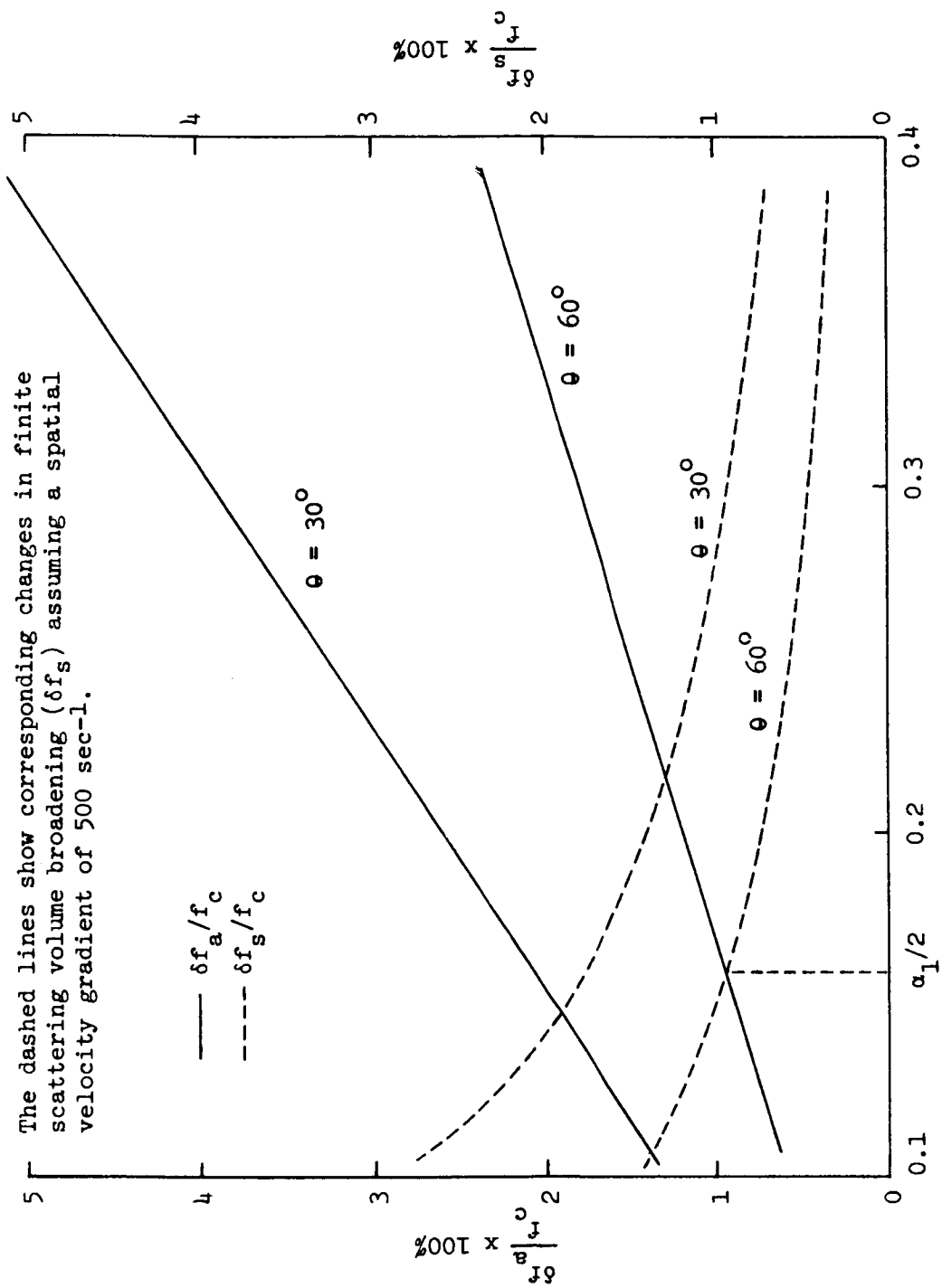

Figure 14

Variation of $\delta f_a/f_c$ and $\delta f_s/f_c$ With α for Different Values of θ
(Symmetrical Heterodyning System)

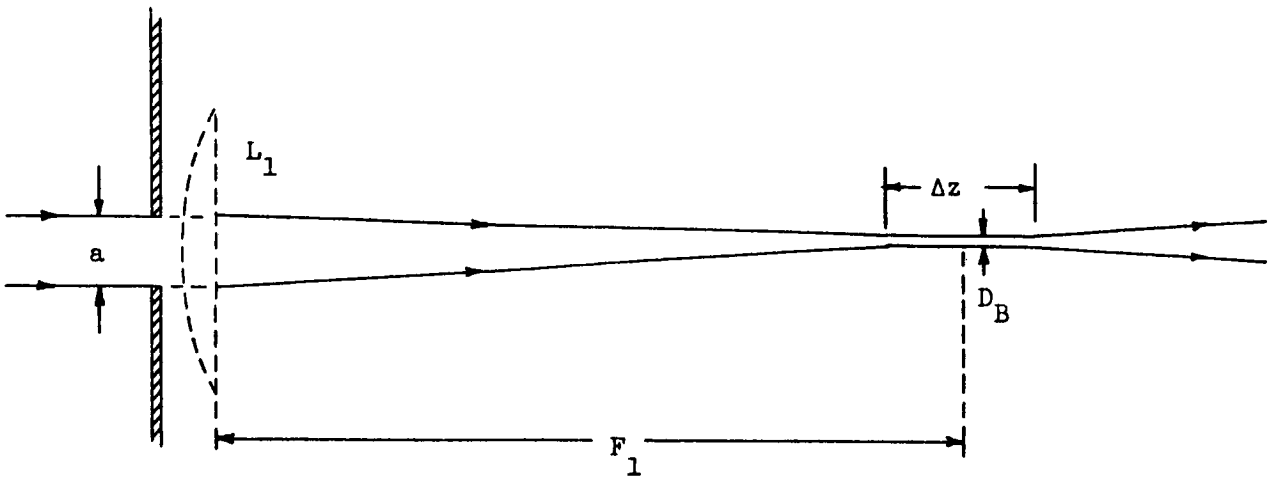

Focal Tolerance in Transmission Optics (see Figure 18)

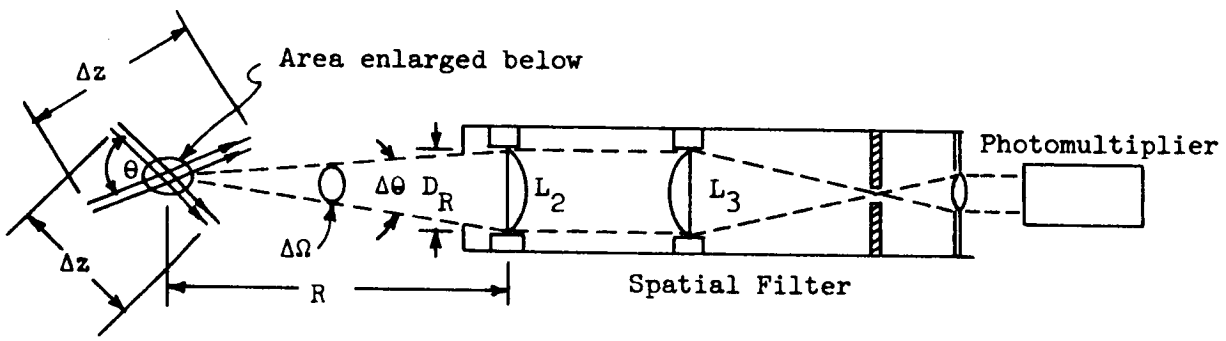

Receiving Optics

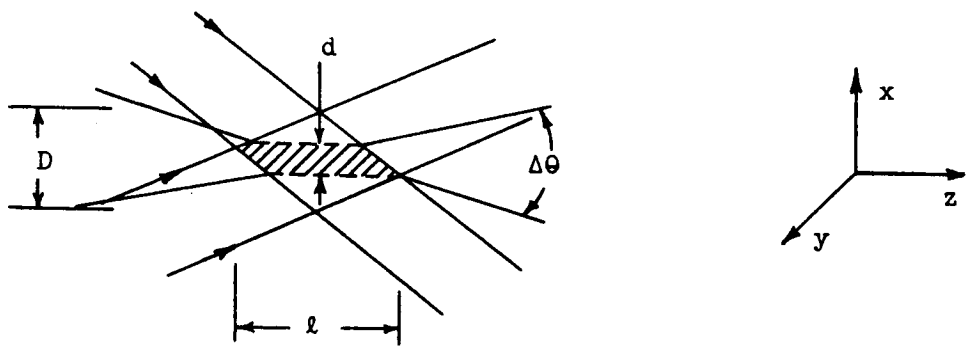

Sensitive Scattering Zone

Figure 15

Dependence of the Geometry of Transmission and Receiving Optics on the Size of the Effective Sensing Volume of the Symmetrical Laser Doppler Velocity Meter

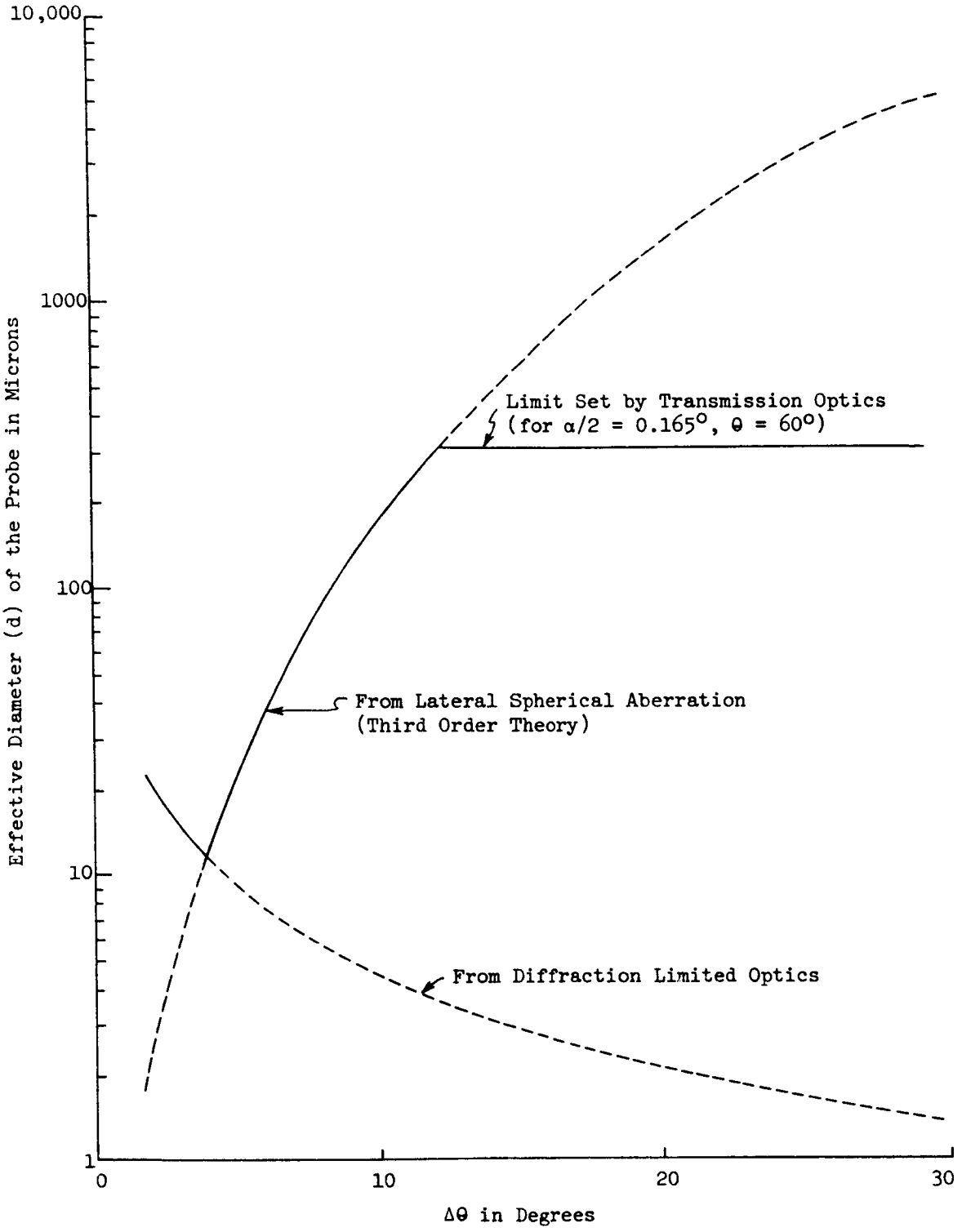

Figure 16

Variation of the Diameter d of the Sensing Volume (Laser Beam "Probe") Versus the Angle $\Delta\theta$ (Symmetrical Heterodyning System)

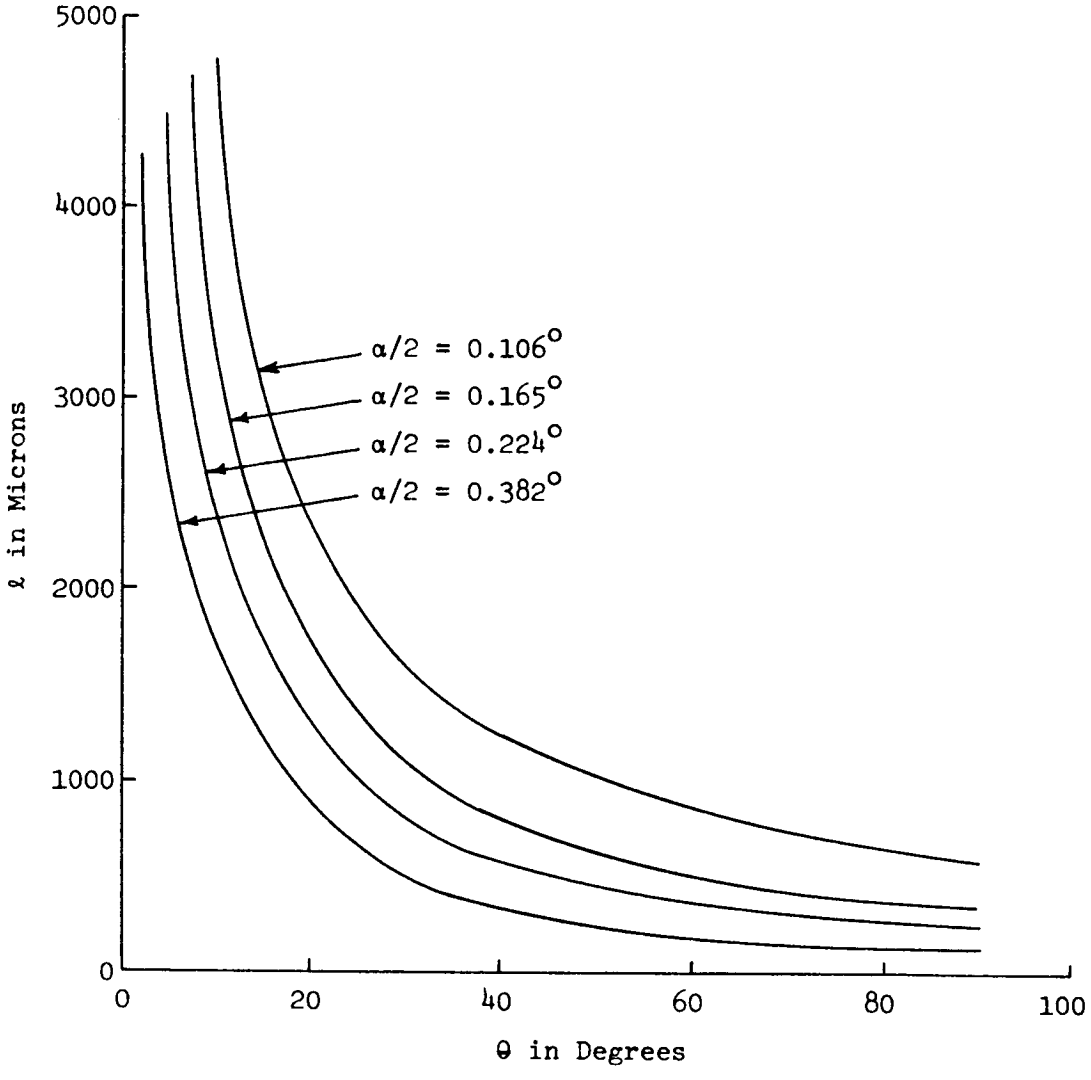

Figure 17

Variation of the Length ℓ of the Sensing Volume Versus θ for Different Values of α/2. (Symmetrical Heterodyning System)

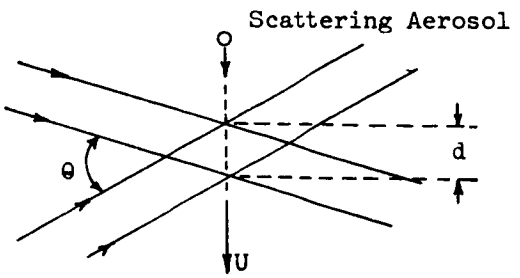

(a) Optical arrangement for $\alpha = 0$

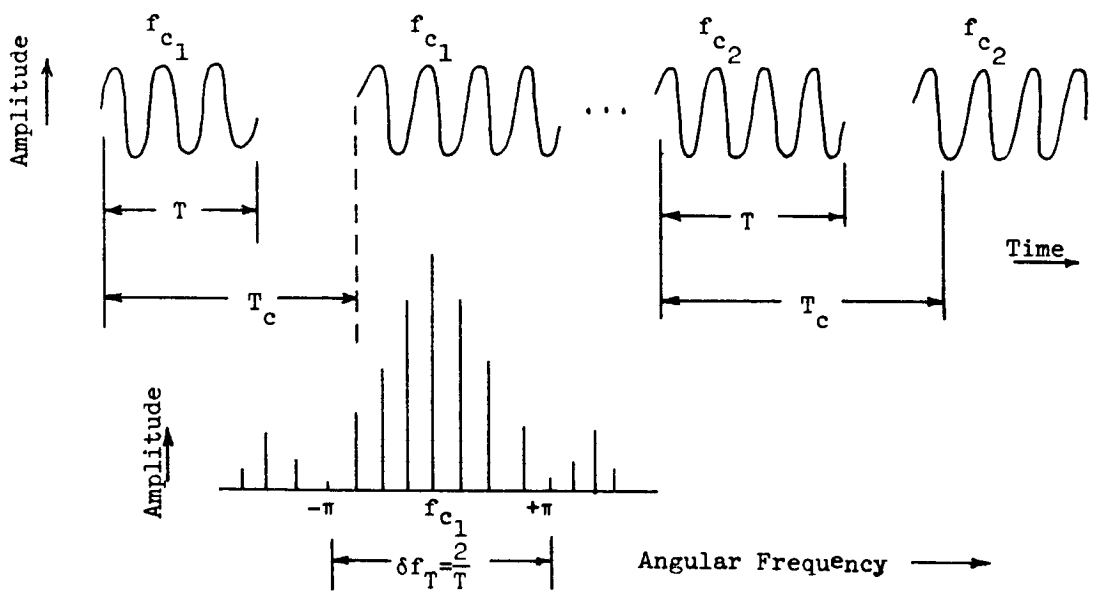

(b) Signal in time and frequency domain

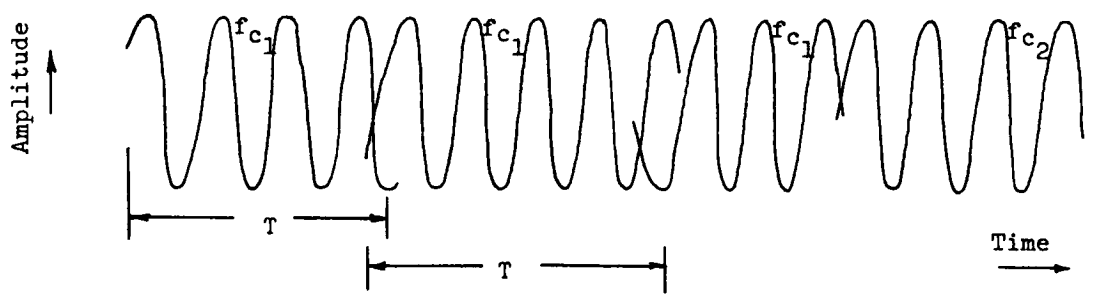

(c) Signal with higher aerosol concentration

Figure 18

Nature of the Doppler Signal in Time and Frequency Domain With Finite Signal Lifetime T. (δf_a and δf_s are assumed 0, $\delta f_T \neq 0$)

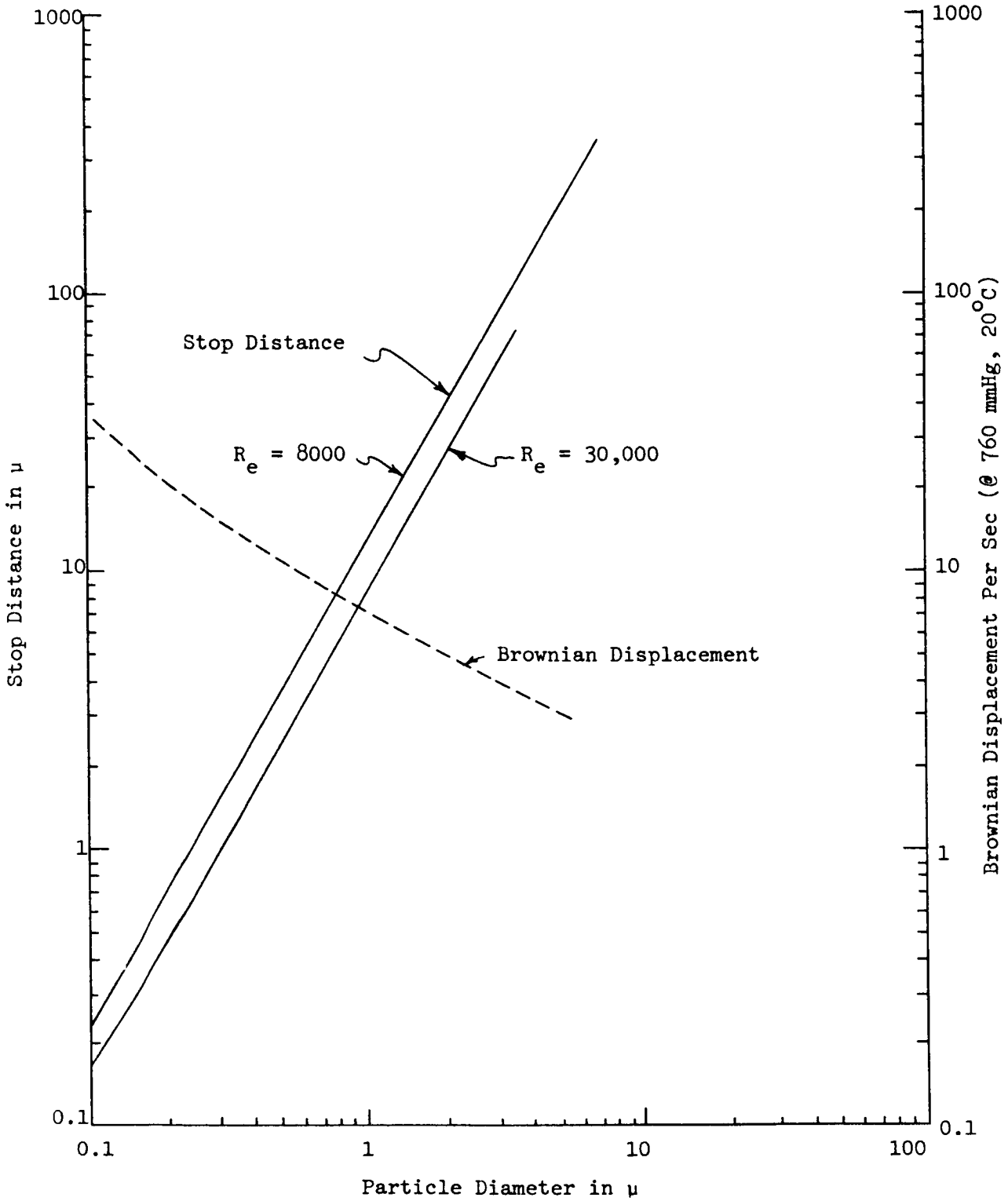

Figure 19

Stop Distance and Brownian Displacement for Unit Density Spherical Particles Versus Particle Diameter

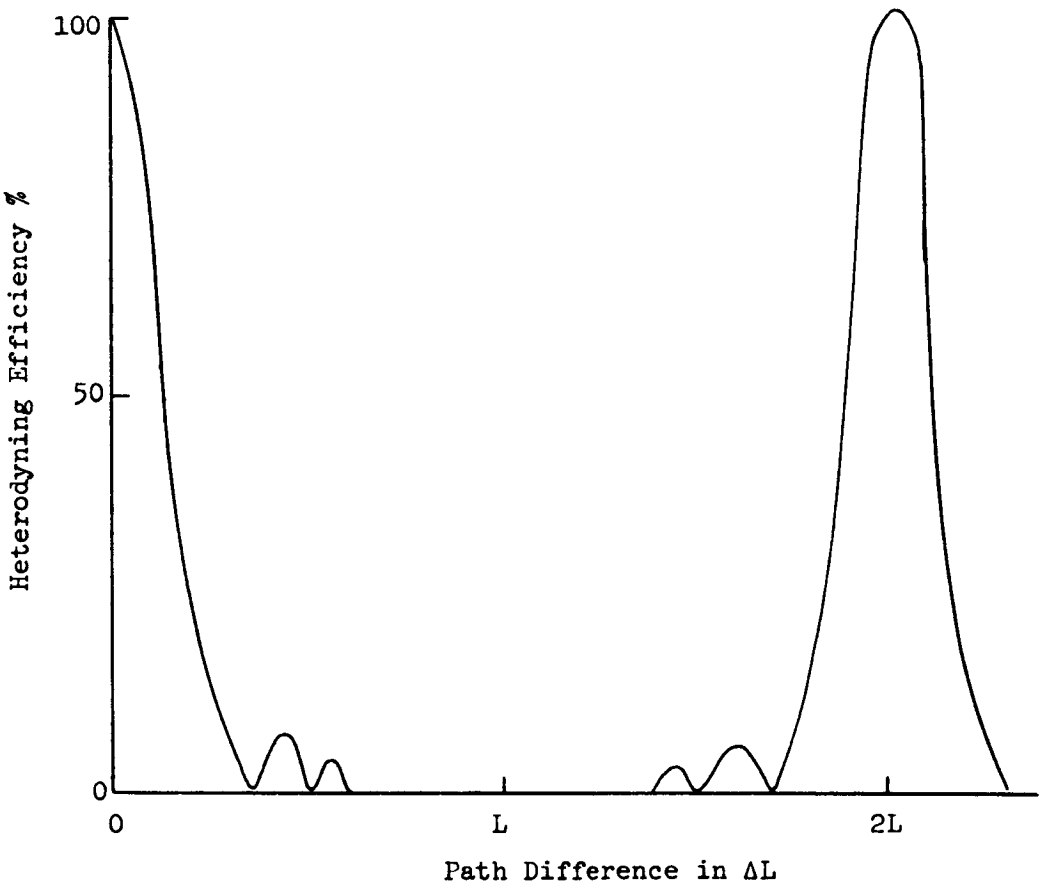

Figure 20

Effect of Path Difference (ΔL) on Heterodyning Efficiency in Terms of the Laser Cavity Length L. (L = 180 cm for Spectra Physics Model 125 Laser).

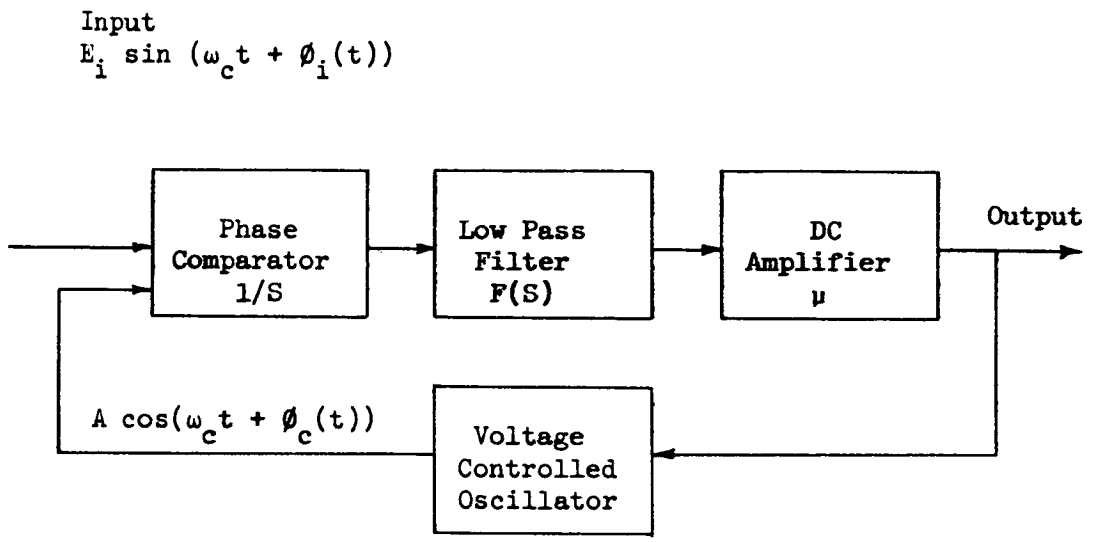

Figure 21

Block Diagram of the Phase-Locked Loop Detector

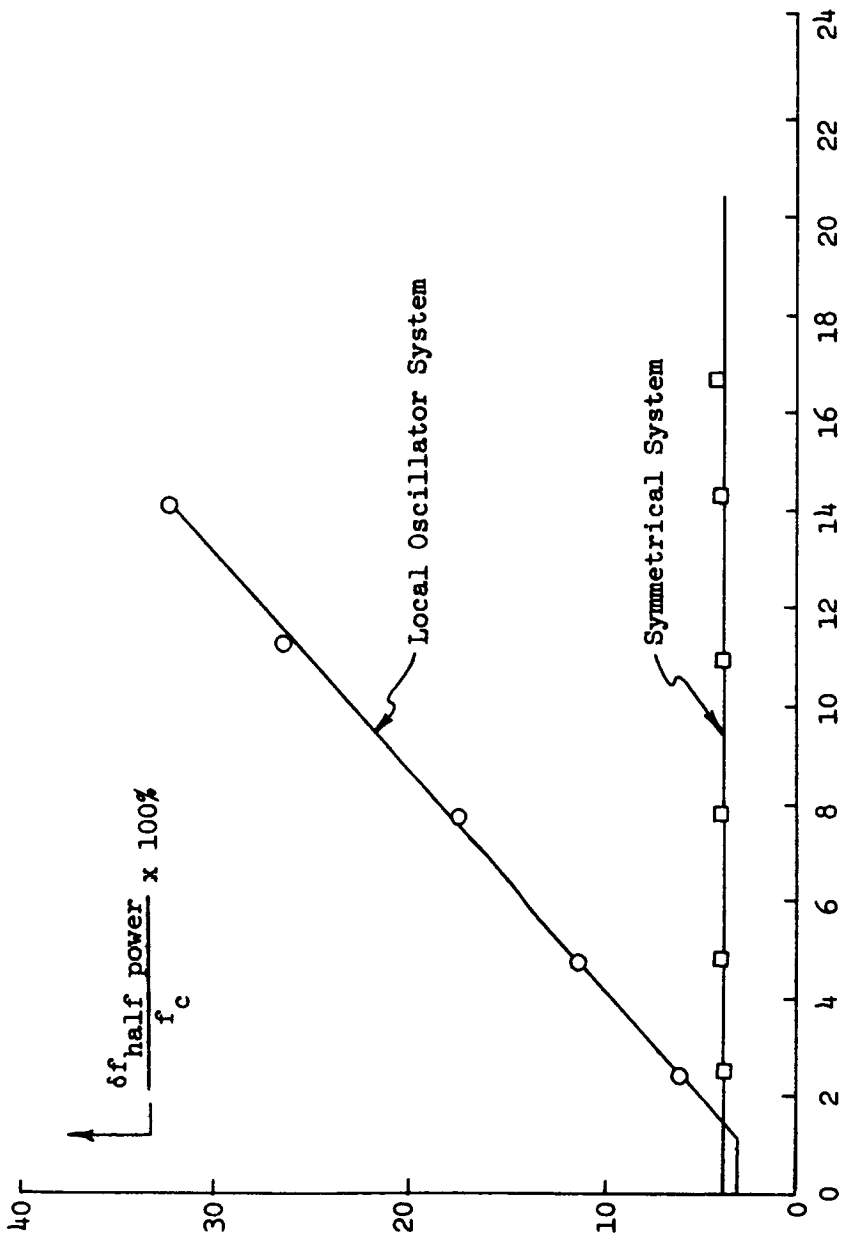

Figure 22

Instrumental Frequency Broadening (δf) Versus Receiving Aperture Diameter

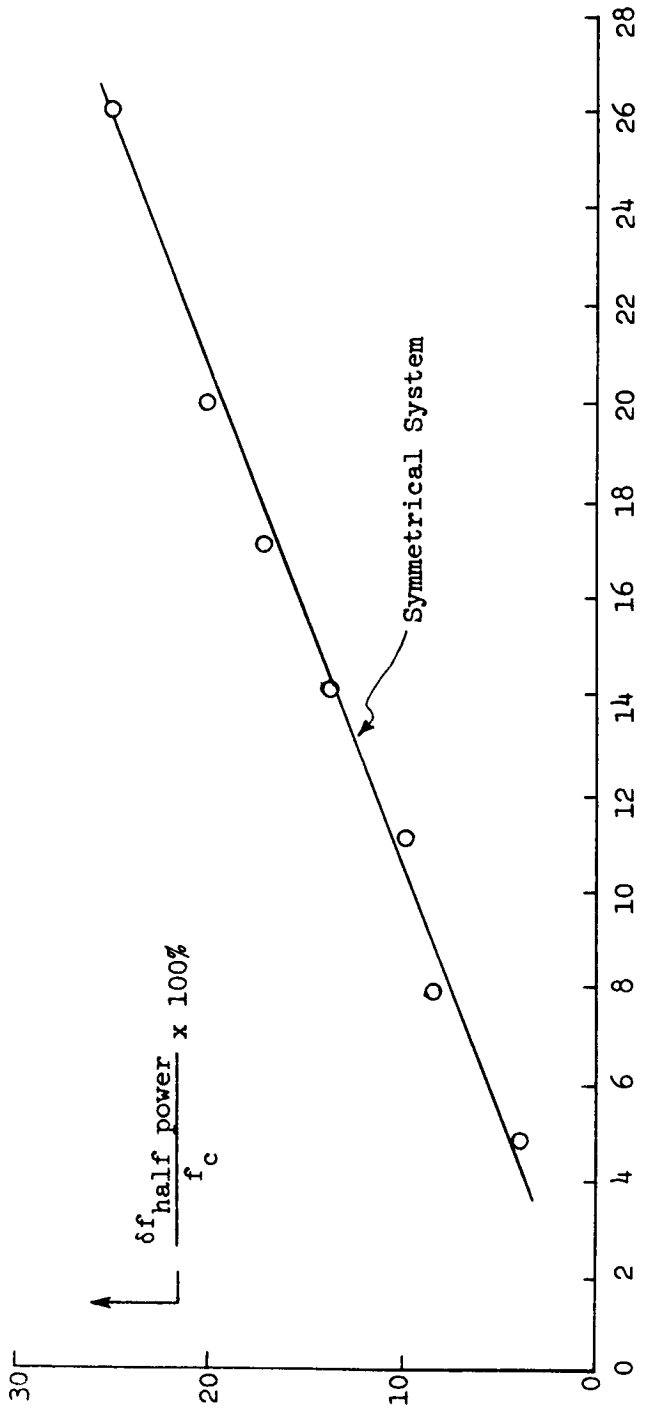

Figure 23

Instrumental Frequency Broadening (δf) Versus Transmission Aperture Diameter

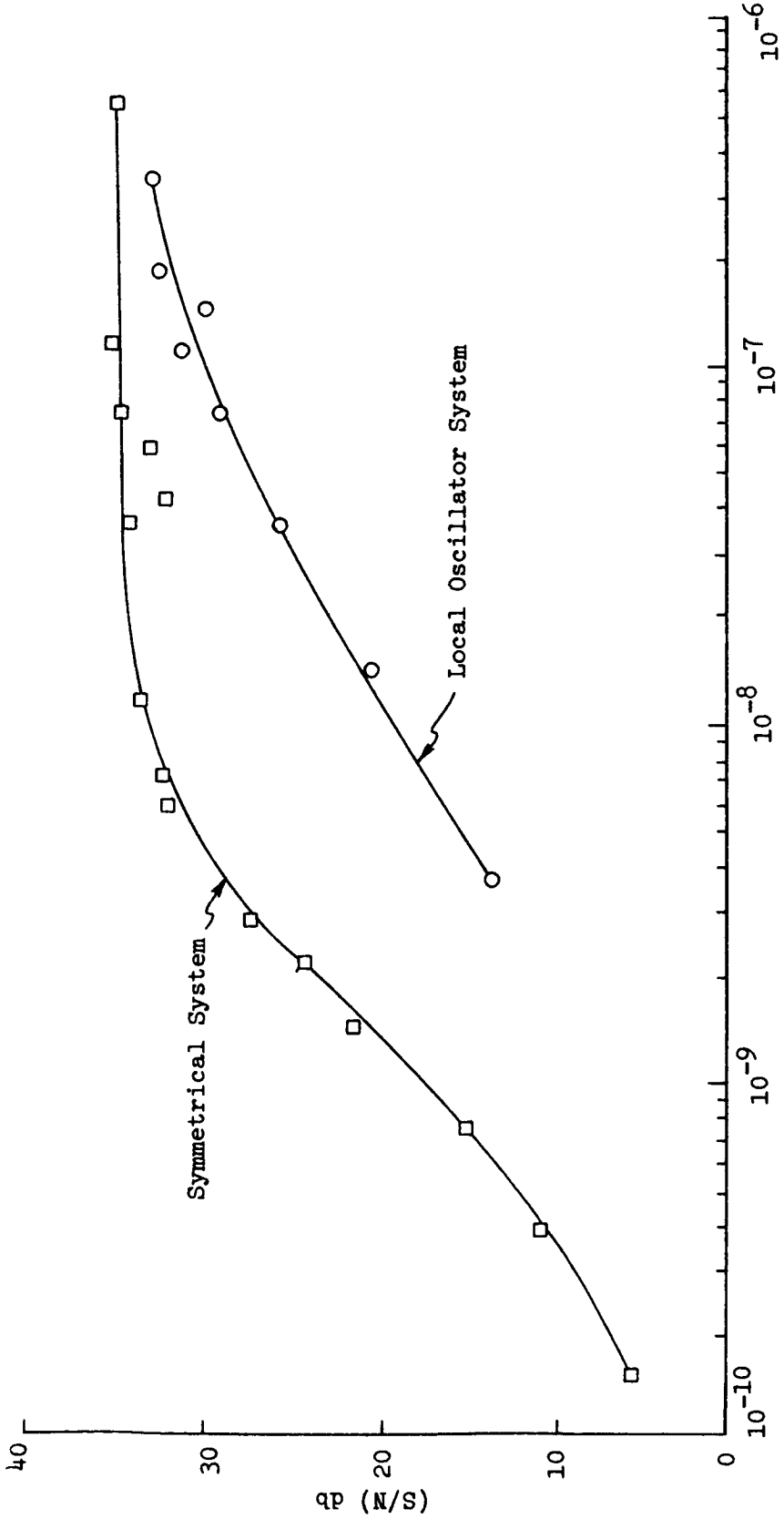

Figure 24

Signal-to-Noise Ratio Versus Signal Power for the Two Different Heterodyning Methods

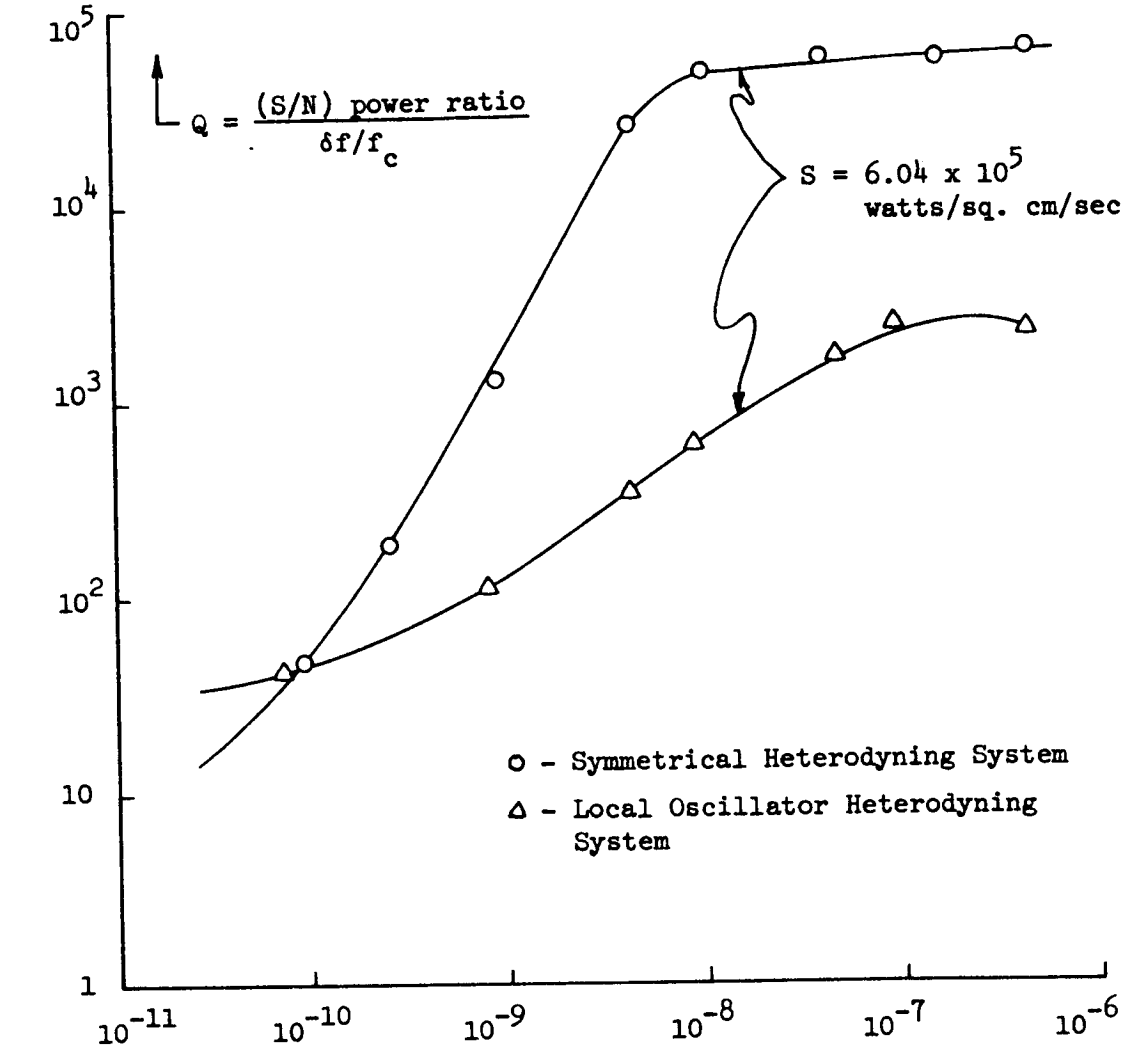

Figure 25

Figure of Merit of Two Heterodyning Systems Versus P_s

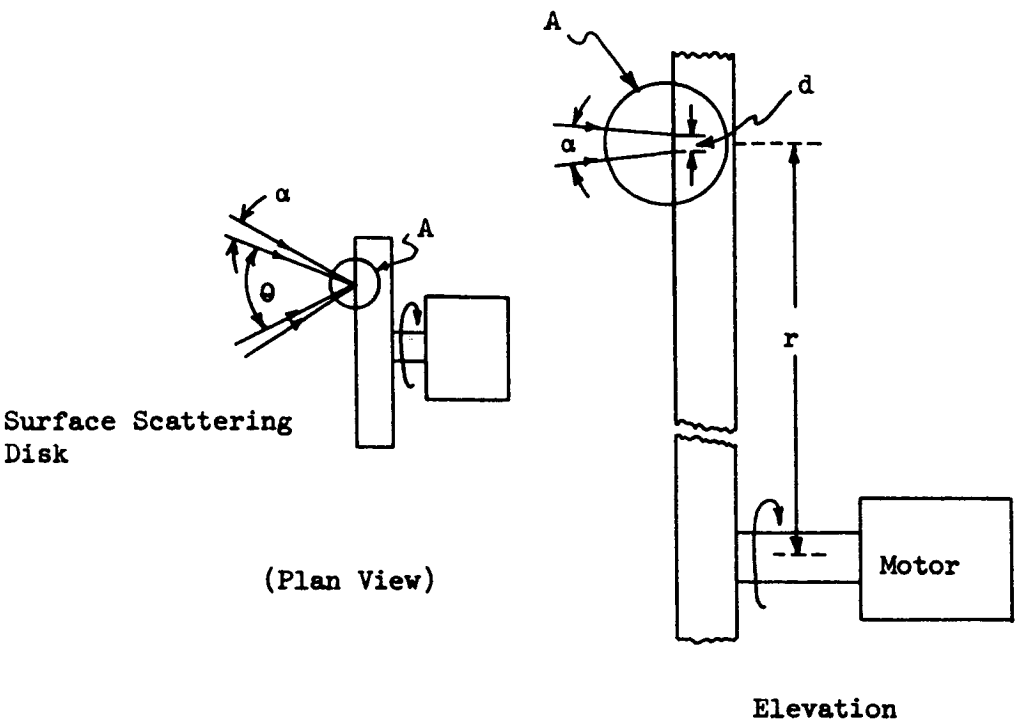

Figure 26

An Experimental Arrangement With a Fixed Velocity Gradient Present Within the Sensing Volume. The Velocity Gradient Is Along the Diameter d of the Sensing Volume.

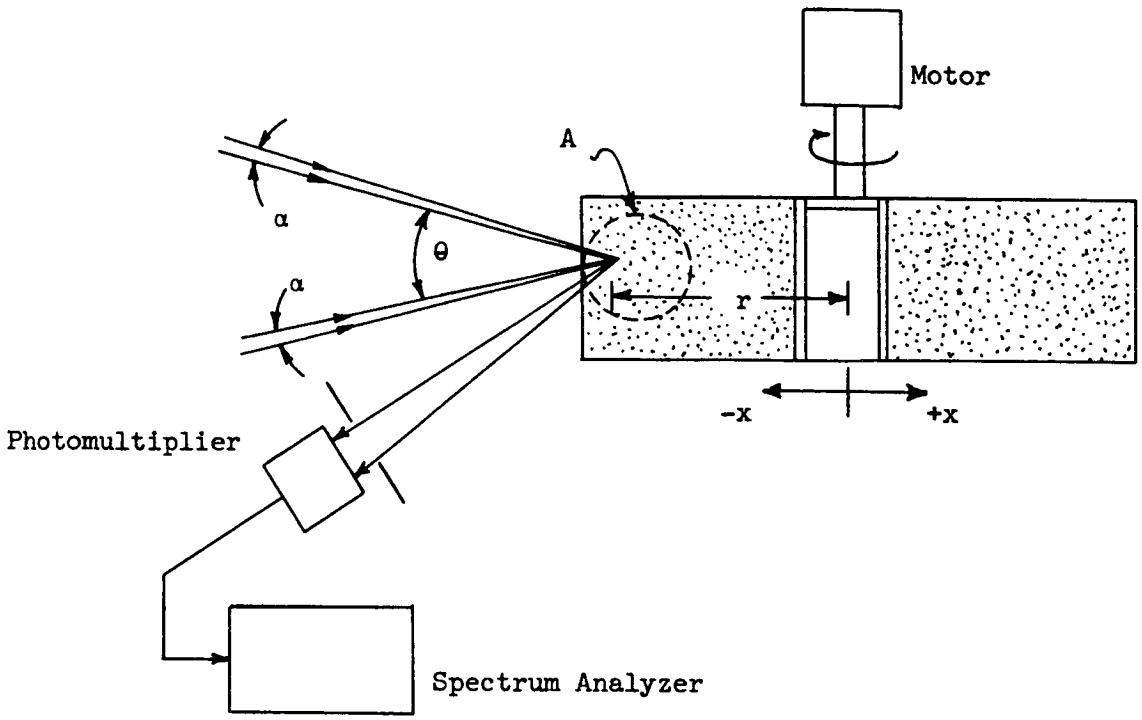

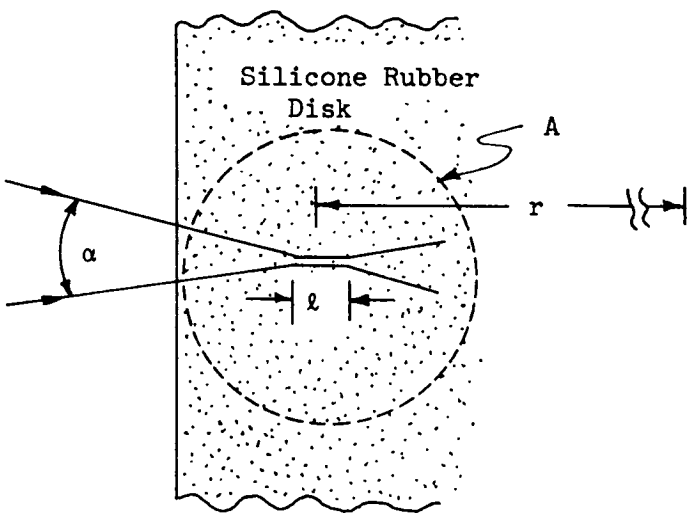

Figure 27

An Experimental Arrangement With a Fixed Velocity Gradient Along the Length ℓ of the Sensing Volume

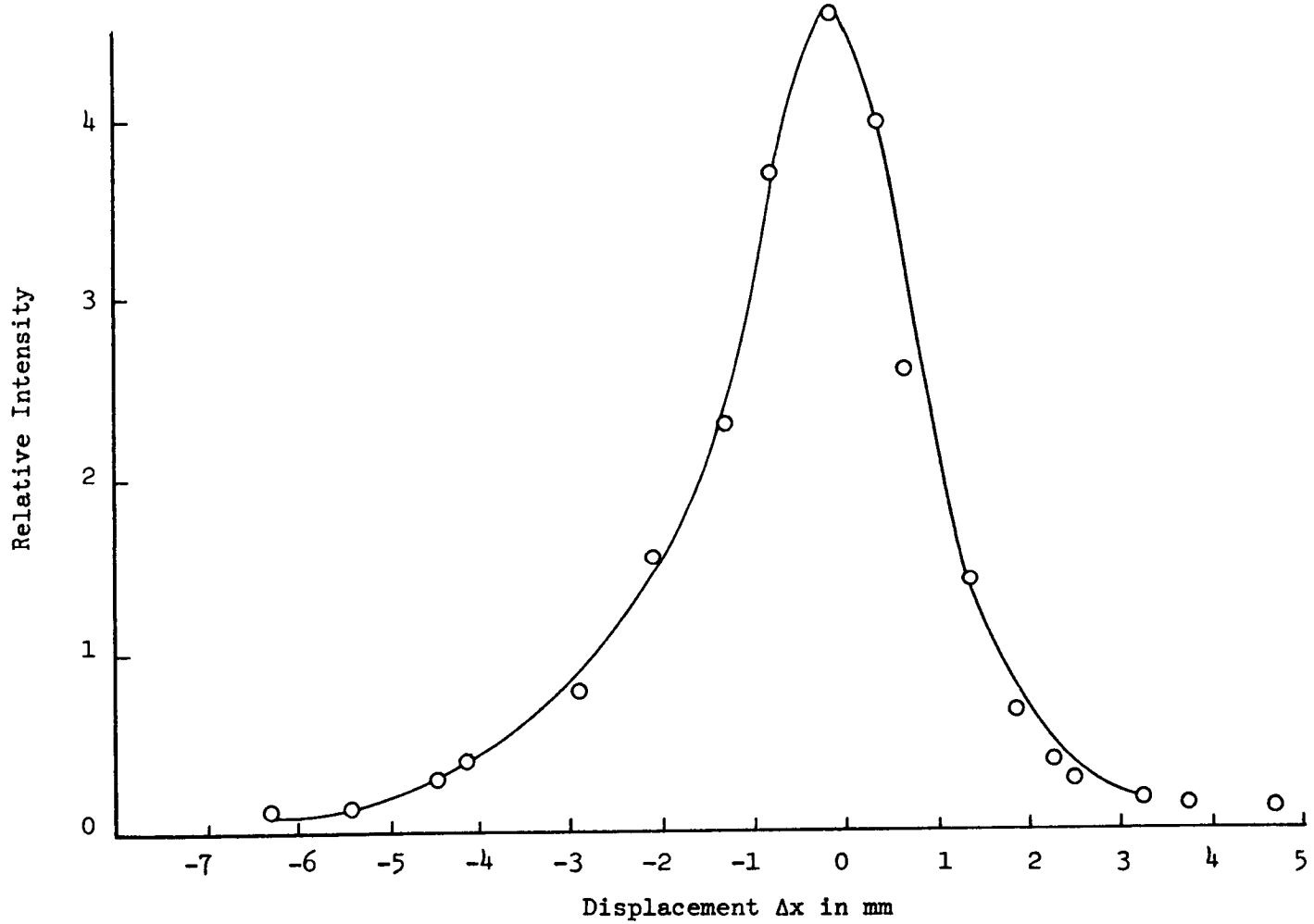

Figure 28

Relative Intensity of Light Falling on the Photomultiplier Versus Displacement Δx of the Volume Scatterer With Respect to the Center of the Sensing Volume

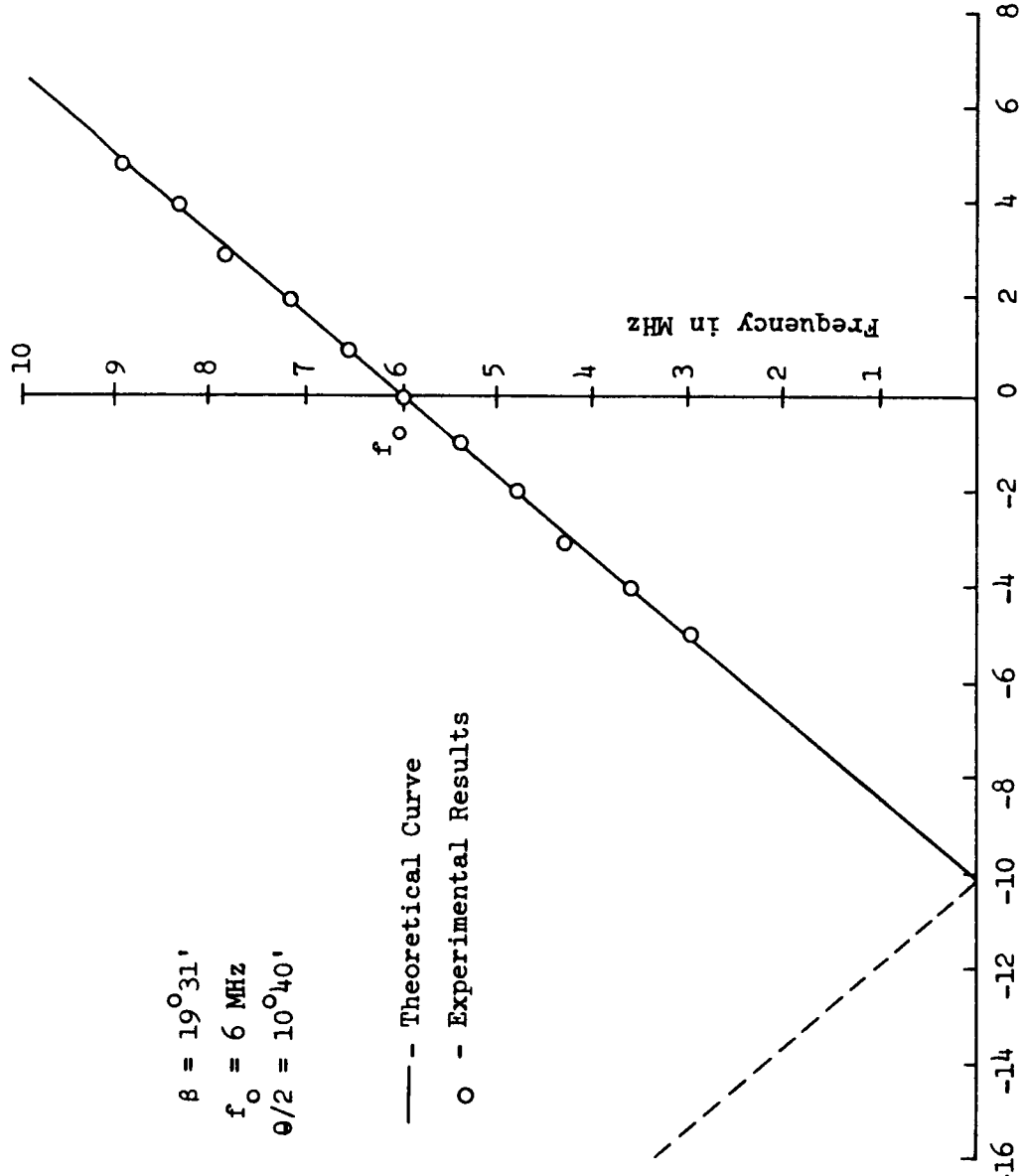

Figure 29

Doppler Shift Versus Velocity Vector in One Dimension

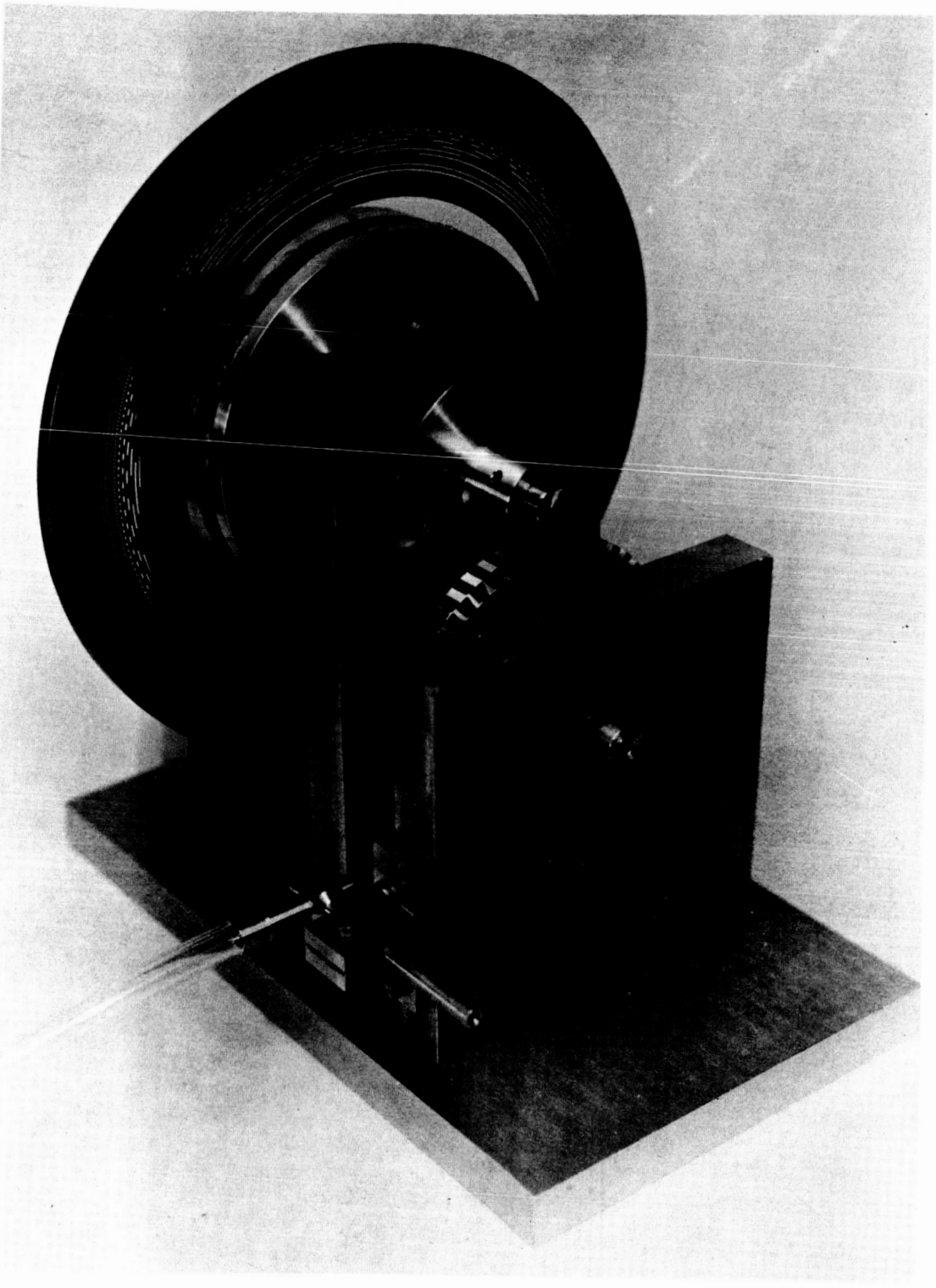

Figure 30

An Encoder Disk Used as a Rotating Diffraction Grating

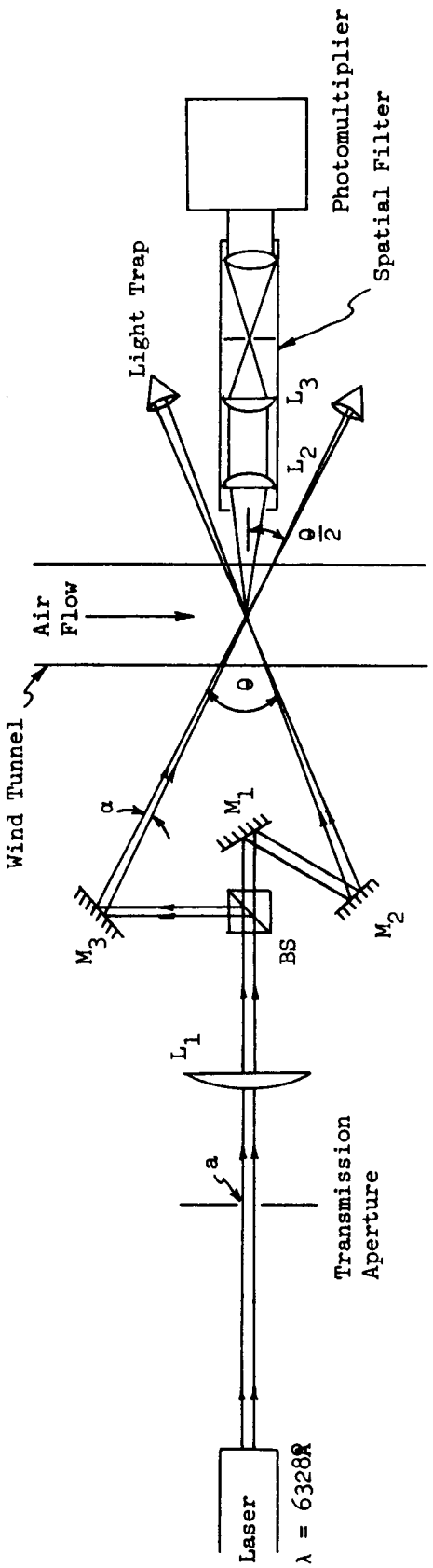

Figure 31

Optical Arrangement of the Symmetrical Heterodyning System

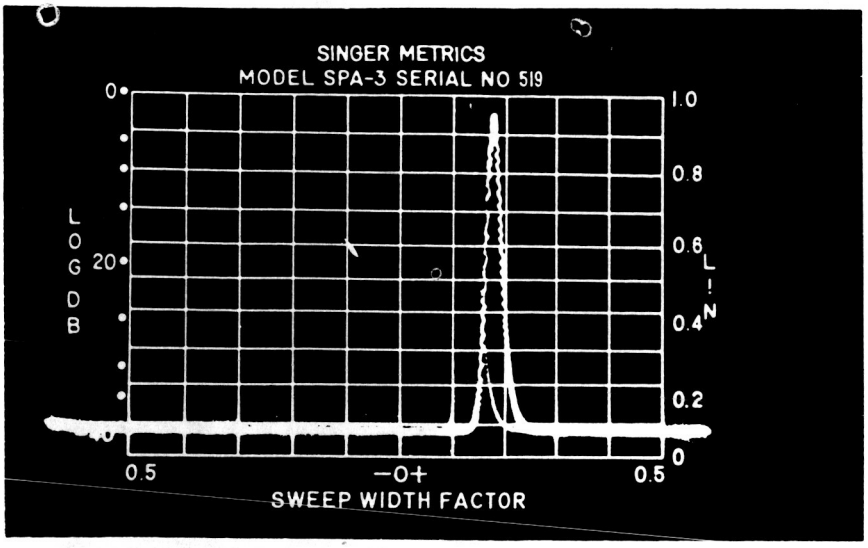

Figure 32a

Spectrum Analyzer Display of a Doppler Signal at f_c = 1.5 MHz, Sweep Width 100 kHz/Div

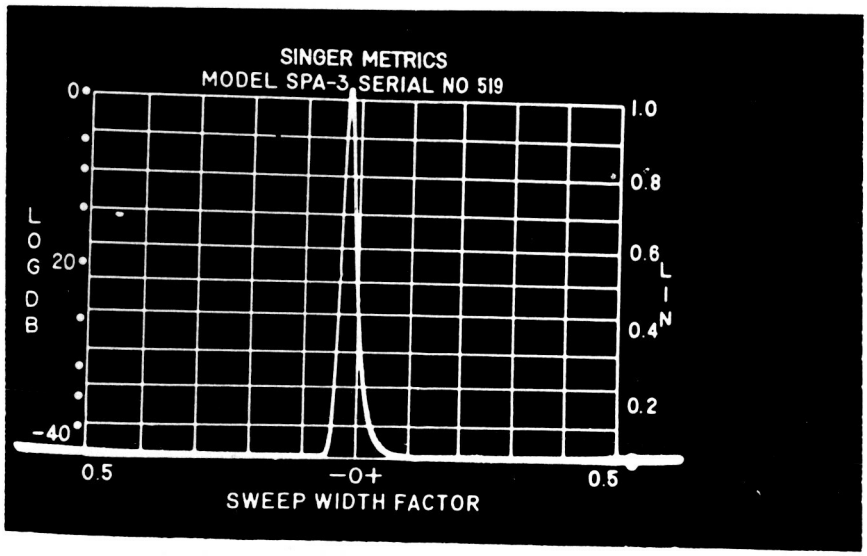

Figure 32b

Spectrum Analyzer Display of a Signal from a RF Oscillator (Frequency = 1.5 MHz, Sweep Width = 100 kHz/Div)

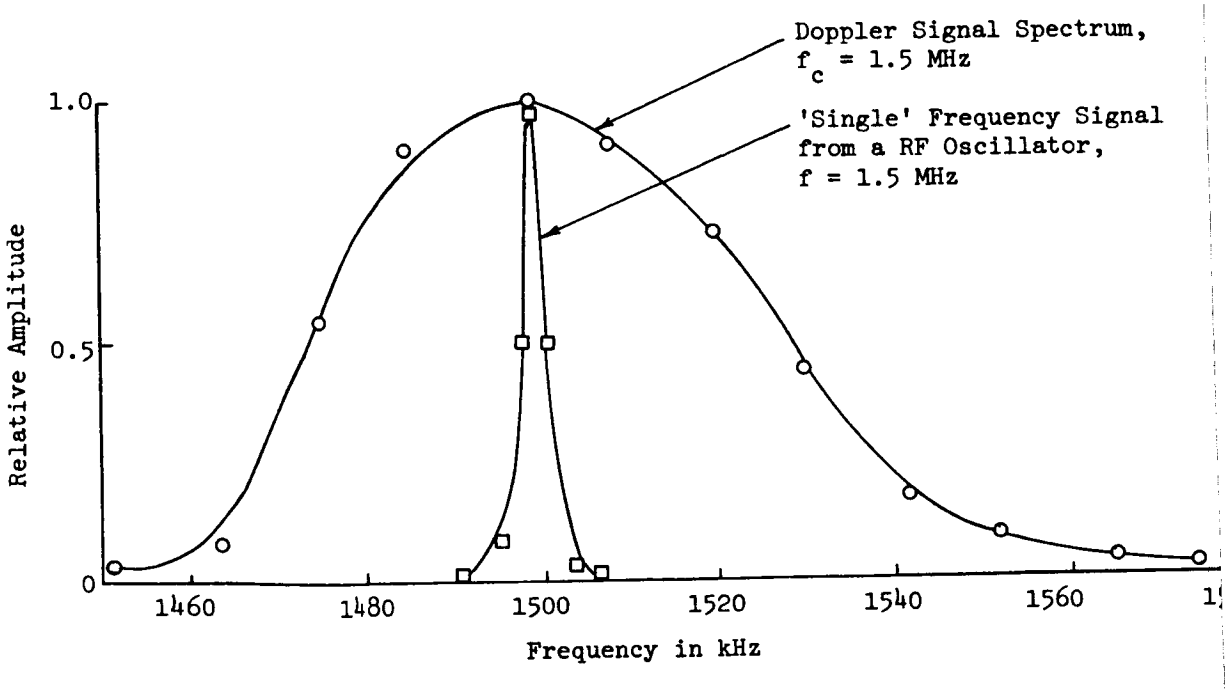

Figure 33

A Typical Doppler Signal Spectrum Is Compared with a 'Single' Frequency Signal from an Oscillator Indicating High Resolution of Communication Receiver Measurements

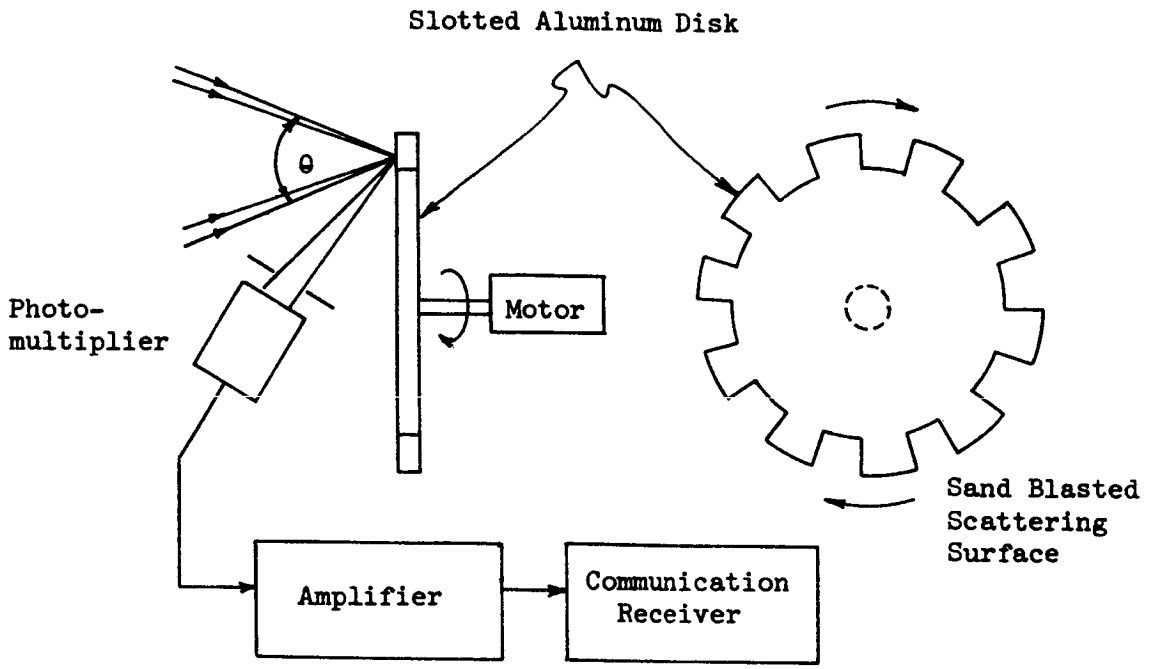

Figure 34

An Experimental Arrangement for Generating a Time-Discontinuous Doppler Signal from a Surface Scatterer

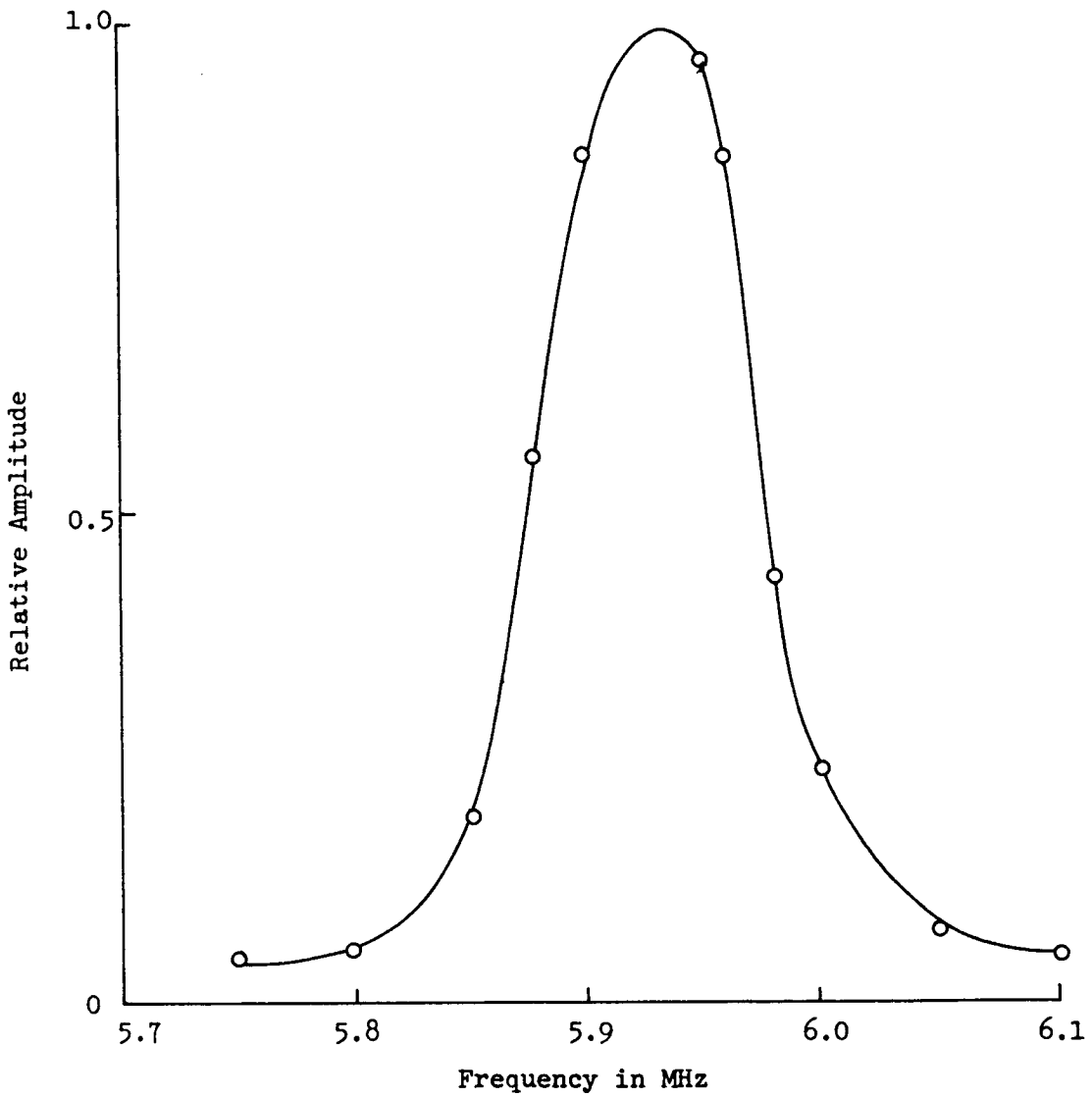

Figure 35

Time Discontinuous Doppler Signal Spectrum Measurements by Communication Receiver (δf_τ Was Deliberately Introduced as Shown in Figure 34)

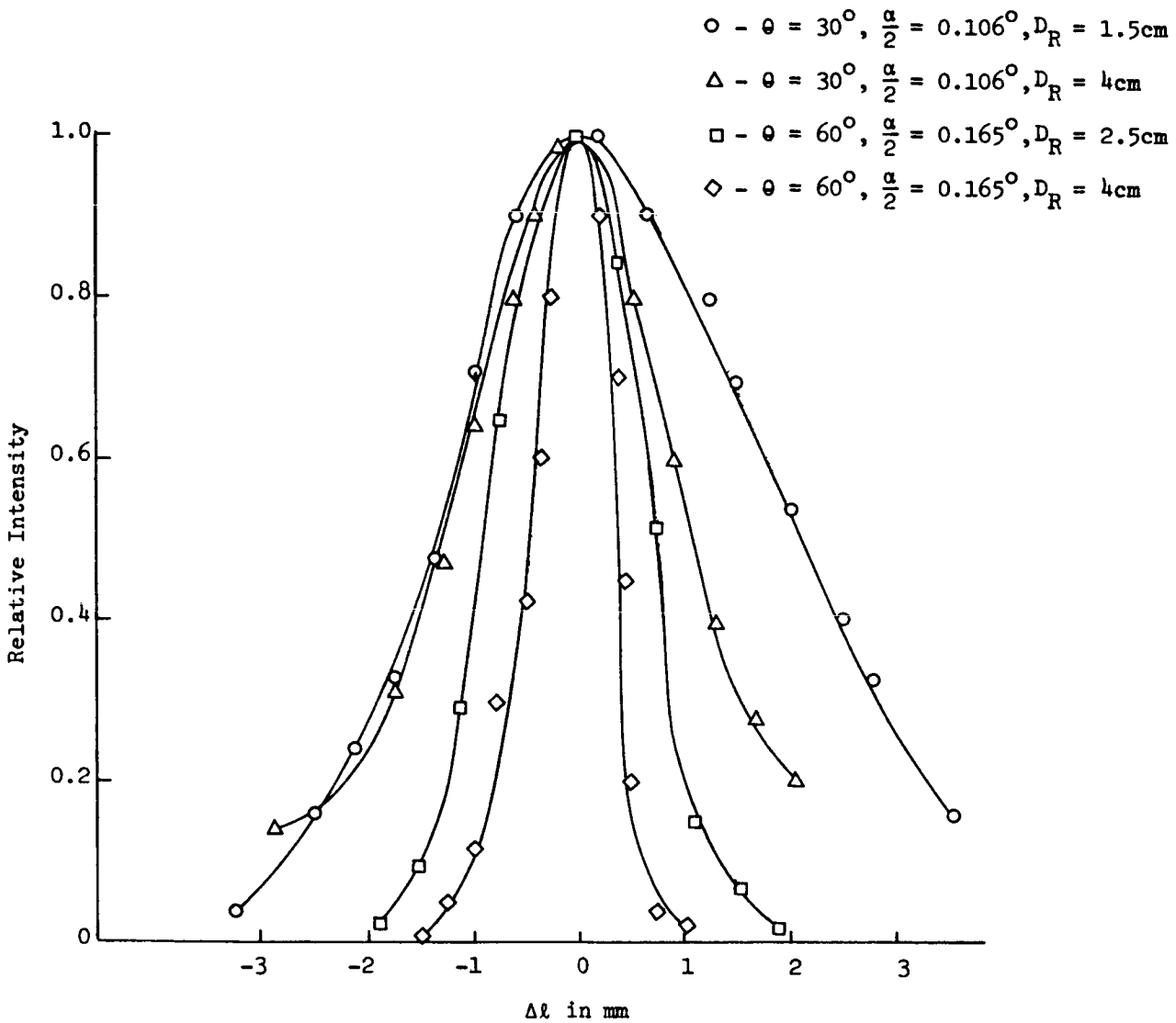

Figure 36

Relative Intensity of Light Falling on the Photomultiplier from the Sensing Volume Versus Displacement Δℓ Showing the Spatial Resolution in the Lateral Spatial Axis

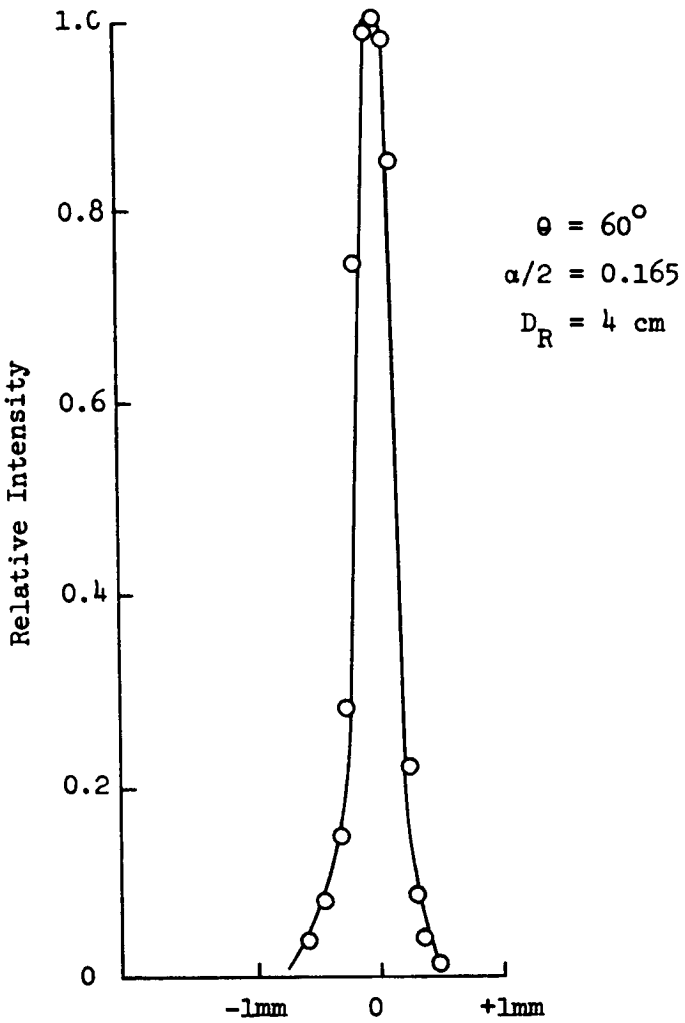

Figure 37

Improved Spatial Resolution Obtained by Tilting the Receiving Optical Axis by an Angle of 30° in a Plane Perpendicular to That Containing the Transmission Optical Axis

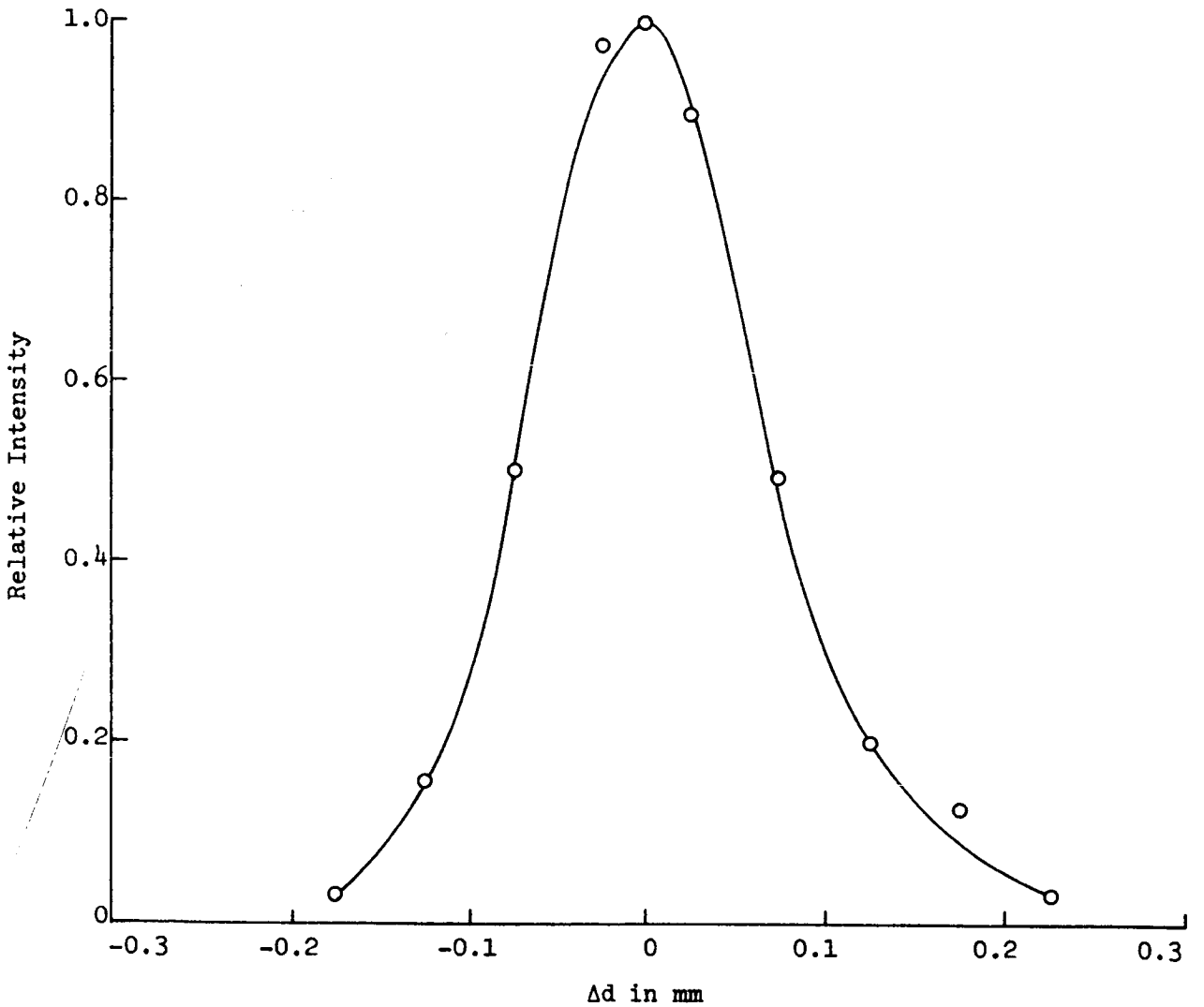

Figure 38

Relative Intensity of Light Falling on the Photomultiplier from the Sensing Volume Versus Displacement Δd Showing the Spatial Resolution in the Longitudinal Axis

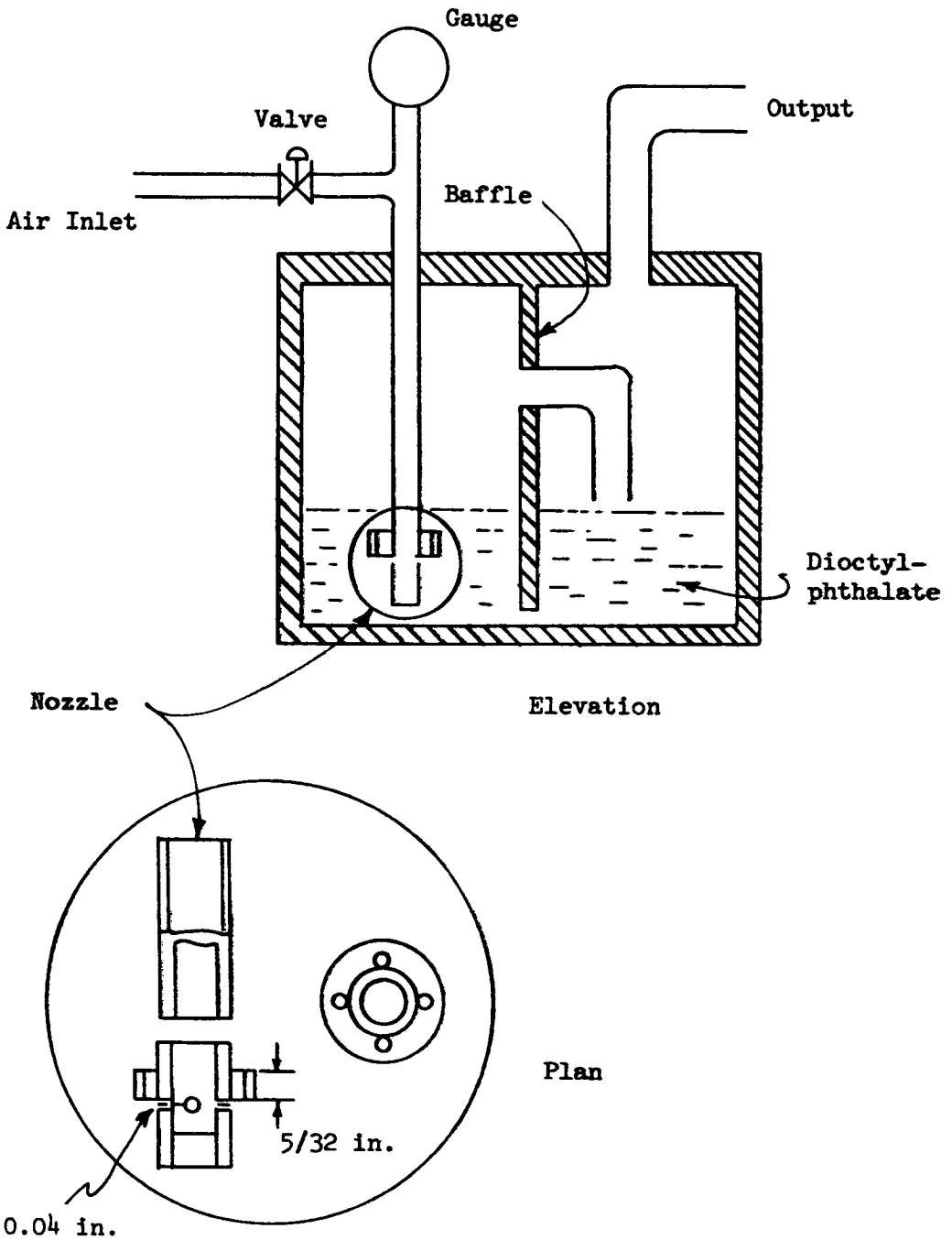

Figure 39a

Dioctyl-Phthalate Aerosol Generator

Figure 39b

DOP Aerosol Generator

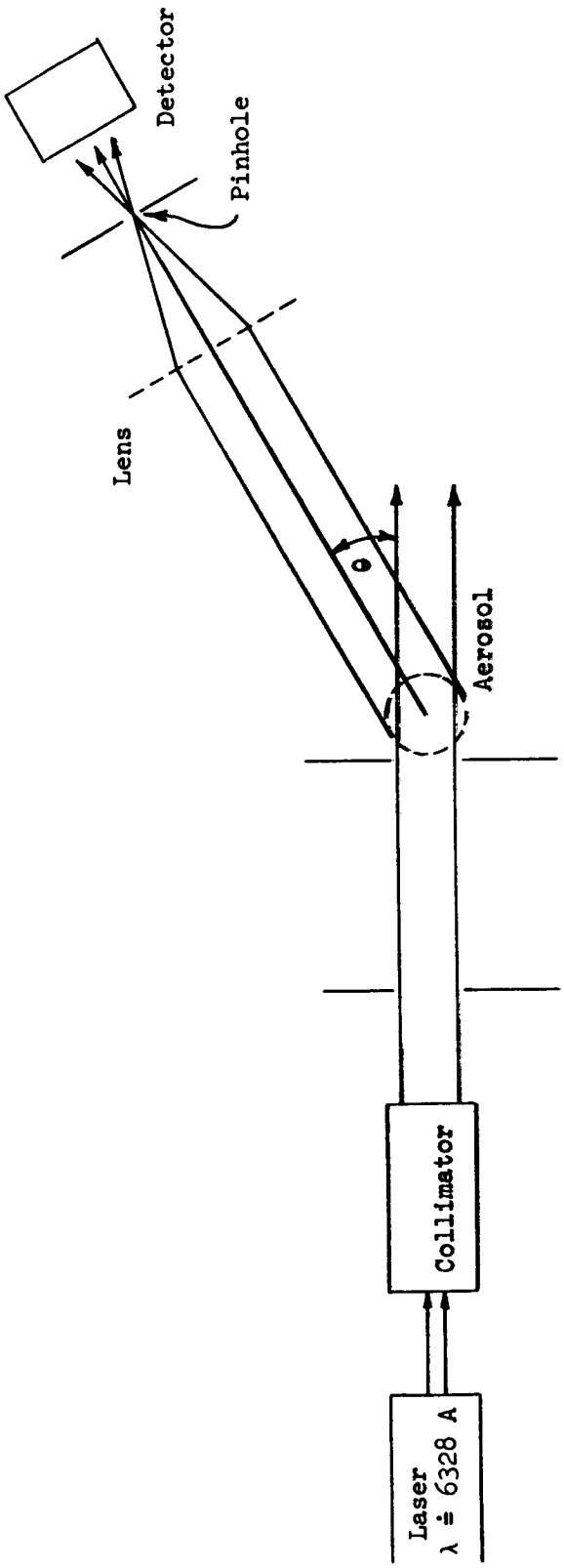

Figure 40

Diagram of Experimental Setup for Measuring Angular Scattering Intensity Function Using a Wide Angle Optical Spectrum Analyzer

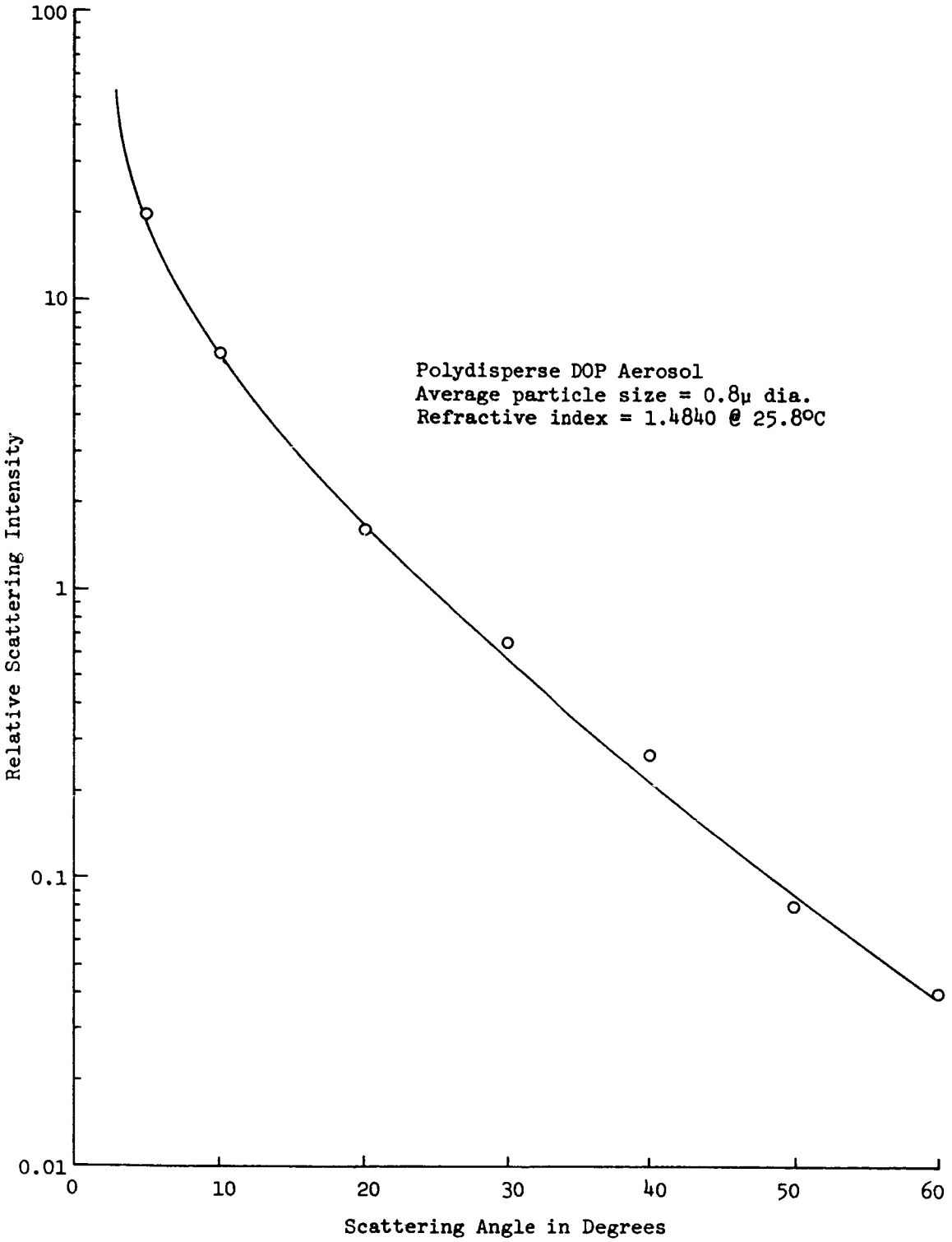

Figure 41

Relative Scattering Intensity Versus Scattering Angle for Polydisperse Submicron Size DOP Aerosol

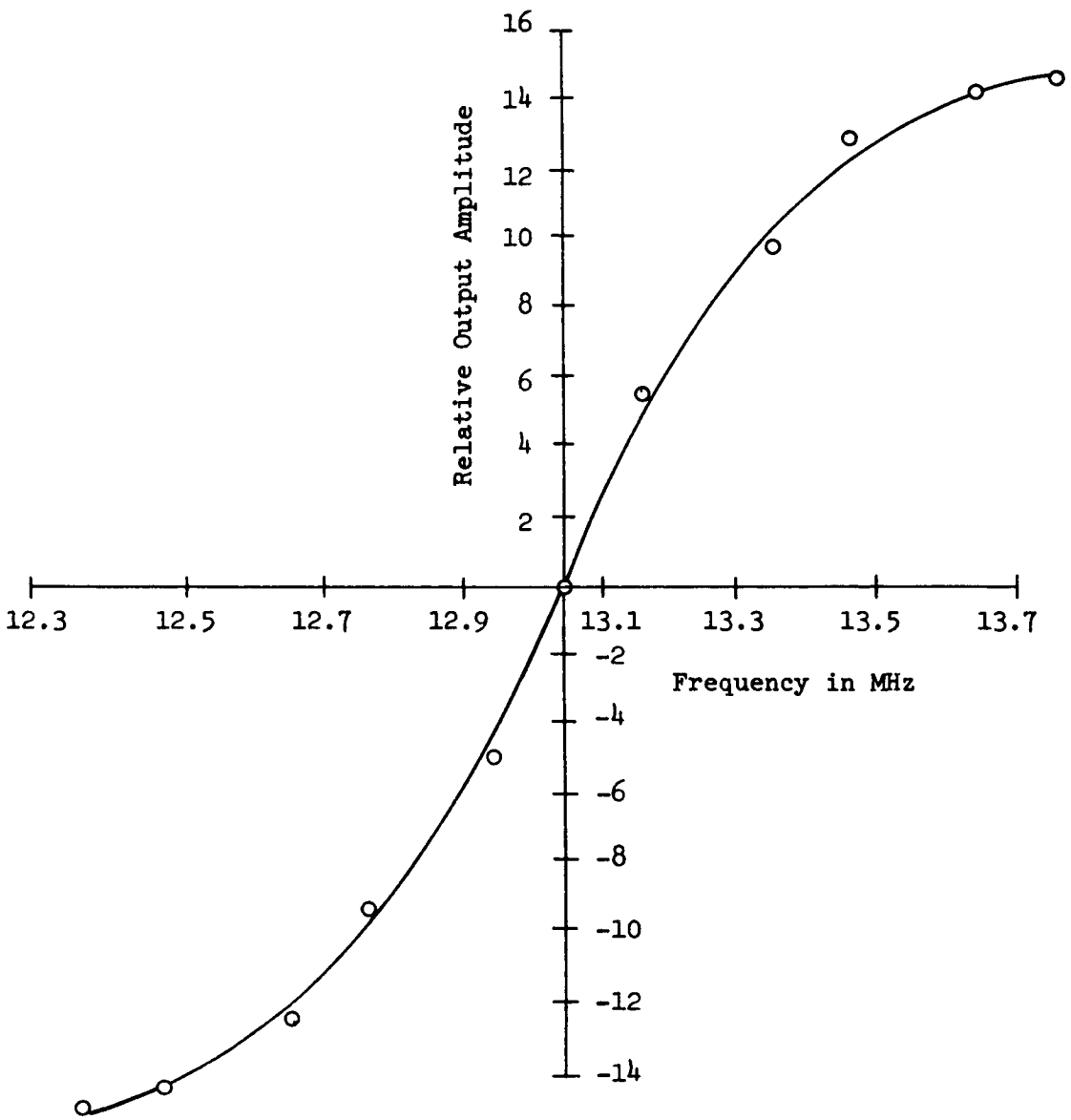

Figure 42

Characteristic Curve of a Q-Spoiled Ratio Detector

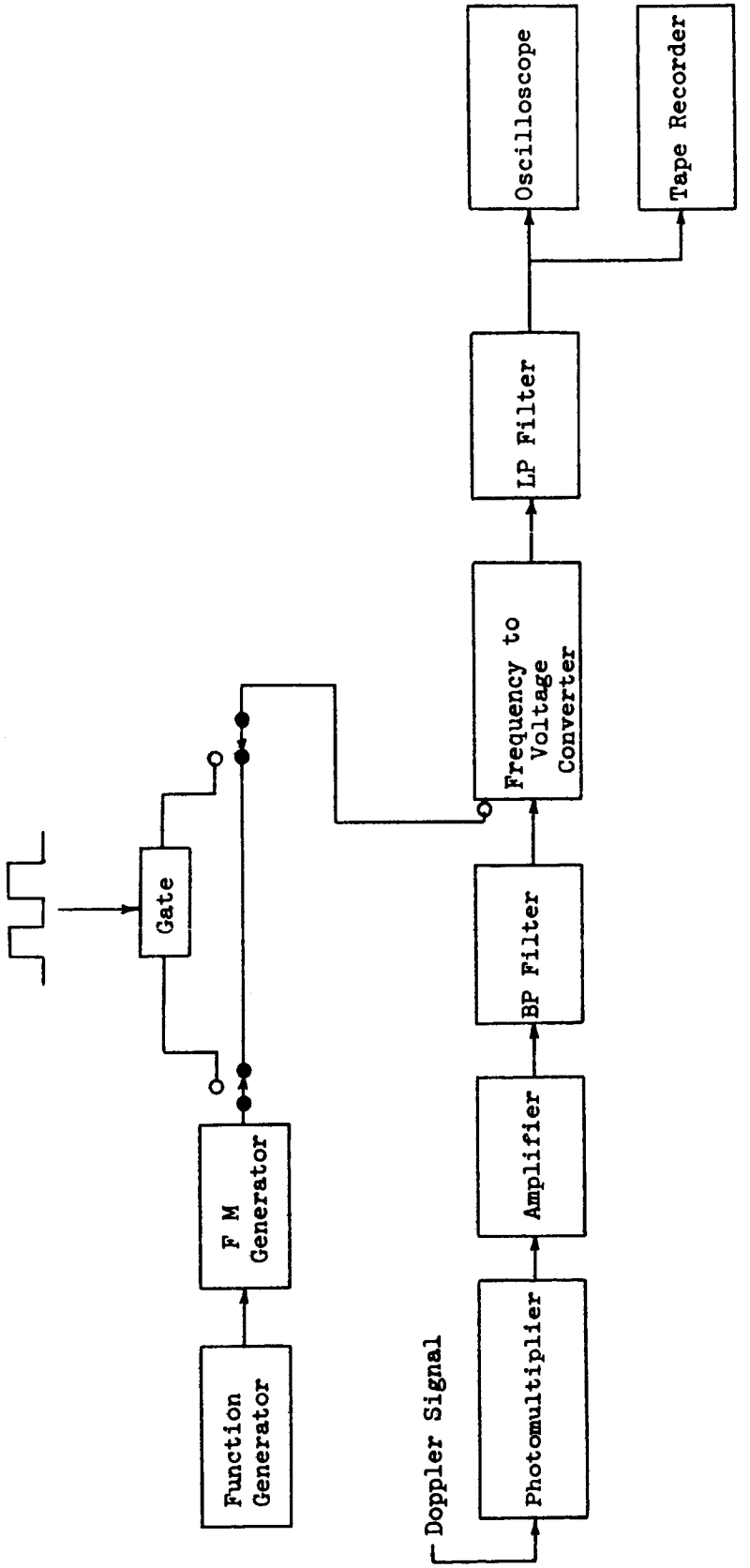

Figure 43

Block Diagram of an Experimental Arrangement for Frequency-to-Voltage Conversion of the Doppler Signal. A Test Setup Using a Simulated Signal Is Also Shown

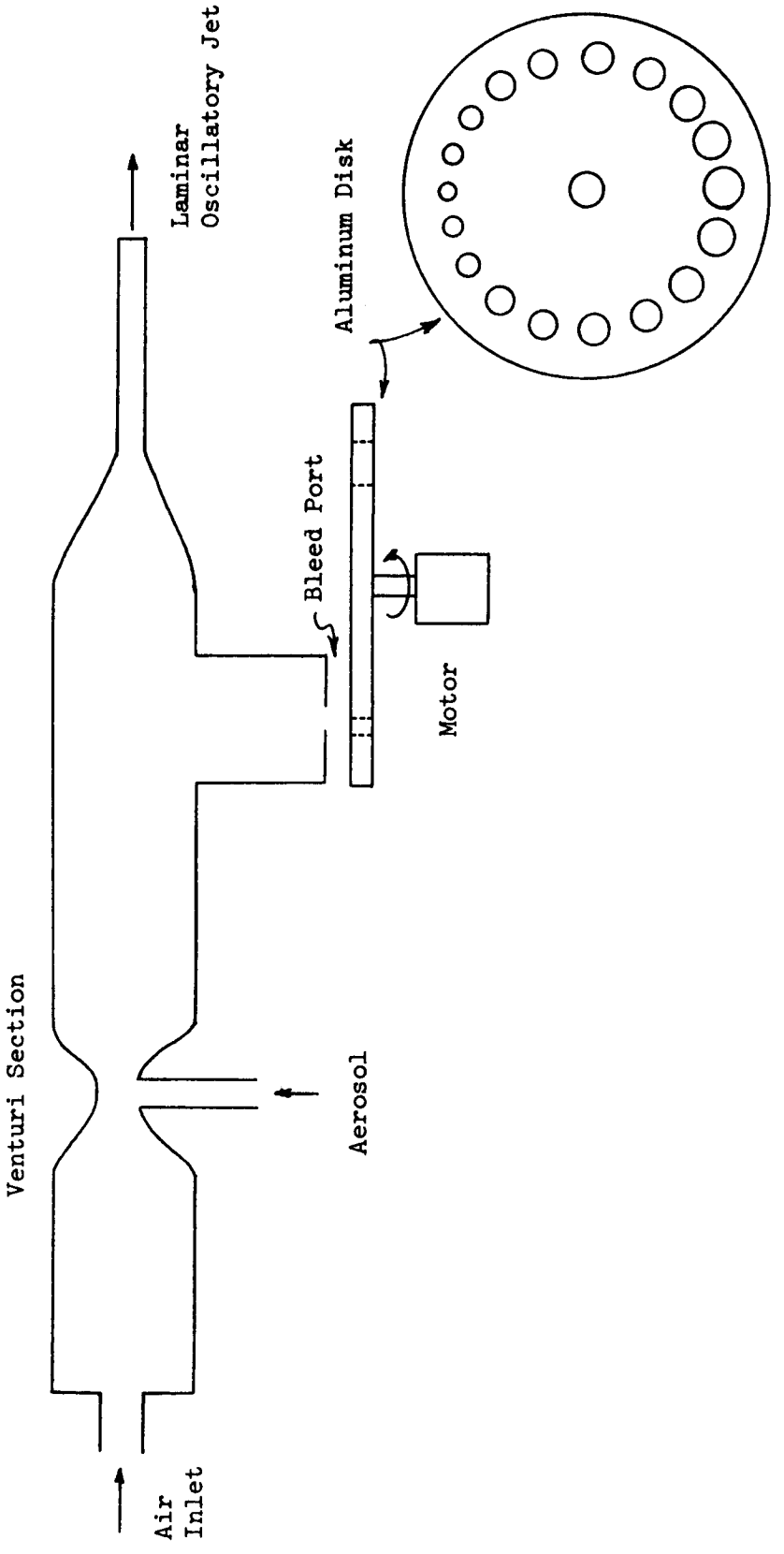

Figure 44

Schematic Diagram of Flow Modulator

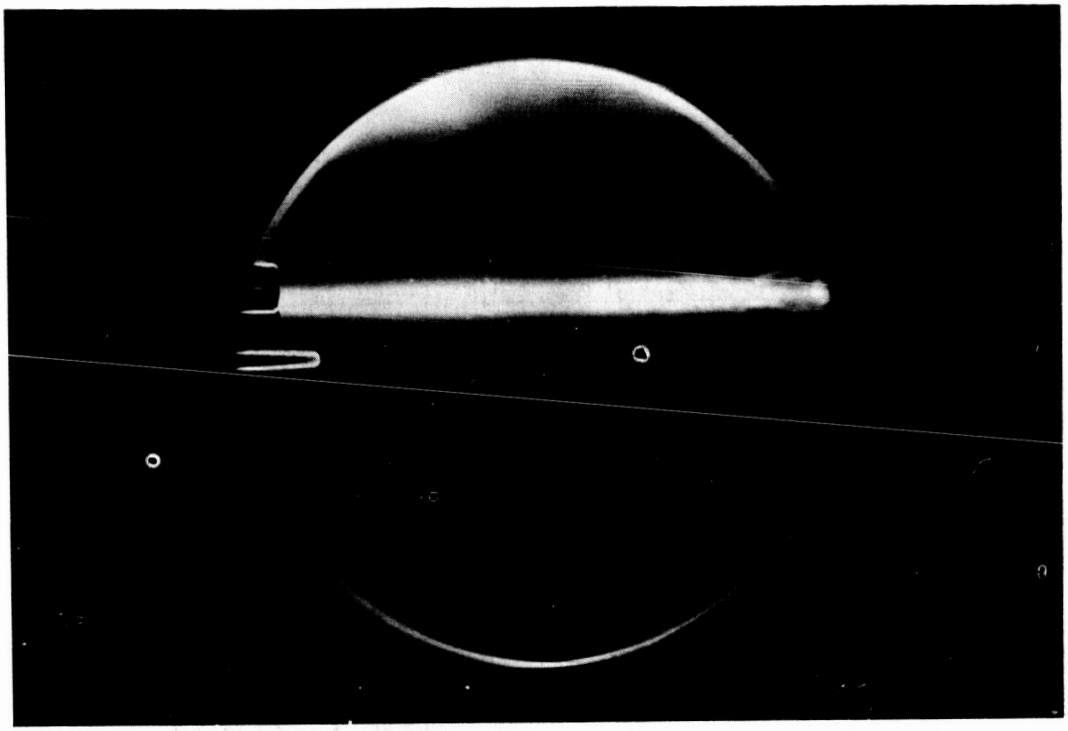

Figure 45

A Schlieren Photograph of the Laminar Oscillatory Jet from the Flow Modulator

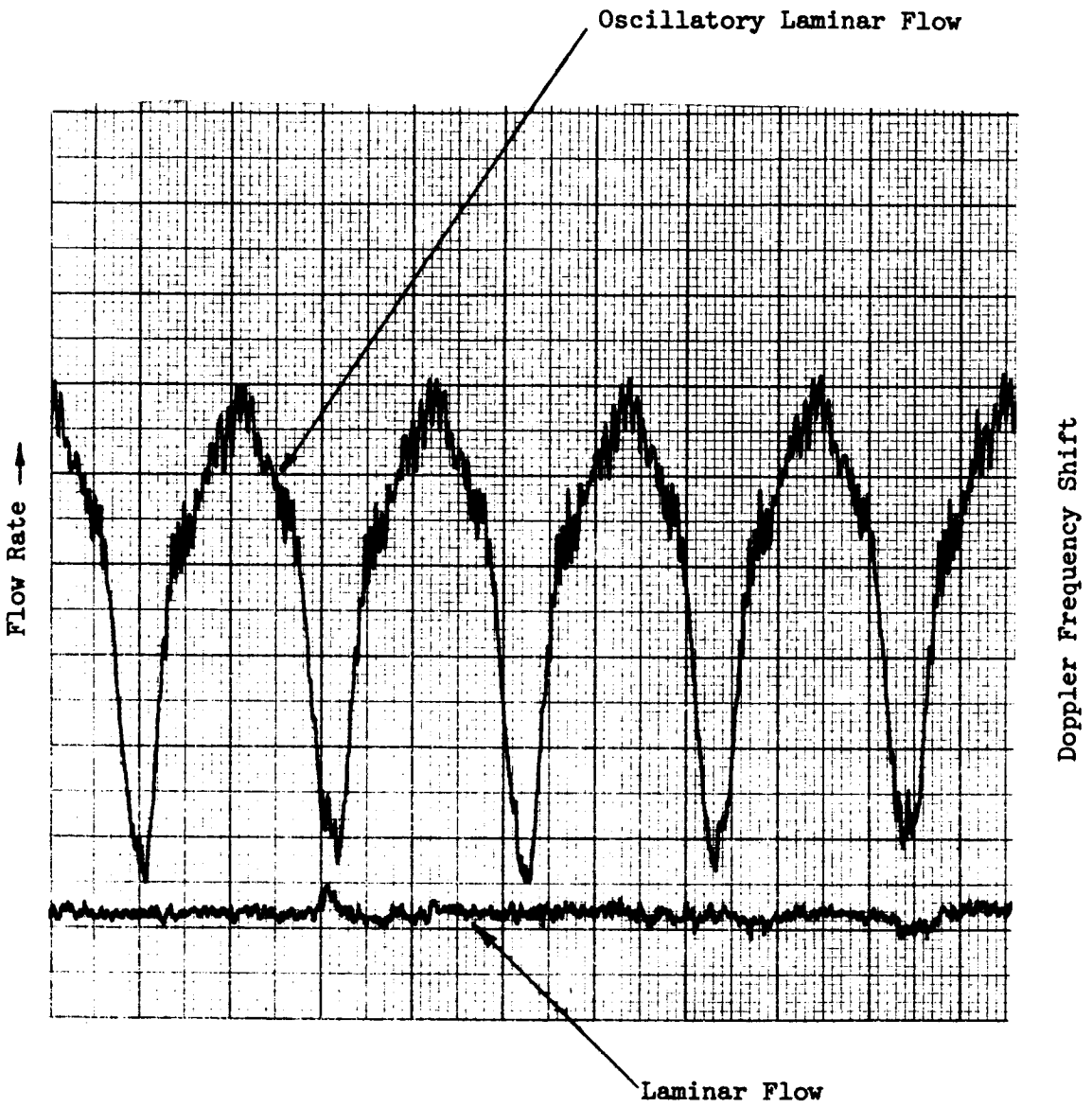

Figure 46

Frequency Discriminator (HP Model 5210A) Output Record from Laminar and Oscillatory Laminar Flows. (Horizontal Scale: 1 inch = 20 seconds; vertical scale: 1 inch = 5.5 cm/sec or 100 kHz)

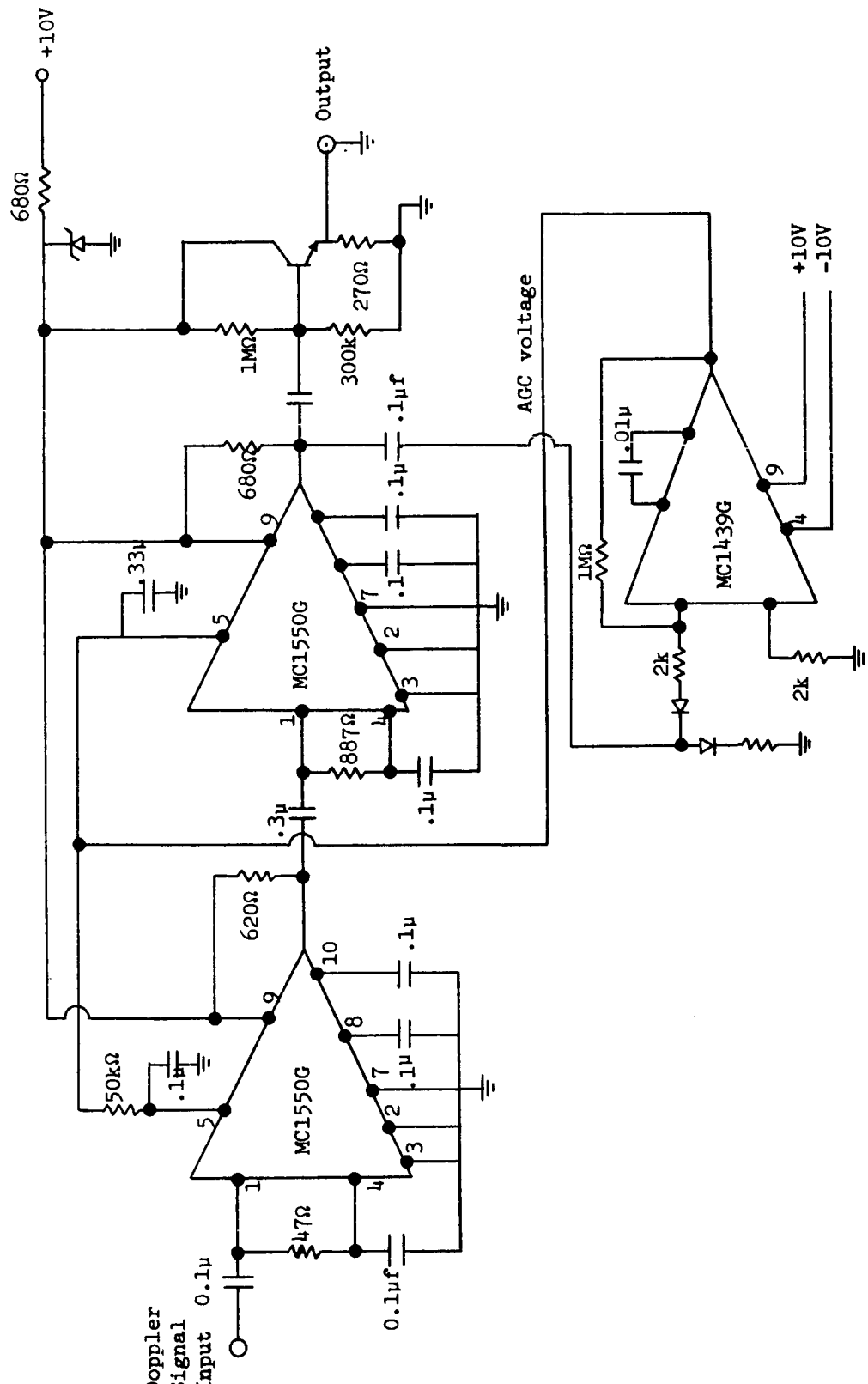

Figure 47

Schematic Diagram of the AGC Circuit

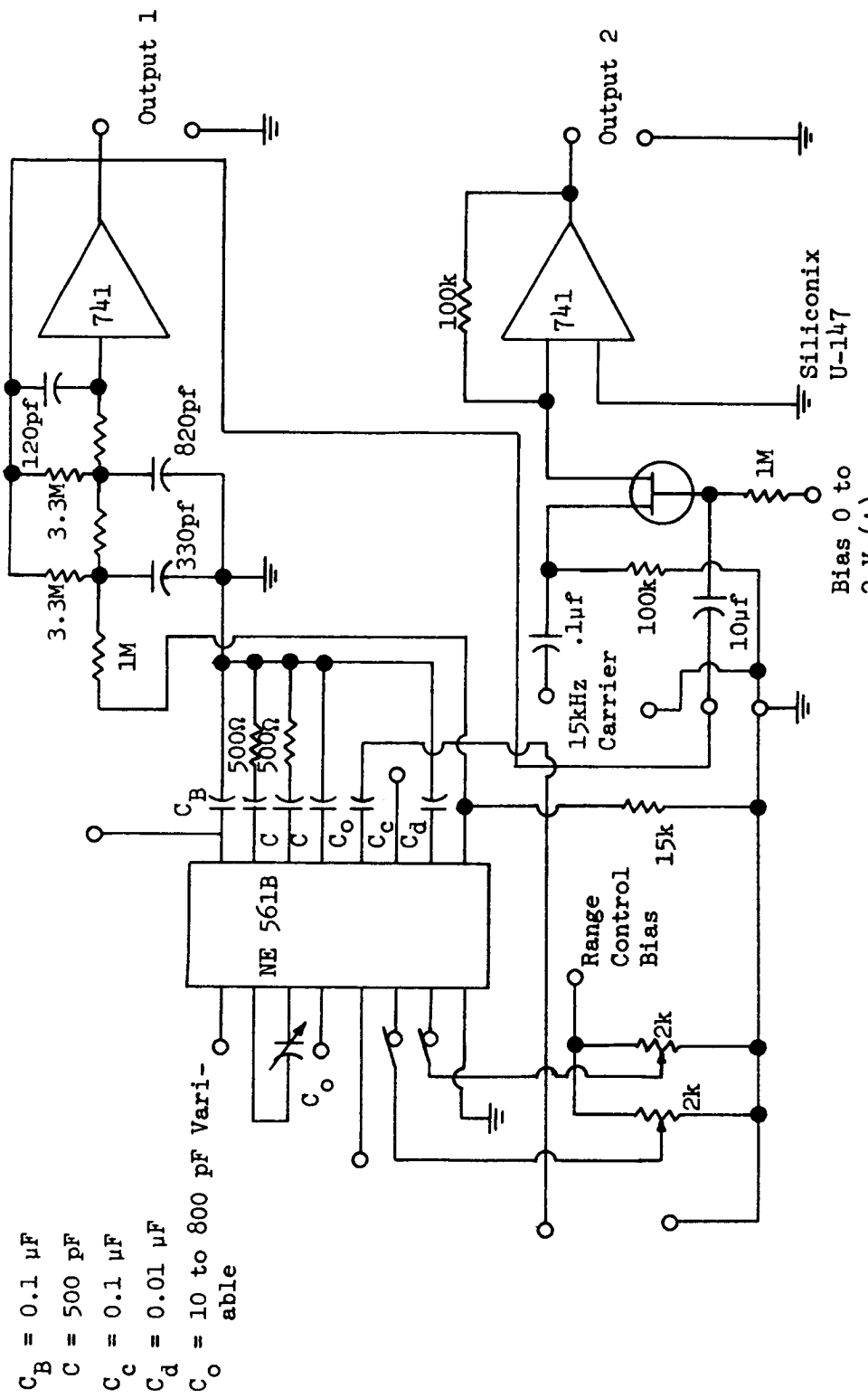

Figure 48

Circuit Diagram of the Phase-Locked Loop Detector

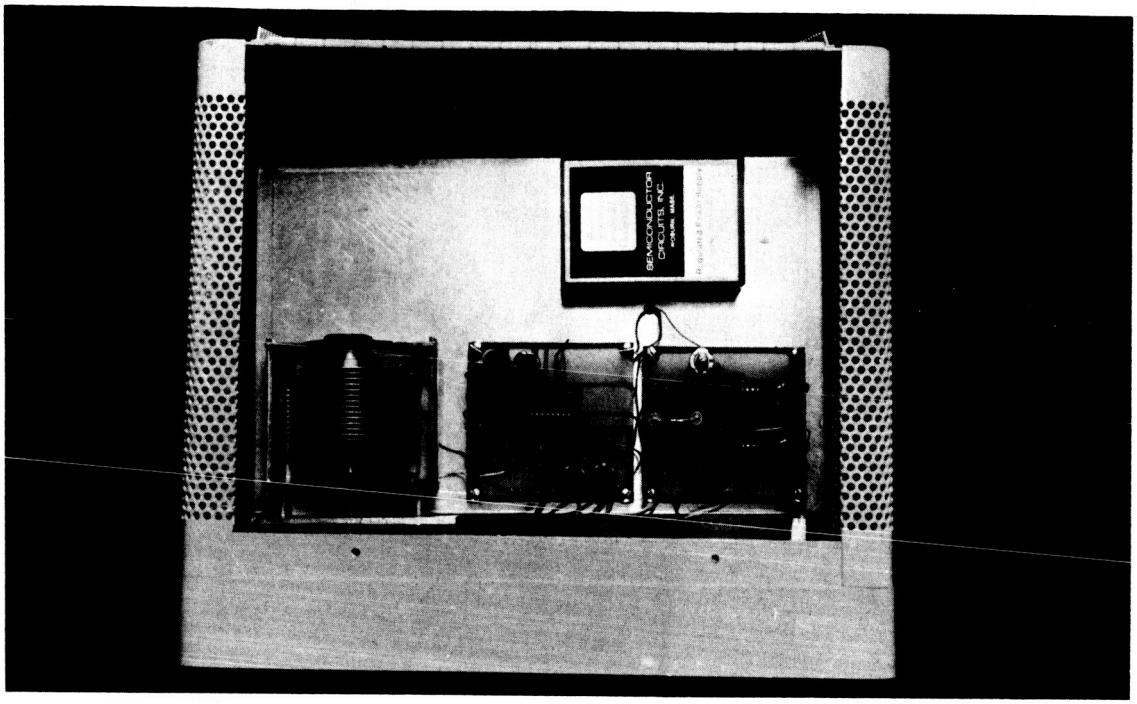

Figure 49

Interior View of the Phase-Locked Loop Detector

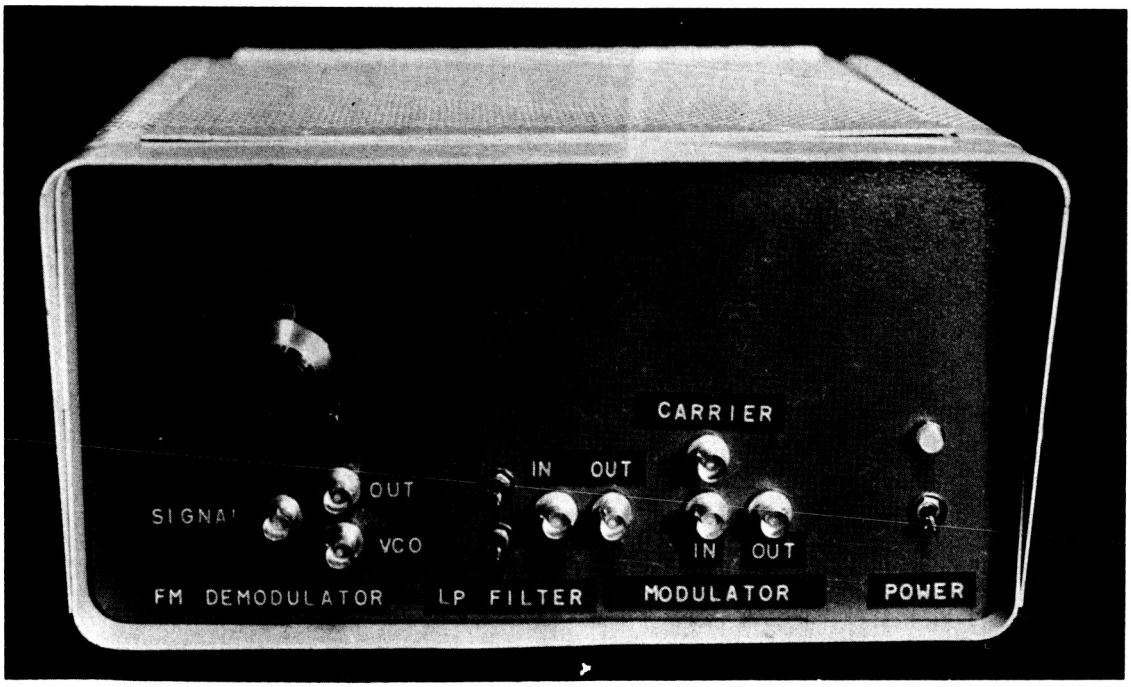

Figure 50

Phase-Locked Loop Detector

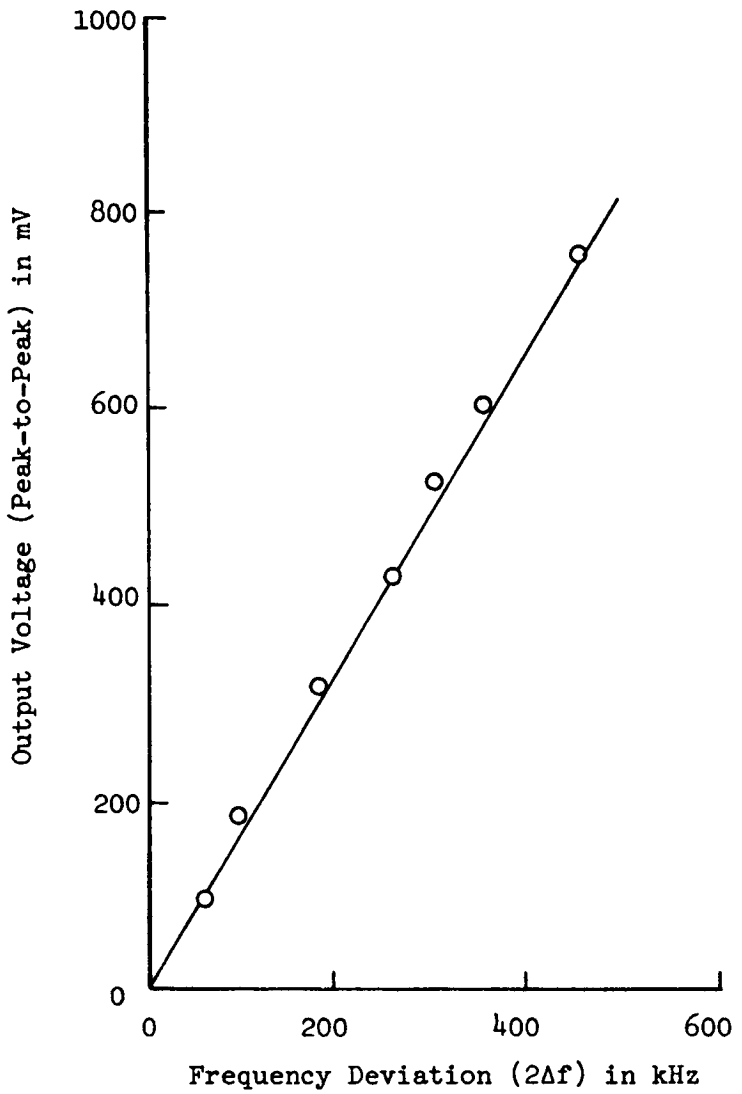

Figure 51

Frequency-to-Voltage Conversion Characteristic of the Phase-Locked Loop Detector

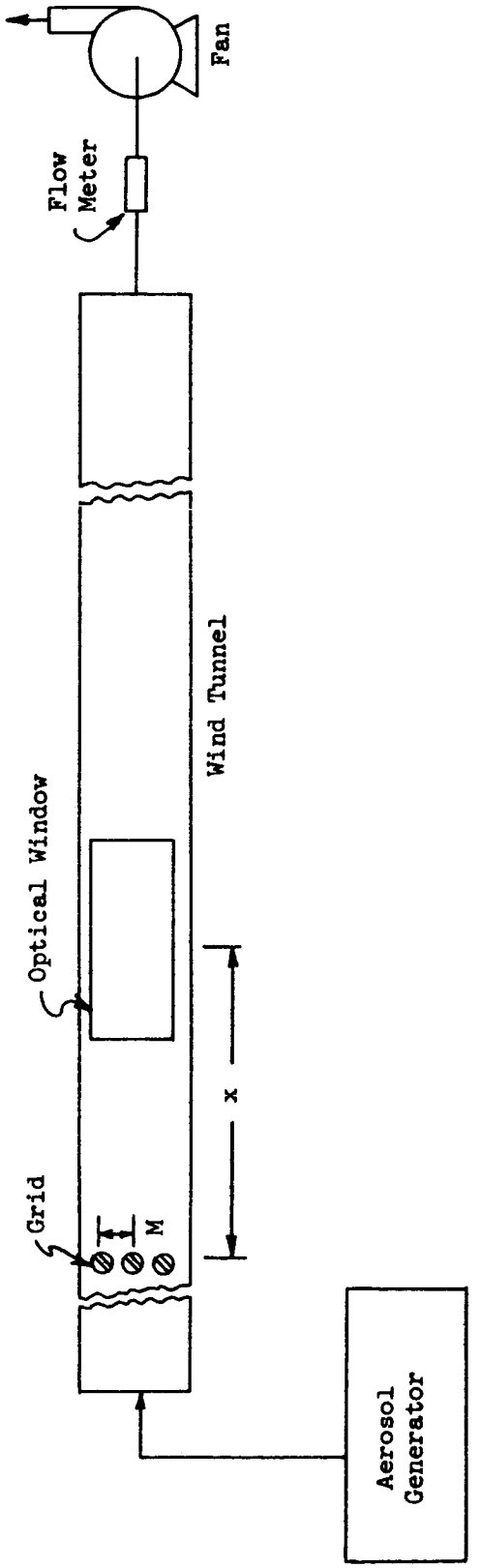

Figure 52

Schematic Diagram of the Flow System

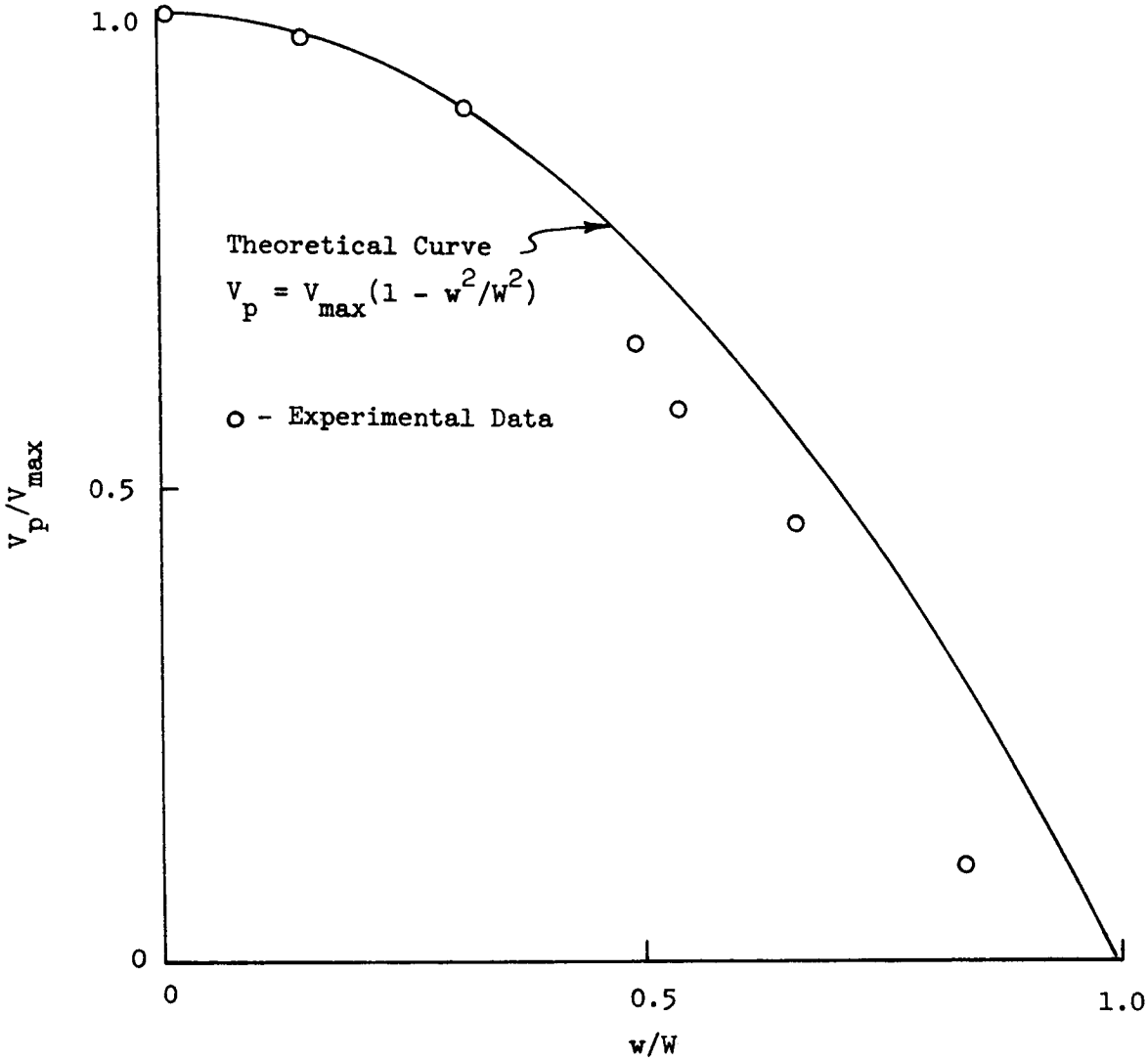

Figure 53

Measurement of the Laminar Velocity Profile in a Square Duct

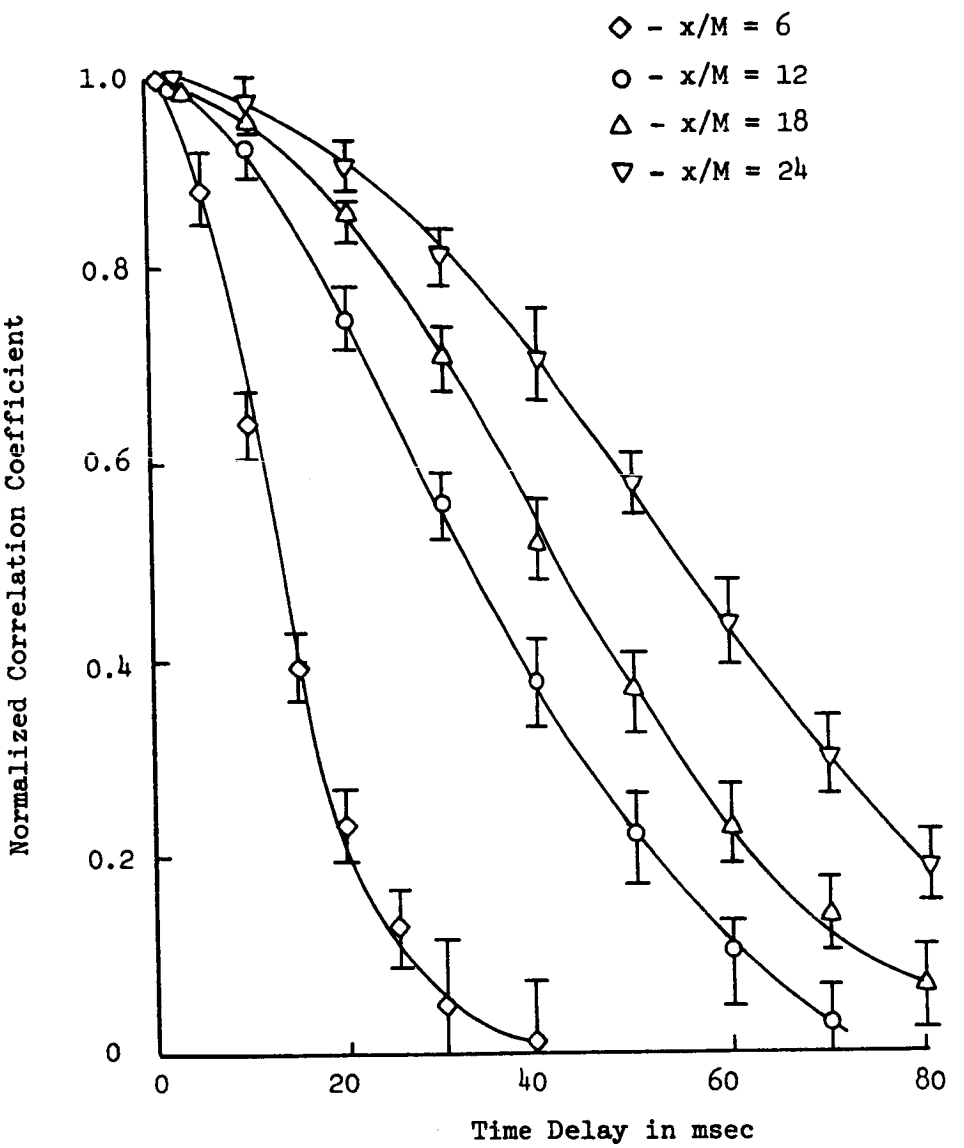

Figure 54

Velocity Auto-Correlation Versus Delay Time
(Analog Correlation Measurement)

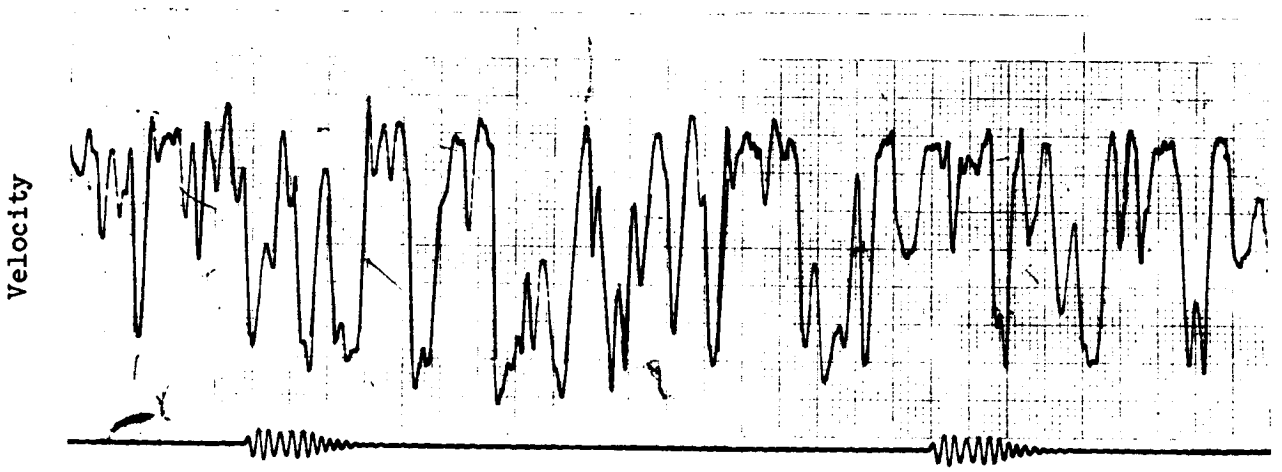

Figure 55

A Typical Signal Record for x/M = 9.
The Marker Signal Below Shows a One Second Time Interval.
In the Vertical Scale Each Small Division (1 mm) = 1.2 cm/sec.

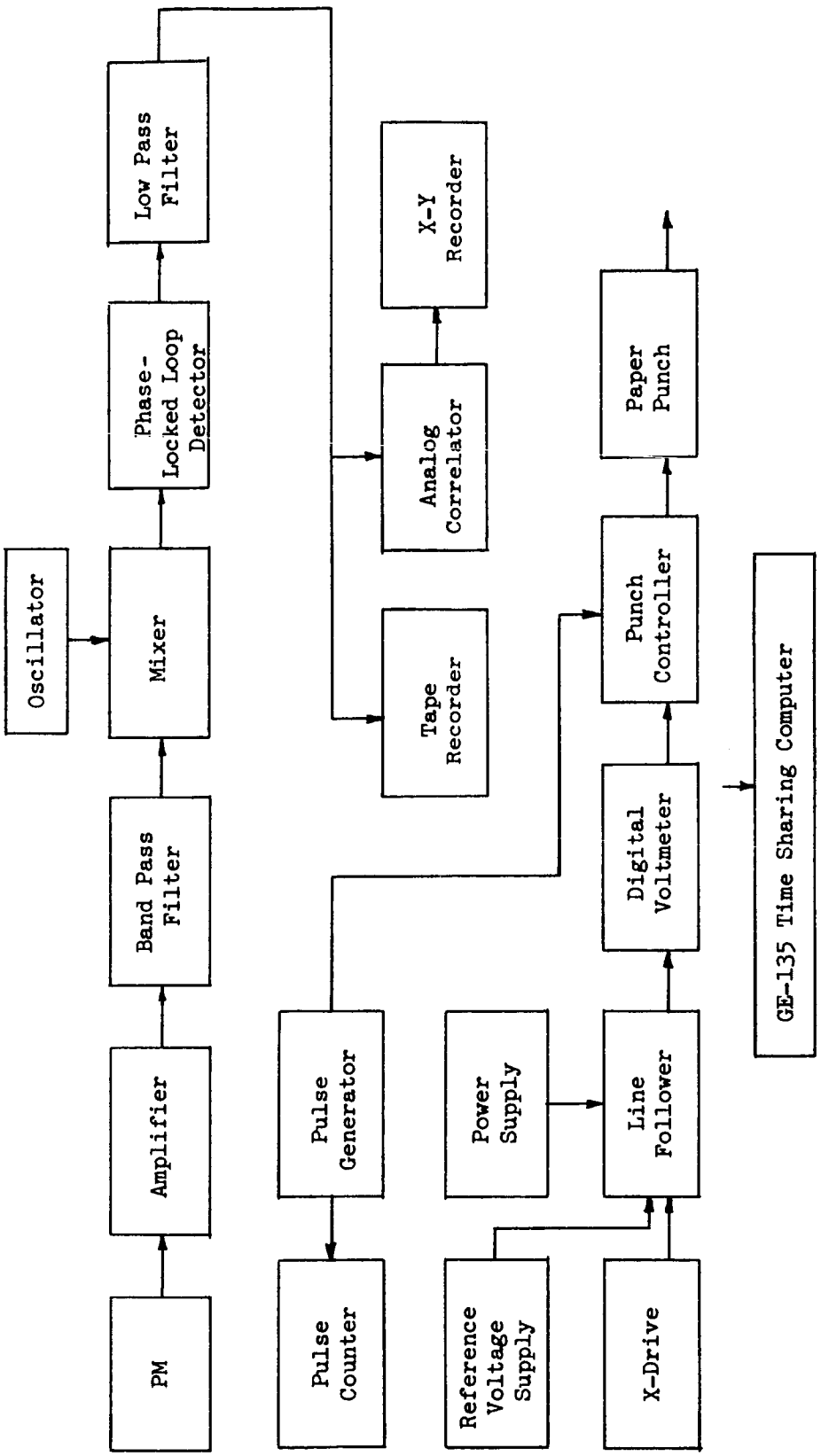

Figure 56

Block Diagram of the Signal Processing and Digitization System

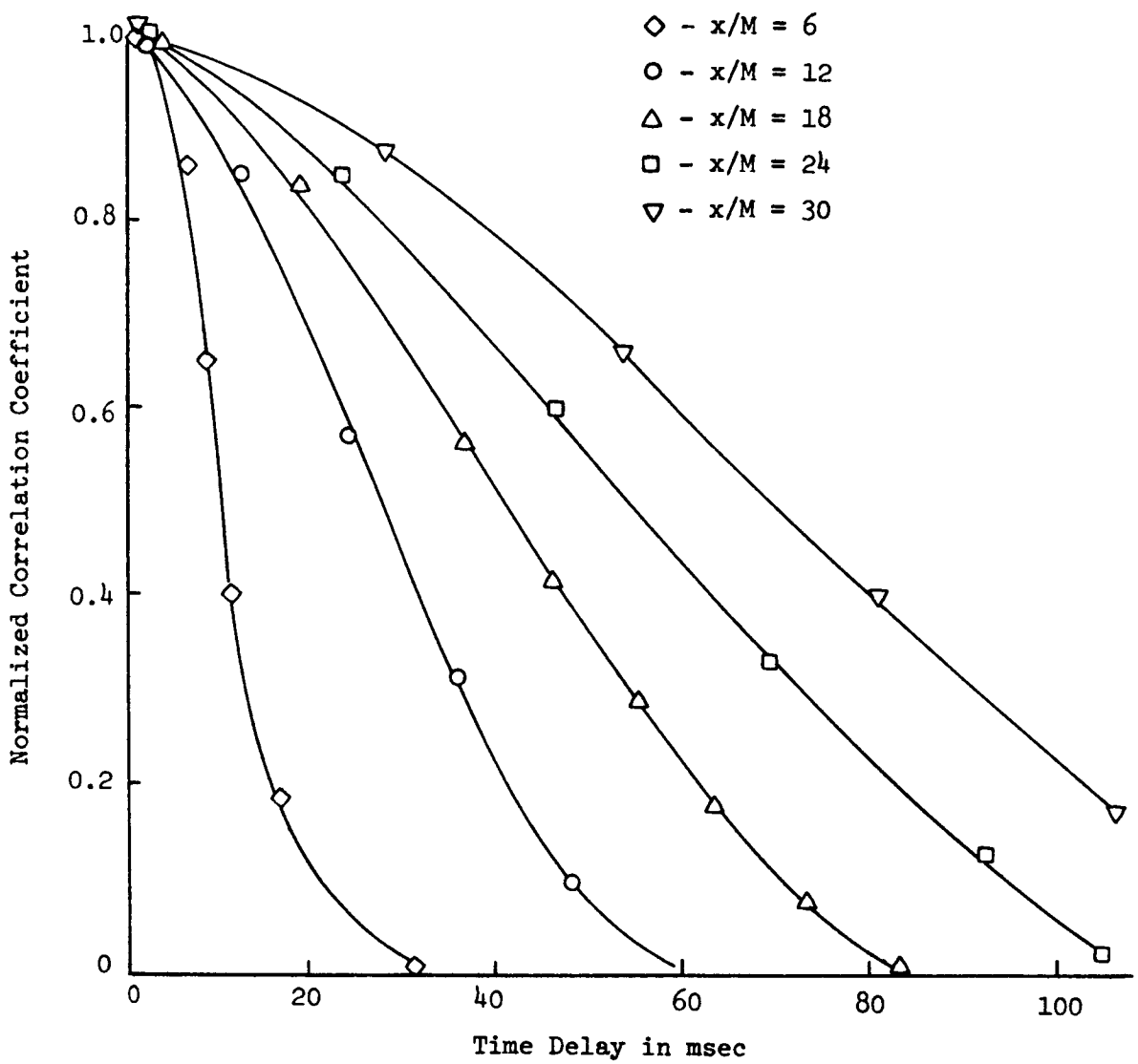

Figure 57

Velocity Auto-Correlation Coefficient Versus Delay Time
(Digital Correlation Measurement)

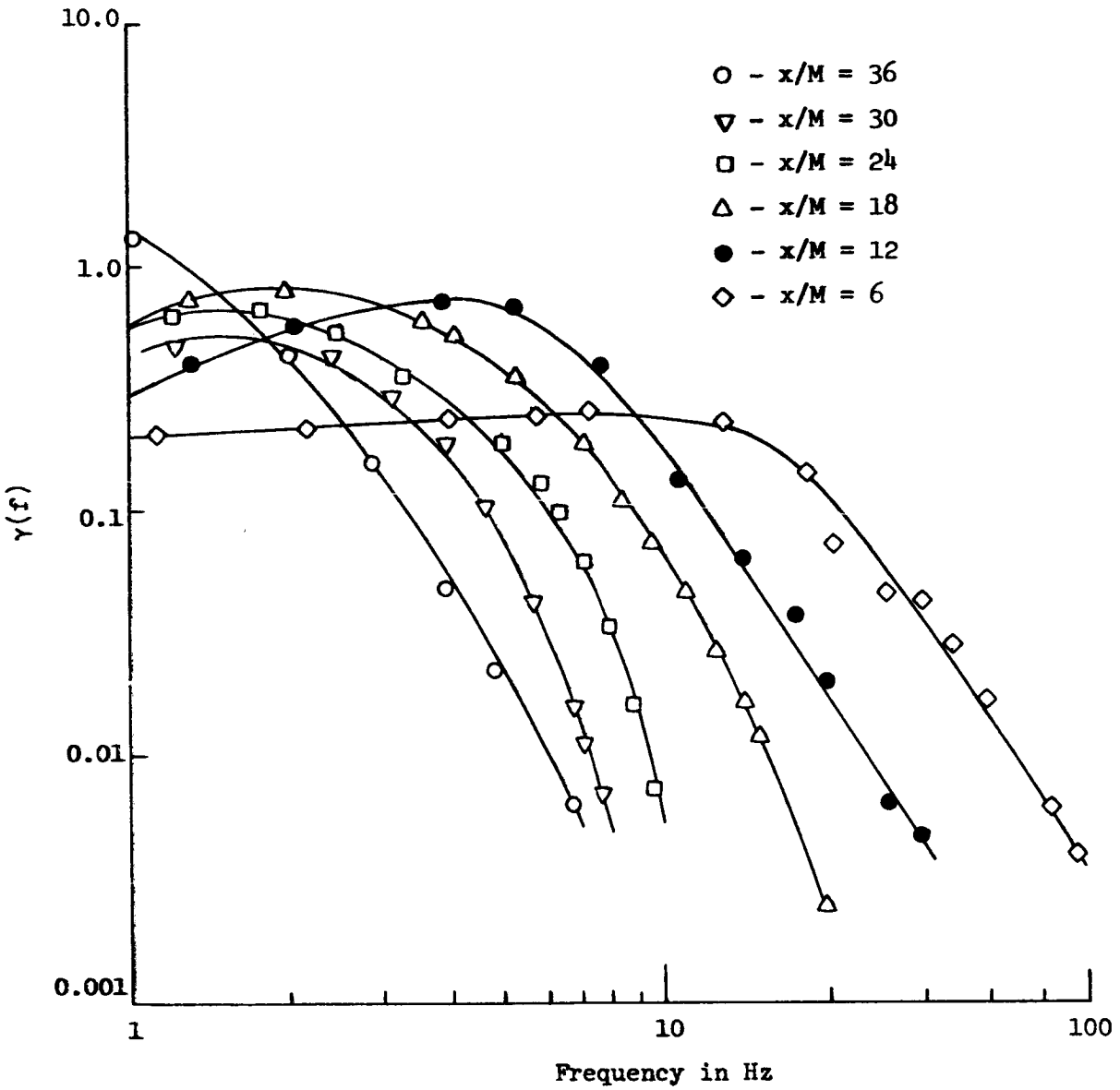

Figure 58

One-Dimensional Energy Spectrum of Turbulence of Low Reynolds Number

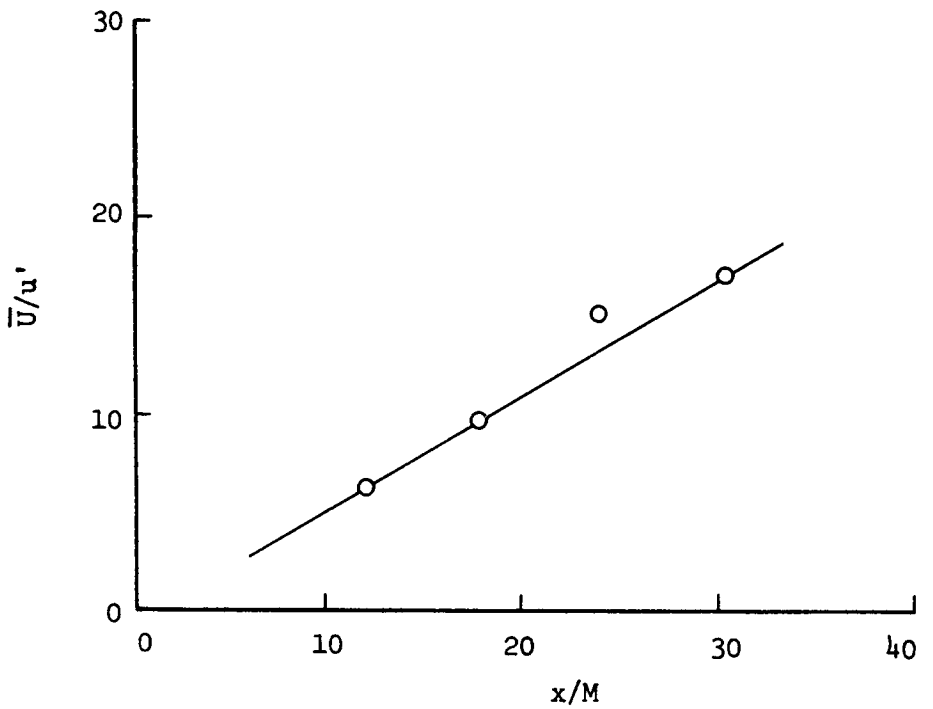

Figure 59

Decay of Turbulence Behind a Grid of Round Bars

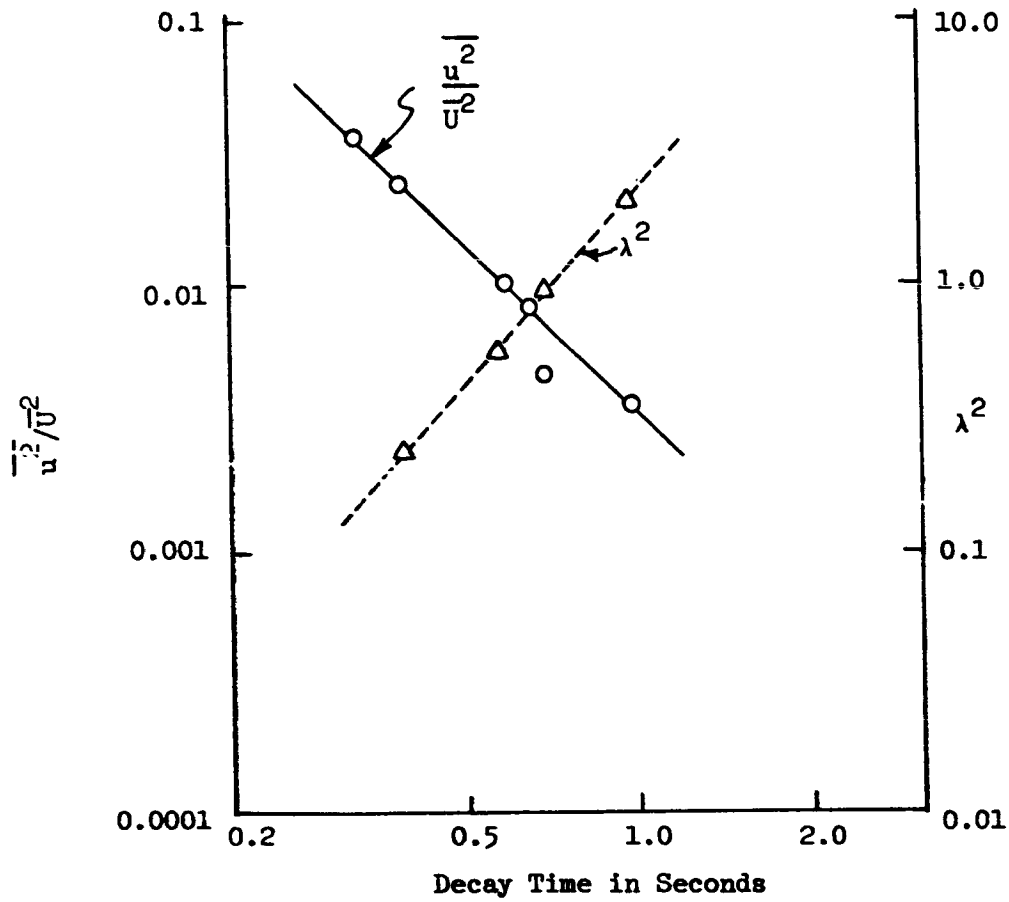

Figure 60

Energy Decay of Turbulence and λ^2 Versus Decay Time

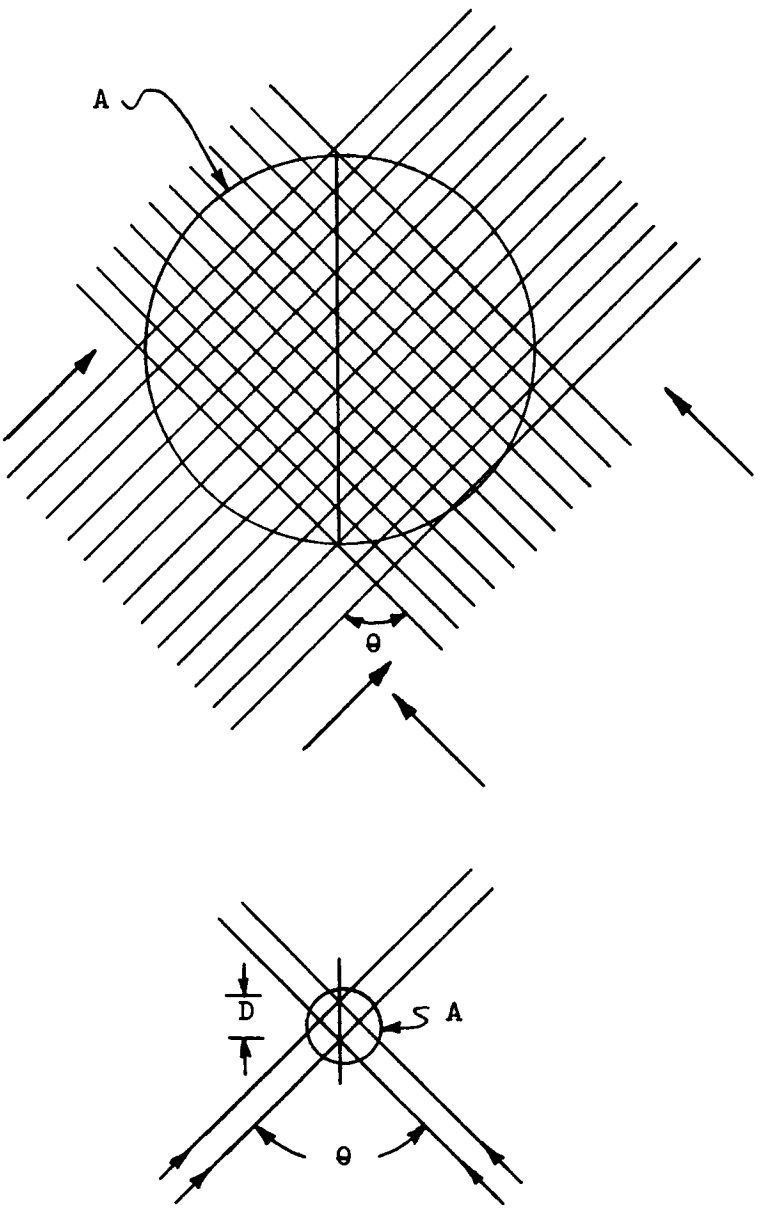

Figure 61

Interference Pattern Produced by Two Plane Parallel Incident Beams

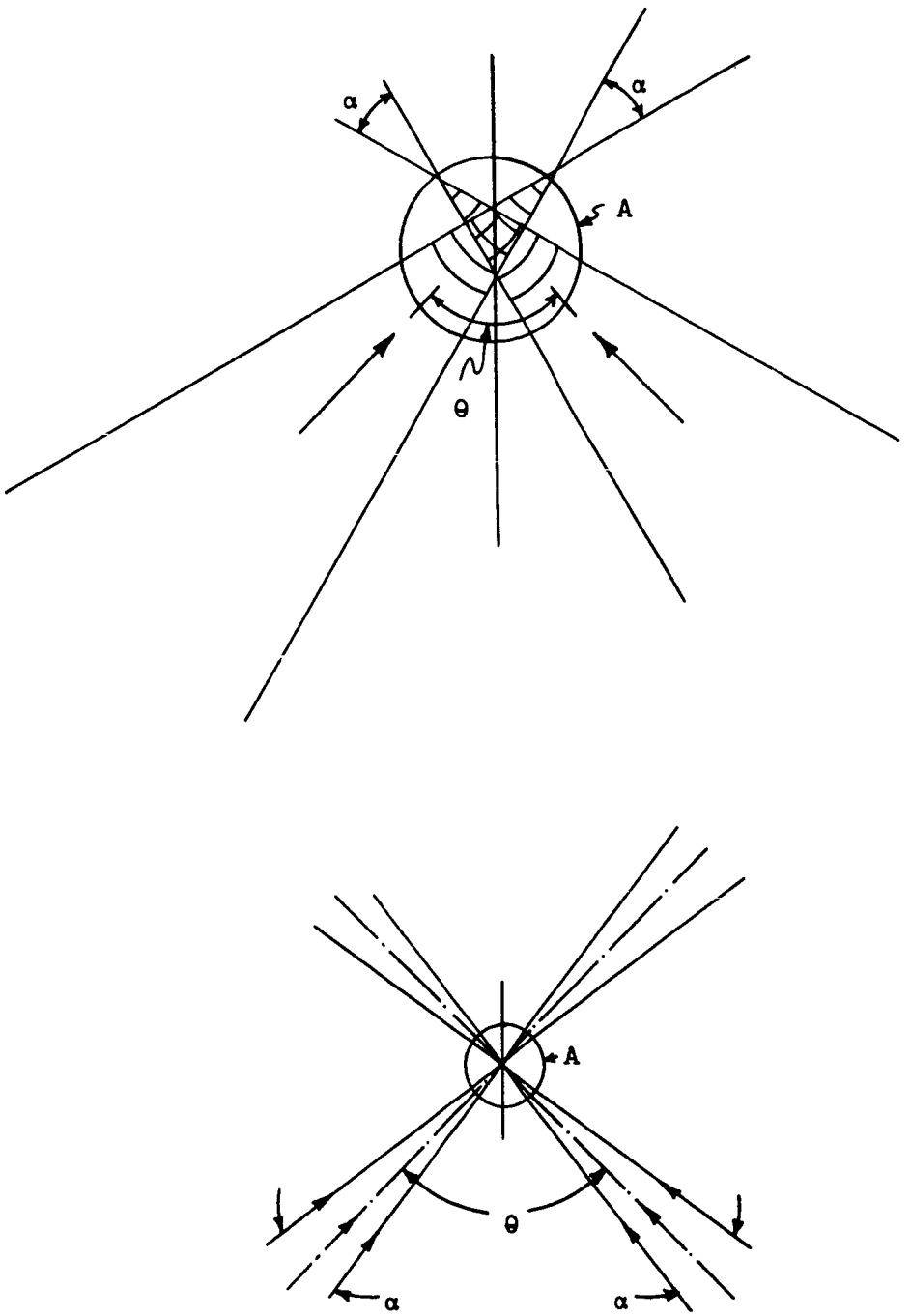

Figure 62

Interference Pattern Produced by Two Converging Incident Beams